Hydrodynamics of crustal detachments and syn-kinematic granites: numerical exploration and implication on uranium mobilities

Khaled Bock[1], Yannick Branquet[1,2], Philippe Boulvais[1], Thibault Duretz[1,3]

[1] *Univ Rennes, CNRS, Géosciences Rennes, UMR 6118, 35000 Rennes, France*
[2] *ISTO, UMR7327, Université d'Orléans, CNRS, BRGM, Orléans F-45071, France*
[3] *Goethe Universität Frankfurt FB 11, Institut für Geowissenschaften Altenhöferallee 1, 60438 Frankfurt*

Abstract. Detachment zones represent a meeting point between surface-derived fluids and rocks, potentially forming mineralized systems (e.g., uranium deposits). However, the hydrodynamics and solute transfer in these zones remain poorly understood, with limited knowledge of the role of plutons associated with detachments. To address these gaps, 2D hydrodynamic numerical models were developed. The study employed a strategy to constrain the numerical modelling set-up by considering the impact of topographical gradient and syntectonic magmatic activity. It also conducted a sensitivity analysis on permeability contrast between the detachment and crust domains and traced meteoric fluids into the detachment, discussing their implications on uranium mobility. The outcomes of the study demonstrate that downward fluid percolation from the surface into detachment zones occurs through two possible mechanisms: (1) an elevated topographic profile (≥ 3000 m) combined with high detachment permeability (i.e., 100 times higher than crust permeability), (2) the presence of a heat source like synkinematic pluton within the detachment. The latter mechanism was found to be more effective in facilitating the downward percolation of meteoric fluids that maintained their liquid state. Additionally, the study found that secondary faults in the hanging wall stabilize hydrodynamics by concentrating solute flows, creating areas favorable for mineralization.

1 Introduction

Detachments, also known as low-angle normal faults (LANF), are faults that occur on a sub-regional to regional scale with an initial shallow dip, likely less than 30 degrees. They are ductile-to-brittle normal faults that can be attributed to the evolution of shallow-dipping shear zones that hosted major crustal extensions, giving rise to metamorphic core complexes.

Detachment zones can host mineralization systems as they provide a pathway for fluids to interact with rocks (Bartley and Glazner 1985). In this regard, some detachments show per-ascensum hot fluid circulations (Famin and Nakashima 2005), and others show per-descenscum meteoric fluid indicators (Morrison and Anderson 1998). Indeed, oxygen and hydrogen isotope signatures indicate that meteoric fluids can attain depths of about 4 to 10 km with a temperature of ca. 350°C (Morrison 1994).

Fluid flow in detachment zones is controlled primarily by buoyancy effects, topography, and permeability contrasts (Figure 1). Although pluton emplacements can enhance buoyancy in the system, their influence on meteoric fluid circulations is yet unknown. It is uncertain whether they play a significant role in mineralized systems or prevent fluids from descending. Moreover, the hydrodynamics and solute transfer in these systems, with or without plutons, are insufficiently known in terms of the driving forces behind fluid flow, particularly topography, and are scarcely explored numerically or constrained by permeability (Person et al. 2007).

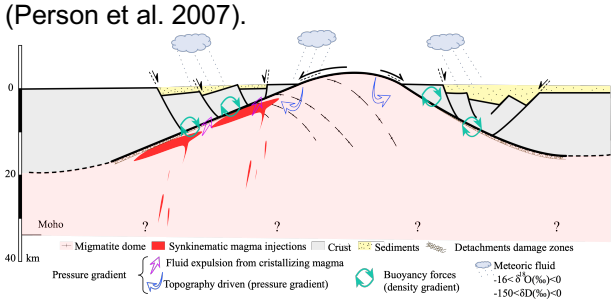

Figure 1. Major fluid driving forces within continental detachments.

Uranium deposits and mobilities in the southern Armorican detachment zones are linked to crustal detachments and syn-kinematic granitic plutons (Figure 2). The magmatic-hydrothermal history is multiphase, with the main mineralization occurring at ca. 300 Ma, soon after leucogranite emplacement.

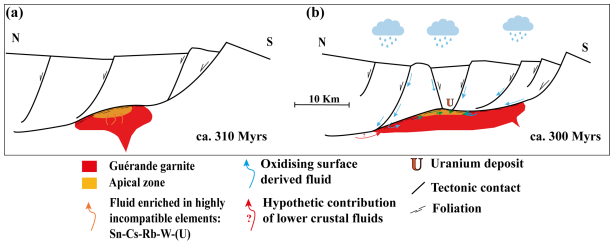

Figure 2. Conceptual model showing the main phases of the evolution of uranium mineralization in the Guérande leucogranite (Localized in the Armorican Massif). (**a**) Emplacement of the granitic pluton at ca. 310 Ma in an extensional deformation regime. (**b**) Brittle deformation at ca. 300 Ma allows the infiltration of meteoric fluids to leach the granite and transport the uraniferous species and precipitate them in the reducing zones. Modified after Ballouard et al. (2017)

The aim of this study is to improve our understanding of the meteoric fluid flow patterns in

detachment zones and their consequences for uranium species transport by building numerical hydrodynamic models based on the Guérande uranium mineralized system.

2 Numerical approach

2.1 Strategy

A series of numerical simulations using Comsol Multiphysics (finite element method) was performed. This numerical investigation has been categorized into three core parts, illustrated in Figure 3. Firstly, a 2D model was constructed to assess buoyancy without topography. Secondly, a model with two topographies (500 m and 3000 m) was tested with an additional driving force of pressure gradient. One topography model was chosen for the injection of a heat source represented by a pluton at two positions - shallow (≈ 4 km) and deep (≈ 10 km) - to understand the limits of the pluton's contribution to the hydrodynamic system. Following the first two steps, a sensitivity study was conducted on the tested permeability models.

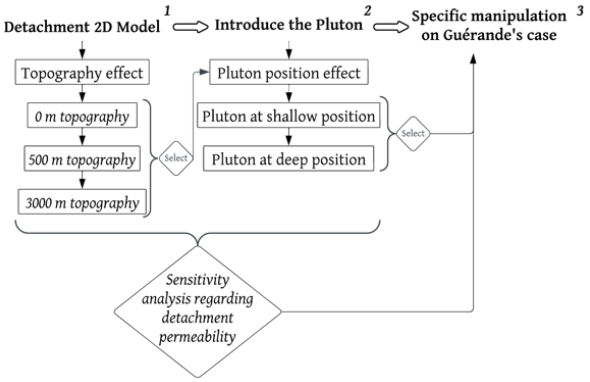

Figure 3. Flow chart of the main steps in the modelling process.

Subsequently, the third stage of the numerical investigation focused on the Guérande case with emphasis on the shallower pluton position. An initial 0-10 Ma calculation was performed without topography to establish a stable fluid flow period, followed by main models covering a time scale of 20 Ma with topographical gradient and pluton models. The detachment was active throughout the 20 Ma periods with the pluton activated between 10 and 11 Ma, using felsic magma temperature below 900 K.

2.2 Initial and boundary conditions

The initial and boundary conditions used for the simulations are shown in Figure 4. To improve accuracy, we increased the mesh resolution in the detachment region by using a maximum mesh size of 50 m and more meshed surfaces, as shown in Figure 4c.

The thickness of the detachment is an important factor since it determines the extent to which the hydrodynamic system may arise. In detachment systems, the diffuse zone of strain can extend up to 1.5 km (Whitney et al. 2013). The damage zone is typically thicker in the hanging wall than in the footwall, and this asymmetry was incorporated into our model (Figure 4) with a detachment thickness ranging from 400 m at the surface to 1 km in depth.

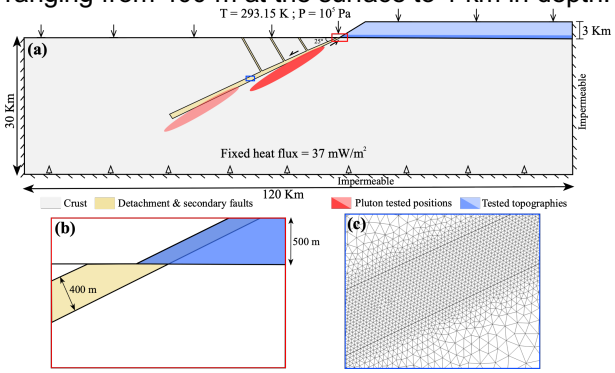

Figure 4. (a) The 2D geometry model displays the defined boundaries and initial conditions, along with the tested positions of the pluton and the topographical gradients. **(b)** A close-up showing the topography and the detachment thickness near the surface. **(c)** A zoomed-in view highlights the mesh resolution in the detachment domain. The model's both sides and bottom indicate no flow with thermal insulation on the left and right edges, at the top, the arrows denote the surface pressure, and surface temperature which varies according to the normal geothermal gradient. The arrows at the bottom indicate the heat flux.

2.3 Governing equations and physical parameters

Heat equations (Equation 1) and Darcy's law (Equation 2) were coupled in our models.

$$\left(\rho C_p\right)_{eff}\frac{\partial T}{\partial t}+\rho_f C_{p,f}u\cdot\nabla T+\nabla\cdot q=Q_t \qquad (1)$$

$$q=-k_e f f\nabla T$$

$$\frac{\partial}{\partial t}\left(\epsilon_p\rho_f\right)+\nabla\cdot\left(\rho_f u\right)=Q_m \qquad (2)$$

$$u=-\frac{k}{\mu}\left(\nabla p+\rho_f g\right)$$

The permeability and the Peclet number (Pe) are both key parameters in our study, the former (described by Equations 3 and 4) guide the hydrodynamic system, whereas the latter (described by Equation 5) enables us to identify areas where thermal advection prevails over thermal conduction.

$$K_c=5\times10^{-16}\times\exp\left(\frac{y}{\delta}\right) \qquad (3)$$

$$K_{d1}=K_c\times10\,;\,K_{d2}=K_c\times30\,;\\ K_{d3}=K_c\times50\,;\,K_{d4}=K_c\times100 \qquad (4)$$

$$Pe=\frac{Lu}{\alpha}\quad \alpha=\frac{K}{\left(\rho C_p\right)} \qquad (5)$$

3 Results and discussion

3.1 Topographic gradient effect

The relationship between topography gradient, detachment permeability (K_{d1} and K_{d4}), and fluid flow into the detachment zone through Peclet numbers (Pe) patterns are shown in Figure 5. The 500 m and 3000 m topography models with low detachment permeabilities exhibit Pe values exceeding 1, for which advection dominates over diffusion, in the superficial area due to gravity-driven downward fluid flow. With high detachment permeability, this flow extends deeper into the detachment, accompanied by a slight deformation of the isotherms in the 500 m model. The 3000 m topography model shows similar tendencies, with more pronounced and distinct isotherm deformation and higher Peclet number values. In contrast, apart from a small increase in the Pe values in the high detachment permeability, the topography-free model shows no significant disturbance to the horizontal isotherms.

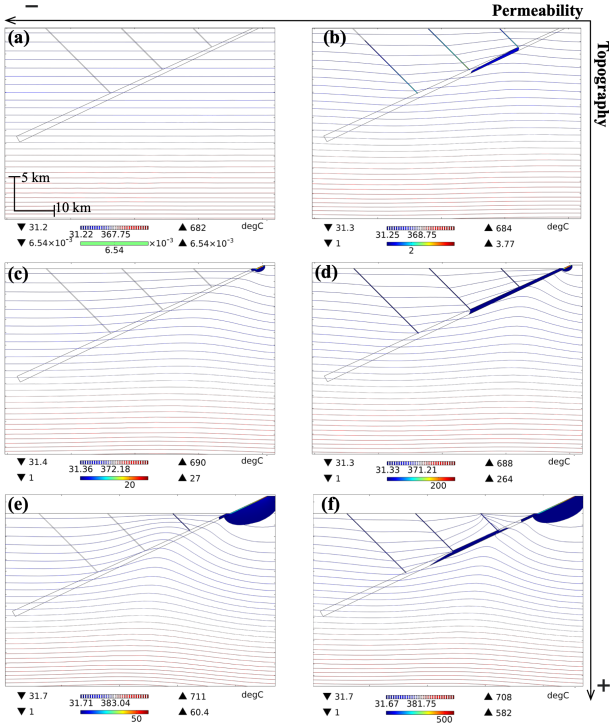

Figure 5. Topography models showing the Peclet number and isotherms within the detachment zone and its secondary faults. The two columns denoted **(a)** and **(b)** represent the permeability models K_{d1} and K_{d4}, respectively. The **(a)**-**(b)** line corresponds to the free topography model, while **(c)**-**(d)** and **(e)**-**(f)** represent the topography models of 500 m and 3000 m, respectively.

3.2 Pluton effect

For the sake of concision, only the nearest pluton position to the surface (Figure 6), which corresponds approximately to the position of the Guérande granite, will be presented. The K_{d3} model (Figure 6a) shows an increasing trend in the Peclet number during the activation of the pluton (10.5 Ma) and the cooling period (11.1 Ma). In both cases, we observe the migration of the Peclet number values greater than 1 from the detachment zone to the hanging wall in the crust ahead of the pluton. Similar patterns are visible in the K_{d4} model (Figure 6b) with even higher Peclet number values, particularly during the pluton's active phase. Panels c and d in Figure 6 illustrate the Peclet number models by showing the direction of fluid flow in conjunction with the deformation of the isotherms. These visualizations demonstrate a downward fluid flow via two of the secondary faults along with the detachment, and an upward circulation towards the surface via the third secondary fault.

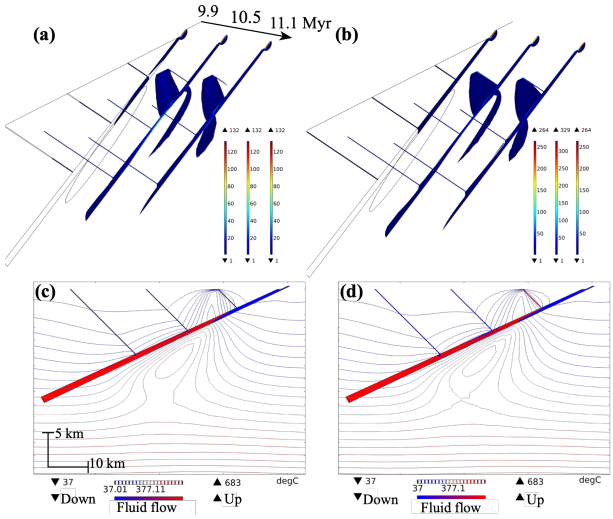

Figure 5. Evolution of the Peclet number in the detachment zone and associated secondary faults before, during, and after the pluton activity using two detachment permeability models K_{d3} and K_{d4}, correspondingly, for **(a)** and **(b)**. In **(c)** and **(d)** Darcy velocities indicate fluid flow direction in detachment zones for both permeabilities K_{d3} and K_{d4} following pluton deactivation.

3.3 Detachment permeability sensitivity analysis

Figure 7 presents two cross-sections of the detachment and one of the three secondary faults, displaying the correlation between the Peclet numbers and the four tested detachment permeability laws (Equation 4). These models are limited to the first pluton position and the three topographic gradient models that were examined.
In the detachment cross-section with no topography, all permeability models exhibit Peclet number values below one, whereas, in the detachment cross-section with a 3000 m topography setup, Peclet number values exceeding the thermal advection threshold are observed in three of the four detachment permeabilities (K_{d2}, K_{d3}, and K_{d4}). The Peclet numbers are relatively evenly distributed across all topography models in the high detachment permeability (K_{d4}) in the secondary fault cross-section, with all models indicating Peclet number values above 1. Hence, an increase in the Peclet number is evident with an increasing topographical gradient. The pluton model

cross-section panels (Figure 7d, e) exhibit a significant increase in Peclet number values during the activity of the pluton and cooling phases, particularly in the secondary fault.

In quantitative terms, the heat source underneath the detachment zone triggers significant surface-derived fluid percolation, even in areas with low topographic gradients or permeability ratios. This is due to the temperature and permeability contrast between the pluton and its surrounding rocks (e.g., Eldursi et al. 2009; Launay et al. 2023). Fluid molecules from various surface locations (i.e., detachment and secondary faults), have been tracked deep into the detachment during the pluton's activation and cooling phases (10-12 Ma). The results of the tracking indicate that these fluids retained their liquid state and penetrated approximately to a depth ranging from 4 to 11 kilometers where they reaches the apex of the pluton.

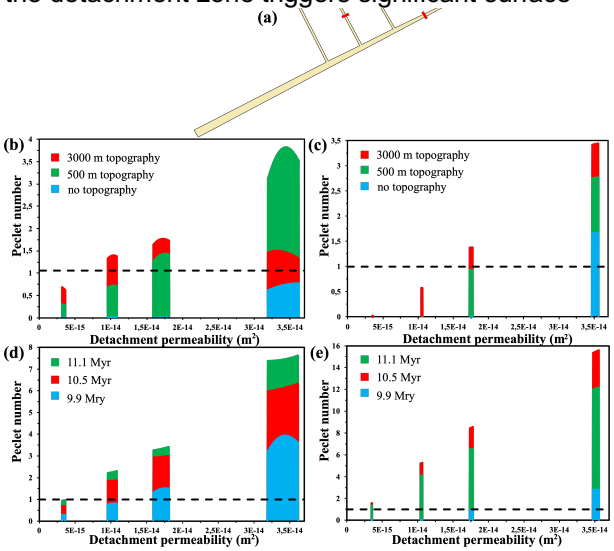

Figure 6. Peclet number as a function of detachment permeability models for two cross-sections from **(a)**. Panels **(b)** and **(c)** respectively depict the detachment cross-section for the three tested topographies and the first pluton position at three different instants (before, during and after its activity). Similarly, panels **(c)** and **(e)** display the fault cut section.

4 Conclusions

The present investigation suggests that a hydrodynamic system featuring downward fluid flow patterns can arise through two models, knowing that forced convection and free convection play simultaneously in each. The first model involves a high topography gradient coupled with a high permeability ratio between the crust and the detachment zone, with the crust's permeability being at least $5 \times 10^{-16}\,\mathrm{m}^2$. The second model is associated with a magmatic activity represented by a syntectonic pluton emplacement that triggers advection and allows for rapid percolation ($\approx 2 \times 10^{-8}\,\mathrm{m \cdot s}^{-1}$) of surface-derived fluids into the detachment. The latter is deemed to be more effective and more reliable of the two mechanisms. Leaching of the apical zones of the plutons, leading for instance to the leaching of uranium, as documented in the case of the Guérande granite (Ballouard et al. 2017).

The secondary faults in the hanging wall play a crucial role in stabilizing the hydrodynamics by concentrating solute flows and transporting meteoric fluids from the surface into the detachment zone. These findings shed light on the mechanisms of fluid migration in detachment zone systems, particularly in hydrothermal systems and uranium mineralization processes. Further research is needed, specifically through the integration of chemical components and the transport equation of uranium species, to investigate the influence of the outlined hydrodynamic mechanism on the precipitation and transport of uranium.

Acknowledgements

This study is granted by the NEEDS consortium through the URAMOD project.

References

Ballouard, C., Poujol, M., Boulvais, P., Mercadier, J., Tartèse, R., Venneman, T., Deloule, E., Jolivet, M., Kéré, I., Cathelineau, M., & Cuney, M. (2017). Magmatic and hydrothermal behavior of uranium in syntectonic leucogranites: The uranium mineralization associated with the Hercynian Guérande granite (Armorican Massif, France). *Ore Geology Reviews*, *80*, 309–331. https://doi.org/10.1016/j.oregeorev.2016.06.034

Bartley, J. M., and Glazner, A. F. (1985): Hydrothermal systems and Tertiary low-angle normal faulting in the southwestern United States. *Geology*, *13*(8), 562. https://doi.org/10.1130/0091-7613(1985)13<562:HSATLN>2.0.CO;2

Bons PD, Gomez-Rivas E. Origin of Meteoric Fluids in Extensional Detachments. Geofluids. 2020; 2020:1-8. doi:10.1155/2020/7201545

Eldursi K. Minéralisations et Circulations péri-granitiques: Modélisation numérique couplée 2D/3D, Applications au District minier de Tighza (Maroc-Central). Published online 2009:220.

Famin, V., and Nakashima, S. (2005): Hydrothermal fluid venting along a seismogenic detachment fault in the Moresby rift (Woodlark basin, Papua New Guinea): HYDROTHERMAL FLUID VENTING. Geochemistry, Geophysics, Geosystems, 6(12), n/a-n/a. https://doi.org/10.1029/2005GC001112

Launay G, Branquet Y, Sizaret S, Guillou-Frottier L, Gloaguen E. How greisenization could trigger the formation of large vein-and-greisen Sn-W deposits: A numerical investigation applied to the Panasqueira deposit. Ore Geology Reviews. 2023;153:105299. doi:10.1016/j.oregeorev.2023.105299

Morrison, J., and Anderson, J. L. (1998). Footwall Refrigeration Along a Detachment Fault: Implications for the Thermal Evolution of Core Complexes. Science, 279(5347),63–66. https://doi.org/10.1126/science.279.5347.63

Morrison J. Meteoric water-rock interaction in the lower plate of the Whipple Mountain metamorphic core complex, California. Journal of Metamorphic Geology. 1994;12(6):827-840.doi:10.1111/j.1525-1314.1994.tb00062.x

Person M, Mulch A, Teyssier C, Gao Y. Isotope transport and exchange within metamorphic core complexes. American Journal of Science. 2007;307(3):555-589. doi:10.2475/03.2007.01

Whitney DL, Teyssier C, Rey P, Buck WR. Continental and oceanic core complexes. Geological Society of America Bulletin. 2013;125(3-4):273-298. doi:10.1130/B30754.1

Las Minas newly recognized epithermal deposit and its relationship with Tatatila-Las Minas Skarn, Veracruz, Mexico.

Pablo E. Carbajal[1], Jesús Castro Mora[2], Julie Roberge[1], Gerardo Arrieta[3], Godwyn Paulson Pitchaimani[1], Celestine N. Mercer[4].
[1]Posgrado ESIA Ticomán, Instituto Politécnico Nacional, CDMX, Mexico
[2]Universidad Autónoma del Estado de Hidalgo, Mexico.
[3]Laboratorio Universitario de Geoquímica Isotópica (LUGIS), Instituto de Geofísica, Universidad Nacional Autónoma de México (UNAM), CDMX, Mexico
[4]U.S. Geological Survey, Geology, Geophysics and Geochemistry Science Center, Denver, CO.

Abstract. The Las Minas district, Veracruz, hosts the well-known Tatatila–Las Minas IOCG skarn deposits. Until now, the possibilities of other types of deposits in the area have been ignored because of the presence of this skarn, which has reported reserves of 719,000 oz Au eq. This work aims to show the existence of another type of mineral deposit overprinting the mineralized zone of the Tatatila–Las Minas skarn deposit. Regional geology shows a vast extension of dolomites and limestones of the Tamaulipas inferior formation which were intruded during the Miocene by three thermal events of granitic to granodioritic composition. As a result of the intrusions, a contact metamorphism zone was developed and led to the precipitation of skarn minerals rich in Cu-Fe-Au-Ag.
Based on petrographic and mineralogical studies of skarn samples, evidence for hydrothermal fluid circulation and epithermal veins has been observed, suggesting the presence of an epithermal deposit overprinting large exposures of the skarn.
Linking the geological history of both deposits will help to understand if both mineralization events were cogenetic or originated from different geological events.

1 Introduction

The mining district of Las Minas (LM), Veracruz is within the youngest portion of the Trans Mexican Volcanic Belt (TMVB), in the east-central part of the state of Veracruz (Figure 1).

Figure 1: Location map of the studied area.

Attention in the mineralized zone of Las Minas is focused on the Tatatila–Las Minas IOCG skarn deposit that hosts Au, Ag and Cu that are currently being exploited. However, we have discovered petrologic and mineralogic evidence indicating epithermal mineralisation overprinting the skarn. The aim of this study is to further characterize this newly identified mineralization.

The known mineralized zones in Las Minas consist of a Au-Cu-Ag-magnetite skarn and a Zn-Pb-Ag skarn (Fuentes-Guzmán et al. 2020). Metal values of the skarn deposit reported by the Mexican Gold Mining Corp (2023) show that concentrations vary from: Au 1 to 39.3 g/t, Ag 4.11 to 127 g/t and Cu 0.64% to 11.7%, with principal inferred reserves of 719,000 oz Au eq.

Exploration of the mineralized zones is challenging due to the topographic changes of mountains that are full of vegetation. But up to 1000 m of the stratigraphy of Las Minas is intermittently exposed in deep valleys cutting the high volcanic plains.

The skarn is largely exposed in the mining district (Figure 2) where large outcrops of carbonate rocks from the Tamaulipas Inferior formation outcrop. This is where the economic values of minerals of the skarn were found.

After a successful exploration, Mexican Gold Corporation has targeted exploitation of the skarn with open-pit methods.

The geologic and metallogenic framework of both the skarn and the possible epithermal deposit can help understand if the Tatatila–Las Minas IOCG skarn deposit is a part of a larger mineralized system that merits further exploration.

This study presents a digital elevation model with newly integrated observations of alteration zones, mineralogical, and petrographical information that we have collected. The map will also show previously published geologic and structural characteristics that will provide context to interpret our new observations. The map will help elucidate the paragenetic sequence of the skarn and the newly discovered epithermal deposit as well as the petrogenesis of the larger hydrothermal system.

Mining in Mexico is one of the main sources of employment (Azamar 2022). Therefore, the discovery of new mineralized zones in the municipality of Las Minas can help the state's economic growth and social welfare. It can be an important source of employment for both men and

women, promoting inclusion in mining and research.

2 Regional geologic context

The regional geology is summarized by the *Perote* E14-B26 geological map (Fig. 2; Mexican Geological Service, 2007).

The north central part of the E14-B26 map is where the mining district of Las Minas is located (Figure 2). Early Cretaceous limestones and dolomites are intruded by three Miocene granite to granodiorite intrusive events. These middle Miocene (U-Pb 15.05 ± 0.94 Ma) and middle to late Miocene (U-Pb 15.27 ± 0.36 Ma and 14.33 ± 0.38 Ma) granitic and granodioritic rocks that are thought to be related to skarn genesis. These rocks were dated by $^{40}Ar/^{39}Ar$ methods using rare fuchsite, hornblende, K-feldspar and biotite (Fuentes-Guzman et al., 2020). They yielded two groups of ages: (A) late Oligocene to early Miocene (22.12 ± 0.74 Ma) and 19.04 ±0.69 Ma and (B) middle to late Miocene with ages from 16.34 ± 0.20 Ma and 13.92 ± 0.22 Ma (Fuentes-Guzman et al., 2020). Thick sequences of rhyolite and andesite tuffs have been observed and are thought to be cogenetic with mineralizing granites, but they remain to be dated.

The Cretaceous and Miocene rocks have been covered by up to 200 m of pyroclastic flows which according to Olvera et al. (2020) came from the *Los Humeros* volcanic center, 20 km west and host to one of the biggest producing geothermal systems in Mexico.

There are two principal dextral faults that correspond with the alignment of two principal rivers: *Las Minas* and *La Trinidad.* The faults are oriented from NNE to SSW. Also, NNW to SSE faults are observed following some other rivers too.

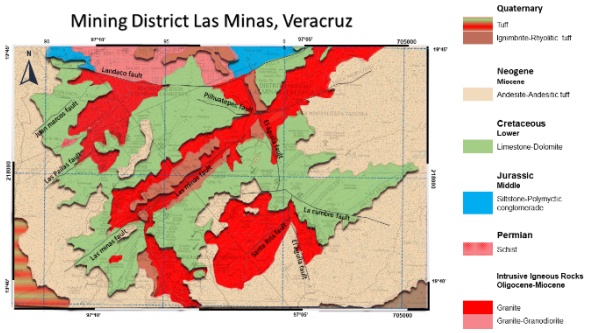

Figure 2: Geologic map of Las Minas mining district, Veracruz, Mexico.

3 Field observations

The proximal zone of the skarn is characterized by rocks with granoblastic texture and metallic IOCG mineralization with native copper, wollastonite, clinopyroxenes and garnet that vary from green to brown colors. Distal zone of the skarn is characterized by coarse to fine grain marble. There are calcite veins and coarse bladed calcite in outcrops indicating high temperature hydrothermal fluids, but their paragenesis is as yet unknown.

The skarn is cut by meter-wide granitic dykes that are mineralized, which in turn are cut by mafic dykes that are not mineralized or enriched in any precious metals. Although mineralization is not observed in mafic dykes, they help us to understand how the mining district was affected by regional thermal events that could affect future thermochronometry studies.

The zone that we hypothesize to be epithermal includes pervasive argillic alteration with coarse (3-4 cm) to fine (<1 cm) euhedral pyrite (Fig. 3).

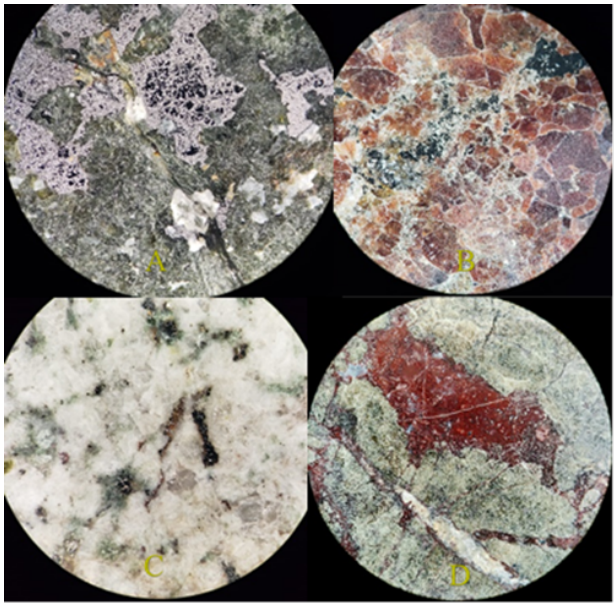

Figure 3: Microphotos of samples from the Tatatila-La Minas Skarn and epithermal (?) deposit.

4 Conclusions and future work

We propose the existence of an epithermal mineral deposit related to the Tatatila–Las Minas IOCG skarn deposit. We are currently synthesizing the digital elevation map with new geologic, alteration, and mineralogic observations in order to understand the temporal relationships and whether the epithermal deposit was formed contemporaneously with the skarn or if formed afterwards during another mineralising event. Future work will include Ar/Ar isotopic studies in order to constrain the paragenetic sequences of the proposed epithermal deposit relative to the skarn deposit.

Acknowledgements

We thank Diego Ibarra Garcia, Lizbeth Carillo Marrodan, Maria Fernanda Reyes Gonzalez and Regina Cuervo Morales for assistance in different parts of the project.

References

Castro-Mora, J. C., Ortíz-Hernández, L. E., Escamilla-Casas, J. C., Cruz-Chávez, E., & Dorantes-Castro, C. G. (2016). Metalogénesis de la mineralización tipo IOCG relacionada al skarn del Distrito Minero Las Minas, Estado de Veracruz. Tópicos de Investigación en

Ciencias de la Tierra y Materiales, 3, 128-143. https://doi.org/10.29057/aactm.v3i3.9617

Fuentes-Guzmán, E., Gonzales, E., Camprubí, A., Hernandez, G., Gabites, J., Iriondo, A., Ruggieri, G. and López, M. (2020): The Miocene Tatatila.Las Minas IOCG skarn deposits (Veracruz) as a result of adakitic magmatism in the Trans.Mexican Volcanic Belt; Boletín de la Sociedad Geológica Mexicana, v.72 (3), p 1-50.

Olvera, E., Blanco, C., Monroy, V., Brogi, A., Liotta, D., Wheeler, W., Gómez, F., Najera, S., Jímenez, A., Guevara, J., Bastesen, E., Lepillier, B., Zucchi, M., Caggianelli, A. and Ruggieri Giovanni. (2020): Geology of Las Minas: an example of an exhumed geothermal system (Eastern Trans-Mexican Volcanic Belt); Journal of maps, v, 16:2, p. 918-926. https://doi.org/10.1080/17445647.2020.1842815

Melt inclusions types within related processes in the Dăneşti - Piatra Roşie realm (Maramureş County, Romania)

Ioan Pintea[1], George Dincă[1], Sorin S. Udubaşa[2], Marian Munteanu[1]
[1] Geological Institute of Romania, Caransebes str., no 1, Bucharest, Romania
[2]Bucharest University, Nicolae Balcescu Blv., no1, Bucharest, Romania

Abstract. Globular sulfide/oxide, silicate melts, and hydrosaline melt inclusion are the main topic of this paper based upon petrograpy, microthermometry, Raman, and SEM/EDS analyses. Dăneşti-Piatra Roşie dacite complex is situated in the Gutâi volcanic zone between Baia Sprie and Cavnic epithermal Au-Ag-Pb-Zn-Cu-W-Sb-Te-As ore deposits. Volcanic lava domes are predominant and melt inclusions were studied in pyroxene, amphibole, plagioclase, quartz, and zircon, mainly as phenoclasts, collected from volcanic debris around Dăneşti village. Microtextural features and postentrapment modifications of the melt inclusions are suggestive for the magma mixing/mingling process in the shallow magma reservoirs. Homogenization temperature in selected silicate melt inclusions ranged between 715º and 1150ºC of more than 200 measurements. The unique presence of hydrosaline melt inclusion trapped in mushy quartz as secondary (pseudosecondary) trails around 3.5 km depth suggesting brine lens formation around the volcanic conduit(s) and upper magma reservoir as in the active volcanism today worldwide, emphasized that this could be the main metal source for the epithermal ore deposits in the area. We noted the Cu- enrichment of the immiscible globular sulfide/oxide globules trapped in minerals and glass matrix as the main result of mafic mineral destruction during magma mixing and degassing.

1 Introduction

Immiscible (Fe-S-O), silicate-, and hydrosaline melt inclusions from pyroxene, amphibole, plagioclase, zircon, and quartz from Dăneşti-Piatra Roşie dacite complex (Figure 1) are representative for intrusive-extrusive volcanic products generated and accumulated in shallow magma reservoir(s) in a complex plumbing system as it was emphasized from thermobaric geochemistry data (Kovacs 2002; Grancea et al. 2003; Kovacs et al. 2021). Petrogenetic minerals were crystallized at various depth batches and suggest specific genetic processes such as magmatic immiscibility, magma mixing/mingling, decompression, and degassing, fluid phase separation, etc. Globular sulphide/oxide inclusions were found variously distributed in minerals as primary inclusions along the growth zones or randomly distributed in the groundmass, generally with a characteristic frothy microtexture (e.g. Laroque et al. 2000; Figure 4). Separate globular sulphide/oxide were also collected freely from volcanic debris and are the most complex ones composed of magnetite dendrites, globular pyrrhotite, Cu-rich sulphide globulae, monosulphide solid solution (mss), and intermediate solid solution (iss) within black silicate glass matrix (Pintea 2008, 2015 - Figures 11 and 12). Silicate melt inclusion is monophasic, biphasic, and multiphasic with opaque and transparent daughter minerals. Their dimension is variable between less than (1-10) to (80-100) micrometres. Generally, they are primarily distributed along the primary growth zones, glassy and/or recrystallized in the internal sieve microtexture, frequently post-entrapment modified by partial remelting, cumulative aggregation, decrepitation, and stretching, because of the hot mafic magma input (e.g. Pintea 2015 - Figure 9). Former yellow-greenish transparent glassy solid inclusions (up to 150-200 micrometers) of silicate perlite-like globule could also be picked up under the binocular microscope (Pintea 2016 unpubl.). Hydrosaline melt inclusions containing halite, anhydrite(?), other salts, opaques, and other transparent daughter phases were described yet, only in one single quartz phenoclast from the outcrop of volcanic rocks around Dăneşti village.

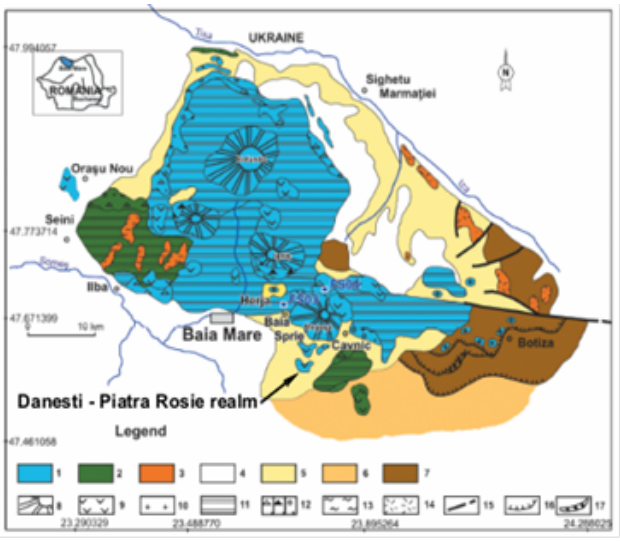

Figure 1. Dăneşti - Piatra Roşie realm on the simplified vulcanological map of the Gutâi Mts. (modified after Iancu and Kovacs eds. 2010). 1. Pannonian volcanics; 2. Sarmatian volcanics; 3. Badenian volcanics; 4. Quaternary; 5. Neogene sedimentary deposits; 6. Oligocene-Miocene sedimentary deposits; 7. Paleogene sedimentary deposits; 8. Effusive cones; 9. Extrusive domes; 10. Intrusives; 11. Volcano-tectonic depression filling; 12. Pyroclastic and epiclastic deposits; 13. Ignimbrites and associated volcanoclastics; 14. Primary and reworked tuffs; 15. Faults; 16. Overthrusts; 17. Pieniny Klippen Zone.

These are secondary or pseudosecondary in origin and the microthermometry results suggested

trapping at depths around 3.5 km. This is suggestive for brine lens formation in the upper part of the present-day volcanoes (Blundy et al. 2021) and is emphasized in this study that, together with the globular sulphide/oxide, these were the primary source of the epithermal mineralizations in the area (e.g. Baia Sprie, Cavnic, Dealul Crucii etc).

2 Methodology

Standard microthermometric measurements (e.g. Pintea 2014) were done in Linkam TS 1500 stage and a "self-built" microthermometric device, starting first at IMP-ETH Zurich (1994) and continued in 2005 and 2015 (Pintea 2006, 2015 – Figs. 78, 123, and Table 4; Pintea et al. 2016; Pintea et al. 2018 unpubl.), especially in unprepared washed grains picked up under a binocular microscope. SEM/EDS and Raman measurements were conducted at the Geological Institute of Romania. A Hitachi TM3030 SEM was used with acceleration voltage of 15 kV. Elemental analysis was done through Bruker's QUANTAX 70 EDS system. Micro-Raman spectra were obtained on polished samples using Renishaw InVia spectrometer with a Peltier cooled CCD detector, equipped with a Leica DM 2700M microscope and 20x, 50x objective lenses. Excitation was provided by a 532 nm laser (RL532C50, Renishaw) with 50 mW power, 10s exposure time, 1-5 accumulations and 1.5 cm^{-1} spectral resolution.

3 Results

3.1 Microthermometry of the silicate melt inclusion

Generally, biphasic inclusions containing glass and vapour bubble(s) were used for microthermometry (Table 1). Frequently, the glass inclusions, mainly in quartz and plagioclase foaming during heating around Tg (glass melting temperature) suggested they were formed in a silicate magma layer saturated in vapour bubbles and the main cause of crystal fragmentation was the explosion of melt inclusions because of the hot magma injection in the magma reservoir (Pintea 2013). Reproducible final homogenization temperature of the trapped silicate foam was slightly variable because of specific foam rheology (Figure 2a).

3.2. Hydrosaline melt inclusion

This was found and described yet in one single quartz grain phenoclast, and consists of an assemblage of multiphasic brine inclusions (Pintea 2016) together with vapour rich ones, in refilled microfissures. Two deformed (remelted) silicate glass inclusions were found very close to each other in this grain (e.g. Figure 2b) and they have been homogenized around 837°-856°C. Brine inclusion contains halite, other salts, silicate, and anhydrite(?) as transparent phases, and sulphide/oxide as opaque phases (Figure 2c). Microthermometric values of one replicated run calculated with *Sowat* (Driesner and Heinrich 2007) are written in Table 1. Despite the fact that there is just one measured assemblage in the mushy rhyolite quartz from Dăneşti-Piatra Roşie dacite complex, their significance is crucial because it is the first time that this kind of inclusions was found in magmatic quartz from the Gutâi Mountains, and their occurrence inside the lava dome at 3.5 km depth suggested the presence of a brine lens formed during volcanic activity comparable with

Table 1. Microthermometric data from biphasic glass inclusions in petrogenetic minerals from Dăneşti-Piatra Roşie dacite complex (modified from Pintea 2006, 2015, and 2016; Pintea et al. 2018 unpubl.), n= number of measurements.

Host mineral	Melt inclusion type	Homo-genization temperature (Th) °C	Observations
Horn-blende	Biphasic (glass + vapor bubble) (n=1)	977	Host opacified at high temperature
Plagio-clase	Biphasic (glass + vapor bubble(s)) (n=23)	811- 1150	Frequently foaming above 530°C
Quartz	Biphasic (glass + vapor bubble(s)) (n=176)	715-986	Almost all inclusions foaming around 530°C; Microsolid melted at 808°C and 844°C (n=2)
	Hydro-saline melt inclusion (n=1)	≥ 916-922	Tm halite= 555°C; Salinity= 67.7405wt% NaCl eq.; x_{NaCl}=0.40; P= 1332.55 bar, d= 1.0455 g/ccm; Single phase state. Replicated data Tmhalite= 571°C; Salinity= 69.9075 wt% NaCl eq., x_{NaCl}= 0.41; P= 1265.04 bar; d= 1.06665 g/ccm; V+L phase state.

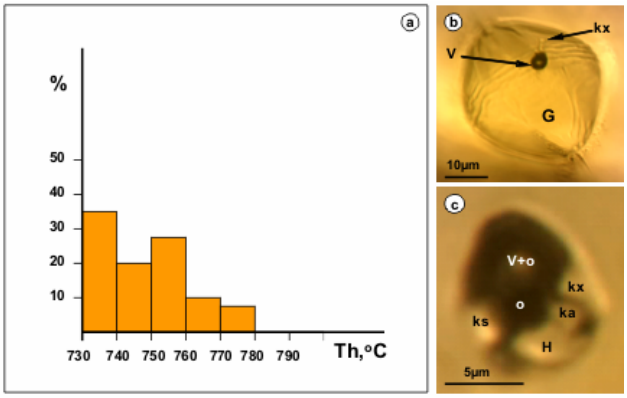

Figure 2. a. Reliability test in one single silicate foam glass inclusion showing variable homogenization temperature, in mushy quartz phenoclast from Dăneşti-Piatra Roşie dacite (data from Pintea 2006; n=15, median= 755ºC); **b**. primary silicate foam glass inclusion; **c.** secondary (pseudosecondary) hydrosaline melt inclusion. Notations: Th- homogenization temperature, G- glass, V- vapor, kx- silicate solid, H- halite, Ks- other salt, ka- anhydrite(?), o- opaque.

present-day findings around the world (Blundy et al. 2021). Moreover, together with the globular sulphide/oxide immiscible melt (see below) were the main source of gold/base metal epithermal ore deposits from the area.

3.3 Raman and SEM/ EDS analyses of globular sulfide/oxide immiscible melt

They are comparable with common Fe-S-O immiscible melt described worldwide (e.g. Larocque et al. 2000; Georgatou et al. 2022; Heinrich and Connolly, 2022). There are two groups of inclusions studied in this paper: one is formed by separated black globules (Pintea 2008, 2015 - Figure 11) up to 1 mm diameter, composed of silicate glass, segregated sulphide, and oxide phases, mainly as pyrrhotite, monosulphide solid solution (mss), intermediate solid solution (iss), chalcopyrite, dendritic magnetite, and possible pentlandite (Figure 3) the other one being represented by the frothy globular sulphide/oxide included in minerals and glass matrix. The Raman spectra suggested the presence (based on RRUFF database; e.g. Figure 4) of neighborite ($NaMgF_3$), yugawaralite ($CaAl_2Si_6O_{16.4}H_2O$), cotunnite ($PbCl_2$), and salammoniac (NH_4Cl) in the black matrix and digenite ($Cu_{1.8}S$), tenorite (CuO), bismuth (Bi), jamesonite ($Pb_4FeSb_6S_4$) in the white and yellow zones inside the sulphide globules.

4 Conclusions

Fe-S-O sulfide/oxide globule, silicate-, and hydrosaline melt inclusions from Dăneşti-Piatra Roşie rhyolite/dacite dome complex are representative for specific magmatic-hydrothermal processes evolved in a shallow magma chamber, around 3.5 km depth, before and during the eruption, including immiscibility, magma mixing, crystallization, decompression, and degassing.

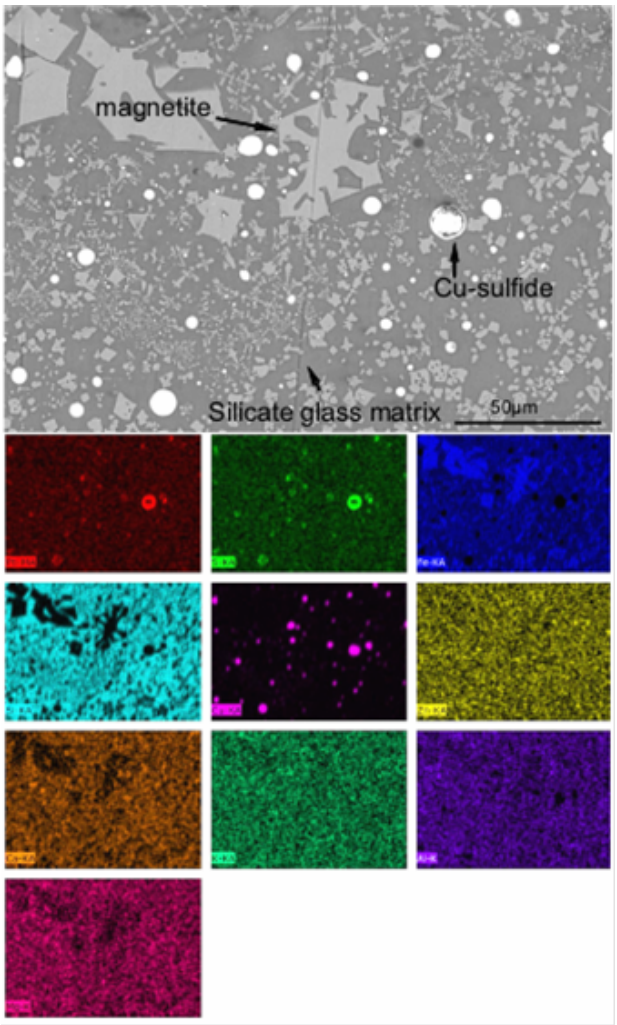

Figure 3. SEM/EDS mapped image within a separate Fe-S-O globule from Dăneşti-Piatra Roşie dacite debris near Dăneşti village (Maramures county) indicating composition of Pb, S, Fe, Si, Cu, Zn, Ca, K, Al, Mg.

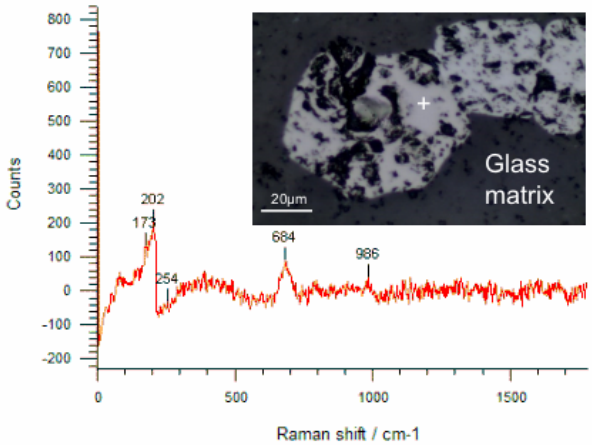

Figure 4. Raman spectra of a frothy Fe-S-O globule in silicate glass matrix from Dăneşti-Piatra Roşie dacite. RRUFF data base suggested the presence of Ca, Si, Al, Mg, Cu, Au, Pb, W, Sb, F^-, Cl^-, NH_4^+, SO_4^{2-}, PO_4^{3-} in various mineral species.

Silicate melt inclusions in quartz, plagioclase, and amphibole indicated low temperature for the mushy rhyolite quartz at 715°C and up to 1150°C for the mafic magma input. During mixing/mingling processes, the mafic minerals were partially dissolved, releasing the Fe-S-O globular melts which concentrated Cu and other metallic elements in sulphide globule segregated from the basic silicate melt together with dendritic magnetite, and possible pentlandite exsolved during decompression and degassing. These were reworked by ultimate hydrosaline fluid and deposited in the upper part of the shallow magma reservoir and around the volcanic conduit(s) Raman and SEM/EDS preliminary analyses of the Fe-S-O globule indicate the presence of silicate, sulphides, oxide, fluoride, ammonium (NH_4^+), sulphate (SO_4^{2-}), phosphate (PO_4^{3-}), fluoride (F^-), and chloride (Cl^-) in mineral species containing Ca, Mg, K, Al, Si, Fe, Au, Cu, Pb, Zn, W, Bi, Sb, Ni, and probably more, representing the primary source of the ore elements in the convective hydrothermal systems from Baia Sprie, Cavnic, Dealul Crucii etc.

Acknowledgements

The authors acknowledge the financial support and access to SEM-EDS and Raman analysis, provided by the GeoEcoLab Laboratory (Geological Institute of Romania). The authors acknowledge the financial support by the national research project PN23-39-02-03.

References

Blundy, J., Afanasyev, A., Tattich, B., Sparks, S., Melnik, O., Utkin, I., Rust, A. (2021): The economic potential of metalliferous sub-volcanic brines. R. Soc. Open Sci. 8 202192.

Driesner, T. and Heinrich, C. (2007): The system H_2O-NaCl. Part I: Correlation formulae for phase relations in temperature pressure-composition space from 0 to 1000°C, 0 to 5000 bar, and 0 to 1 X_{NaCl}. Geochimica et Cosmochimica Acta, v. 71, p. 4880-4901.

Georgatou, A., Chiaradia, M., Klaver, M. (2022): Deep to shallow sulfide saturation at Nisyros active volcano. Geochemistry, Geophysics, Geosystems, v. 23, issue 2, p. 1-21.

Grancea, L., Fulop, A., Cuney, M., Leroy, J., Pironon, J. (2003): Magmatic evolution and ore-forming fluids in the origin of gold/base metals mineralization in the Baia Mare province, Romania. Journal of Geochemical Exploration, v.78 -79, p. 627-630.

Heinrich C.A. and Connolly J.A.D. (2022): Physical transport of magmatic sulfides promotes copper enrichment in hydrothermal ore fluids. Geology, 50, p. 1101-1105.

Iancu, O.G. and Kovacs, M., eds. (2010): Ore deposits and other classic localities in the Eastern Carpathians: From metamorphic to volcanics. Acta Mineralogica - Petrogrographica, Field guide series, Szeged, Hungary. V. 19, p.1-55.

Kovacs, M., (2002): Petrogenesis of Subduction-Related Igneous Rocks from the Central Southeastern Area of the Gutâi Mts. Editura Dacia Cluj-Napoca. (in Romanian). 201 p.

Kovacs, M., Fülöp, A., Seghedi, I., Pecskay, Z. (2021): Architecture of volcanic plumbing systems inferred from thermobarometry: A case study from the Miocene Gutai volcanic zone in the Eastern Carpathians, Romania. Lithos, v. 396-397, 106191.

Larocque, A.C.L., Stimac, J.A., Keith, J.D., Huminicki, M.A.E. (2000): Evidence for open-system behavior in immiscible Fe-S-O liquids in silicate magmas; implications for contributions of metals and sulfur to ore-forming fields. Canadian Mineralogist, v. 38, p. 1233-1250.

Pintea, I., (2006): Melt inclusion texture and microthermometry in volcanic phenoclasts from the central neogene segment, East Carpathians, Romania. An. Inst. Geol. of Romania, Bucharest, v. 74, spec. issue, p.171-172.

Pintea, I., (2008): Fluid and melt inclusion evidence for succession of magmatic and hydrothermal events from Neogene/Quaternary subduction zone in Carpathians. In Pan-American Conference on research on Fluid Inclusions (PACROFI IX) - In memory of Edwin Roedder (ed. H.E. Belkin), Program and Abstracts Reston, V.A, USA, p. 47.

Pintea, I., (2013): Melt inclusions texture and thermal history in minerals from the Dej Tuff, Transylvania basin, Romania. Romanian Jour. of Earth Sciences, Bucharest, V. 87, issue 1-2, p.29-47.

Pintea, I., (2014): The magmatic immiscibility between silicate-, brine-, and Fe-S-O melts from the porphyry (Cu-Au-Mo) deposits in the Carpathians (Romania): a review. Romanian Jour. of Earth Sciences, 87, issue 1-2, p. 1-33 (published 2023 at igr.ro).

Pintea, I., (2015): Fluid in the earth crust and upper mantle: an atlas of the fluid and melt inclusions from Romania. Romanian Jour. of Earth Sciences, v. 87, issue 1-2, p. 35-250 (published 2023 at igr.ro).

Pintea, I., (2016): A self-perspective research topic revealed during the elaboration of the Atlas “Fluid and Melt Inclusions from Romania”. Rom. J. Mineral Deposits, v. 89, issue 1-2, p. 1-6.

Thermodynamic modeling of hydrothermal equilibria: a critical assessment using mineral solubility and aqueous speciation

David Dolejš[1], Federica Salomone[1]
[1]Institute of Earth and Environmental Sciences, University of Freiburg, Germany (david.dolejs@minpet.uni-freiburg.de)

Abstract. Ore formation in hydrothermal systems is commonly coupled to fluid-rock interaction and associated changes in acidity, redox and other system variables. These mechanisms are addressed by thermodynamic chemical equilibrium modelling, but the conventional electrostatic (Helgeson-Kirkham-Flowers, HKF) approach is inappropriate under high-temperature and low-pressure conditions relevant to shallow magmatic and epithermal systems. We explore available, alternative physico-chemical approaches to mineral solubility and aqueous speciation. Ten models for water dissociation accurately converge below 400 °C and increasingly diverge below 1.0 kbar at 600 °C. The ionization in low-density fluids is best captured by semicontinuum hydration or density models. Sixteen models for quartz solubility in water provide comparable and accurate performance up to 500-600 °C and reveal, for instance, the large sensitivity of the HKF model and its extrapolability to parameter calibration. The quartz solubility in low-density vapor is best reproduced by virial models or density approach with augmented functional form. We infer that for geochemical applications, the semi-empirical models using temperature, pressure and/or fluid density expansion (e.g., density models) are of superior quality to strictly physically based approaches. This provides basis for a new equation of state for aqueous species for simulating hydrothermal processes in high-temperature low-pressure settings.

1 Introduction

Mass transport by hydrothermal fluids is an essential mechanism for formation of diverse ore systems in magmatic-hydrothermal, orogenic, metamorphic and basinal settings (Yardley 2005, Williams-Jones and Heinrich 2005, Audétat 2019). Metal sequestration, transport and ore-mineral deposition are usually coupled to external factors (e.g., temperature and pressure gradients) or internal controls (e.g., acidity or redox changes during fluid-rock interaction; Reed 1997; Heinrich and Candela 2014). Our understanding of the fluid-mineral interaction inevitably relies on phase relations and chemical speciation in multicomponent systems and these equilibria are modeled by thermodynamic approaches (e.g., Reed 1998; Reed and Palandri 2006).

Since its introduction in 1980's, thermodynamic properties of aqueous solutes in hydrothermal fluids have been modelled with the Helgeson-Kirkham-Flowers equation of state and dataset (Tanger and Helgeson 1988; Shock et al. 1992). Despite of its attractiveness (extensive dataset, satisfactory performance in liquid-like fluids), the physical basis of this equation of state is not suitable for volatile constituents (e.g., CO_2, SO_2, H_2S, HCl, H_2) and for use in low-density fluids (e.g., Akinfiev and Diamond 2003). This severely limits the chemical-equilibrium modeling of upper-crustal magmatic and subvolcanic systems including porphyry, skarn, greisen and epithermal systems.

However, chemical equilibria in hydrothermal systems can be approached by alternative physico-chemical approaches available in fluid engineering and supercritical fluid extraction (e.g., Palmer et al. 2004, Leusbrock et al. 2008). In this contribution we revisit the physico-chemical principles in high-temperature aqueous systems and illustrate development of a new thermodynamic model designed to predict speciation, solubility and fluid equilibria in hydrothermal systems, with emphasis on low-pressure and low-density settings.

2 Theory

Thermodynamic modelling of aqueous solutes in fluids over wide range of density represents a long-standing challenge in physical chemistry. At low fluid density, the species are variably hydrated (short-range interaction), but long-range interactions between solute and solvent molecules are negligible. At high fluid density, the solvent has flexible but finite structure, where long-range (electrostatic and volumetric) interactions dominate and they can only be described by field continuum approaches (Fig. 1). As a result, no continuous formulation for thermodynamic properties of aqueous species from low to high fluid density is available, and this is a major drawback for modeling and interpretation of fluid-mineral interaction in magmatic-hydrothermal and epithermal systems.

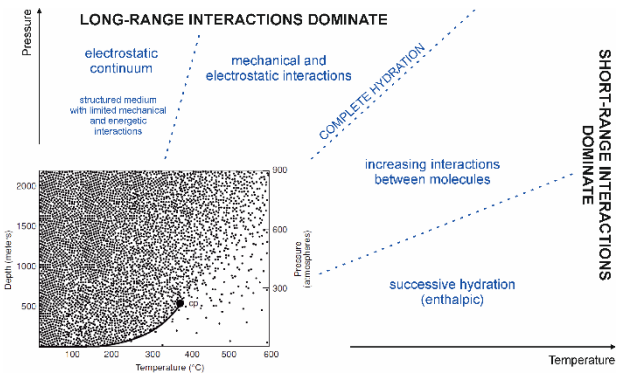

Figure 1. Schematic illustration of H_2O structure and solute-solvent interactions in the pressure-temperature space that define contributions to thermodynamic properties of aqueous species.

In low-density vapor, thermodynamic properties of the aqueous solute are conveniently modelled by introducing successively hydrated species in the gaseous standard state (hydration models). This approach is flexible and accurate at fluid density below ca. 0.1 g cm^{-3}. Its failure at greater densities indicates completion of the coordination sphere of water molecules around the solute species and the progressive onset of long-range interactions around the species. The fully hydrated state can be described: (1) empirically by correlating the thermodynamic properties with fluid density (density models) or, more simply, volume concentration of water (Mesmer et al. 1988, Marshall 2008). The functional form has been derived from several approximations to virial equation of state (Franck 1956, Akinfiev and Plyasunov 2013, Plyasunov 2020), although the temperature or density dependence of interaction parameters is often complex and does not allow extrapolation to very high pressures. At high fluid densities, the interaction field around the solute species has been traditionally described by Born electrostatic theory (electrostatic models; Helgeson et al. 1981, Tanger and Helgeson 1988). These models are physical for charged species, but their performance for volatile solutes and at low fluid density is limited. Several attempts have been made to bridge the hydration and long-range continuum approaches (semi-continuum models; Tanger and Pitzer 1989; Bandura and Lvov 2006). We will evaluate available models from each group in several model systems.

3 Applications

3.1 Dissociation of water

Dissociation of water, $H_2O = H^+ + OH^-$, is a principal speciation equilibrium in aqueous systems. It has been extensively investigated by experiments (638 measurements; Arcis et al. 2020) and modelled by hydration, density, electrostatic and statistical-mechanical approaches (Figs. 2-3).

The experimental data extend to 800 °C, but are essentially limited to fluid density between 0.4 and 0.9 g cm^{-3}. In practice, individual models remain fairly consistent up to 400 °C (at P = 500 bar), but remarkably diverge at higher temperatures (Fig. 2). At 800 °C, the discrepancy reaches 15 orders of magnitude and it provides a cautionary illustration of essentially non-existent constraints on ionic-species equilibria at magmatic temperatures and intermediate to low fluid densities. With decreasing pressure, the decreasing fluid density promotes ionic association, thus leading to substantial decrease in H_2O dissociation constant. At T = 600 °C, the experimental trend is accurately reproduced by density and semi-continuum models, whereas the conventional electrostatic approach (HKF; Tanger and Helgeson 1988; Shock et al. 1992) tends to be inaccurate below 1.5 kbar and non-physical below 1.0 kbar.

The H_2O dissociation has been used as a proxy for other ionic equilibria in hydrothermal fluids (Ryzhenko et al. 1985). Our evaluation defines the limitations of the electrostatic model (HKF) and highlights the potential of semi-continuum hydration and density models for high-temperature and low-pressure hydrothermal conditions.

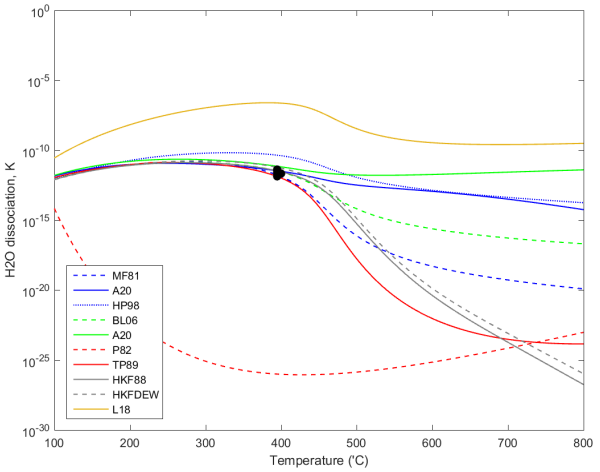

Figure 2. Variation of H_2O dissociation constant (K) with temperature at P = 500 bar. Color scheme: blue – density models; green – empirical hydration models; red – successive hydration models; yellow – statistical-mechanical models. Point symbols are experimental data.

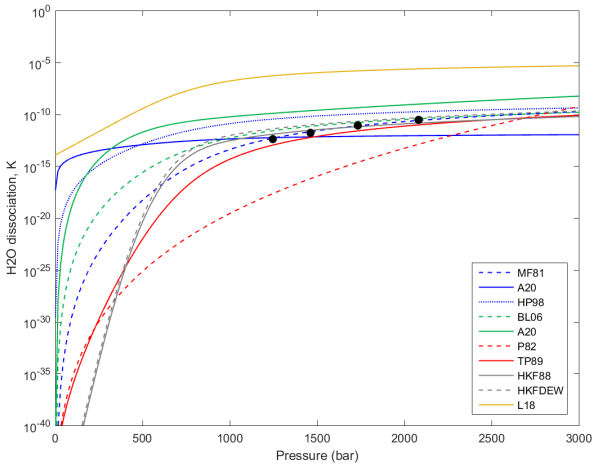

Figure 3. Variation of H_2O dissociation constant (K) with pressure at T = 600 °C. See Fig. 2 for symbol explanation.

3.2 Solubility of quartz

Solubility of quartz in aqueous fluid, expressed by generic equilibrium SiO_2 (qz) = SiO_2 (aq), provides a model system for mineral-fluid equilibria for the following reasons: (1) silica hydrate or silicic acid is a neutral species, stable over wide range of temperature, pressure and acidity; (2) solubility of quartz as a solid phase is low to moderate, hence solute-solute interaction effects remain negligible; (3) extensive coverage by experimental data (748 experiments; e.g., Dolejš and Manning 2010). In total, 16 thermodynamic models are available to predict the quartz solubility under hydrothermal conditions (Figs. 4-5).

The solubility of quartz in H_2O under moderate temperatures up to 500 °C (at P = 500 bar) is consistently and accurately reproduced by any of the thermodynamic approaches (Fig. 4). Above 500 °C, the electrostatic calibration by Sverjensky et al. (2014) and the density model by Holland & Powell (1998) start to deviate from experimental data, but other electrostatic (HKF) and density models maintain overall consistency up to 700 °C, as opposed to virial models (Fig. 4). The relative performance of individual physico-chemical approaches is best illustrated at subcritical conditions, where the differences in solubility in aqueous liquid vs. vapor are amplified (Fig. 5). At T = 300 °C, cannot be captured by miscellaneous, mainly advanced theoretical models. Likewise, the electrostatic (HKF) model does not approach the trend and magnitude of quartz solubility in steam. By contrast, the density models with augmented density dependence (Fournier and Potter 1982) or virial models offer accurate representation of experimental data.

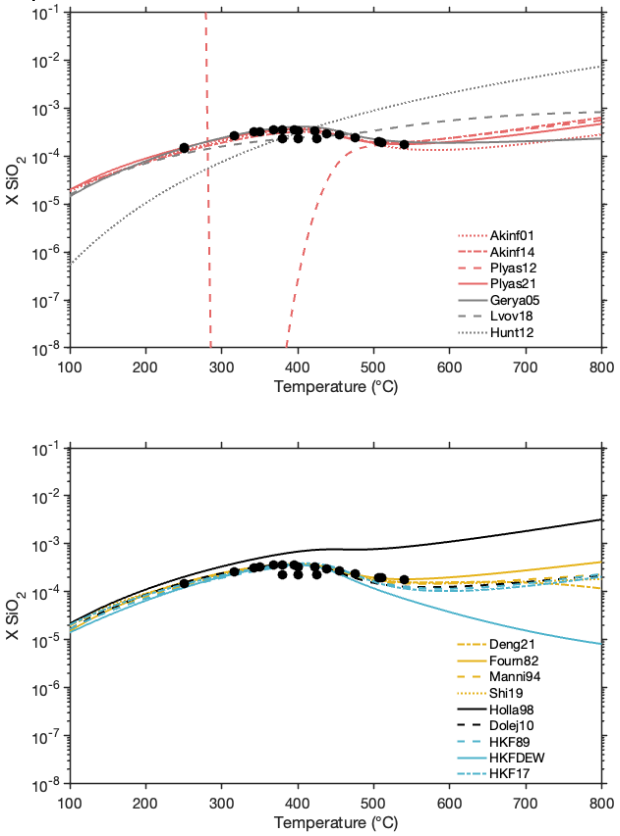

Figure 4. Variation of quartz solubility (expressed as mole fraction, X) with temperature at P = 500 bar. Legend: black – density models, blue – electrostatic models, gray – miscellaneous models, red – virial models, yellow – empirical density models. Point symbols are experimental data.

Overall, the quartz solubility data and models illustrate the limitations of the electrostatic (HKF) approach and emphasize the need for density-based or virial formulation for the thermodynamic properties of aqueous species in high-temperature and low-pressure (low-density) fluids.

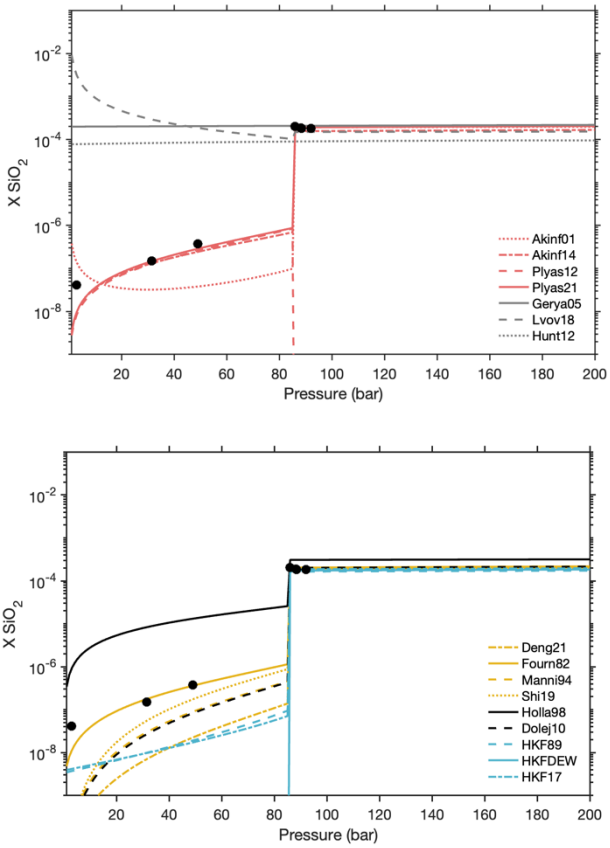

Figure 5. Variation of quartz solubility (expressed as mole fraction, X) with pressure at T = 300 °C. See Fig. 4 for symbol explanation.

4 Conclusions and outlook

This contribution illustrates the diversity of thermodynamic approaches to mineral solubility and aqueous speciation using several model systems. Equations of state for applications in geochemistry and ore formation are expected to provide reasonable extrapolation stability with respect to temperature, pressure or fluid density owing to limited experimental data and the need to cover complex, multicomponent systems. Statistical thermodynamics has offered several fundamental theories for model fluid systems (e.g., hard sphere fluid) and for solute-solvent interactions (e.g., scaled particle theory, fluctuation solution theory, mean spherical approximation). Despite their theoretical rigor, the pressure-temperature dependence of their parameters and leading terms is essentially unknown and difficult to constrain theoretically, unknown and this severely limits their application in geochemistry. In this sense, semi-theoretical or semi-empirical models that are primarily designed around temperature and pressure expansion of their thermodynamic functions are better suited for aqueous geochemistry and fluid-rock interaction.

Our approach is based on empirical comparison of a wide range of thermodynamic models with experimental data with (1) extensive coverage of the pressure-temperature space, and (2) constant and simple solute speciation. This includes solubility of oxide minerals (e.g., quartz) and speciation of

H_2O. Our critical assessment has revealed: (1) the conventional electrostatic (HKF) approach offers sufficient calibration flexibility to reproduce experimental data accurately, but not over a wide range of pressure-temperature conditions. The electrostatic approach cannot capture the trend and magnitude of solute properties in high-temperature and low-density fluids (below 1.0 kbar). (2) Models utilizing successive hydration offer large flexibility for speciation and solubility in low-density vapor, but their functional form is inappropriate and predictions meaningless when the full coordination by solvent has been achieved. (3) Density-based models appear to provide the best compromise between physically defined behaviour and limiting cases, extrapolation stability and accurate data reproducibility. Our intention is to formulate a new functional form for the thermodynamic properties of aqueous species that would extend to high temperatures and low pressures and thus open applications to ore formation in shallow magmatic, subvolcanic and epithermal systems.

Acknowledgements

This project has been financially supported by the German Research Council (DFG). We appreciate constructive editorial handling by Thomas Driesner.

References

Akinfiev NN, Diamond LW (2003) Thermodynamic description of aqueous nonelectrolytes at infinite dilution over a wide range of state parameters. Geochim Cosmochim Acta 67: 613-627

Akinfiev NN, Plyasunov AV (2013) Steam solubilities of solid MoO_3, ZnO and Cu_2O, calculated on a basis of a thermodynamic model. Fluid Phase Equil 338: 232-244

Arcis H, Ferguson JP, Cox JS, Tremaine PR (2020) The ionization constant of water at elevated temperatures and pressures: New data from direct conductivity measurements and revised formulations from T = 273 K to 674 K and p = 0.1 MPa to 31 MPa. J Phys Chem Ref Data 49: 033103

Audétat A (2019) The metal content of magmatic-hydrothermal fluids and its relationship to mineralization potential. Econ Geol 114: 1033-1056

Bandura AV, Lvov SN (2006) The ionization constant of water over wide ranges of temperature and density. J Phys Chem Ref Data 35, 15-30

Dolejš D (2013) Thermodynamics of aqueous species at high temperatures and pressures: equations of state and transport theory. Rev Mineral Geoch 76: 35-79

Dolejš D, Manning CE (2010) Thermodynamic model for mineral solubility in aqueous fluids: theory, calibration and application to model fluid-flow systems. Geofluids 10: 20-40

Fournier RO, Potter RW II (1982) An equation correlating the solubility of quartz in water from 25º to 900ºC at pressures up to 10,000 bars. Geochim Cosmochim Acta 46: 1969-1973

Franck EU (1956) Zur Löslichkeit fester Stoffe in verdichteten Gasen. Z Phys Chemie NF 6: 345-355

Heinrich CA, Candela PA (2014) Fluids and ore formation in the Earth's crust. Treatise Geochem 13: 1-28.

Helgeson HC, Kirkham D, Flowers GC (1981) Thermodynamic behavior of aqueous electrolytes at high pressures and temperatures. IV. Calculation of activity coefficients, osmotic coefficients, and apparent molal and standard and relative partial molal properties to 600ºC and 5 kb. Am J Sci 281: 1249-1516

Holland TJB, Powell R (1998) An internally consistent thermodynamic data set for phases of petrological interest. J Metam Geol 16: 309-343

Leusbrock I, Metz SJ, Rexwinkel G, Versteeg GF (2008) Quantitative approaches fot the description of solubilities of inorganic compounfs in near-critical and supercritical water. J Supercrit Fluids 47: 117-127

Marshall WL (2008) Aqueous electrolyte ionization over extreme ranges as simple fundamental relation with density and believed universal; sodium chloride ionization from 0º to 1000ºC and to 1000 MPa (10000 Atm.). Nat Prec 2008 (DOI: 10.1038/npre.2008.2476.1)

Mesmer RE, Marshall WL, Palmer DA, Simonson JM, Holmes HF (1988) Thermodynamics of aqueous association and ionization reactions at high temperatures and pressures. J Solut Chem 17: 699-718

Palmer DA, Fernández-Prini RJ, Harvey AH (eds, 2004) Aqueous systems at elevated temperatures and pressures. Physical chemistry in water, steam, and hydrothermal solutions. Elsevier, Amsterdam, 753 p

Plyasunov AV (2020) Predicting solubility of oxides of metals and metalloids in supercritical water. Ind Eng Chem Res 59: 970-980

Reed MH (1997) Hydrothermal alteration and its relationship to ore fluid composition. In Barnes HL (ed) Geochemistry of hydrothermal ore deposits (3ed). Wiley, New York: 303-365

Reed MH (1998) Calculation of simultaneous chemical equilibria in aqueous-mineral-gas systems and its application to modeling hydrothermal processes. Rev Econ Geol 10: 109-124

Reed MH, Palandri J (2006) Sulfide mineral precipitation from hydrothermal fluids. Rev Mineral Geochem 61: 609-631

Ryzhenko BN, Bryzgalin OV, Artamkina IY, Spassenykh MY, Shapkin AI (1985) An electrostatic model for the electrolytic dissociation of inorganic substances dissolved in water. Geochem Internat 22/9: 138-144

Shock EL, Oelkers EH, Johnson JW, Sverjensky DA, Helgeson HC (1992) Calculation of the thermodynamic properties of aqueous species at high pressures and temperatures: effective electrostatic radii, dissociation constants and standard partial molal properties to 1000ºC and 5 kbar. J Chem Soc, Faraday Trans 88: 803-826

Sverjensky DA, Harrison B, Azzolini D (2014) Water in the deep Earth: The dielectric constant and the solubilities of quartz and corundum to 60 kb and 1200 ºC. Geochim Cosmochim Acta 129: 125-145

Tanger JC IV, Helgeson HC (1988) Calculation of the thermodynamic and transport properties of aqueous species at high pressures and temperatures: revised equations of state for the standard partial molal properties of ions and electrolytes. Am J Sci 288, 19-98

Tanger JC IV, Pitzer KS (1989) Calculation of the thermodynamic properties of aqueous electrolytes to 1000 ºC and 5000 bar from a semicontinuum model for ion hydration. J Phys Chem 93: 4941-4951

Williams-Jones AE, Heinrich CA (2005) Vapor transport of metals and the formation of magmatic-hydrothermal deposits. Econ Geol 100: 1287-1312

Yardley BWD (2005) Metal concentrations in crustal fluids and their relationship to ore formation. Econ Geol 100: 613-632

Complex genetic model of the shear-zone hosted epithermal Au-Ag-Pb-Zn-Cu deposit Banská Hodruša at the Rozália mine, Slovakia

Peter Koděra[1], Jaroslav Lexa[2], Martin Chovan[1], Rastislav Vojtko[1], Alexander Kubač[3], Bertrand Rottier[4], Matej Rybárik[1], Ján Prcúch[5]
[1]Faculty of Natural Sciences, Comenius University, Bratislava, Slovakia
[2]Earth Science Institute, Slovak Academy of Sciences, Bratislava, Slovakia
[3]State Geological Institute of D. Štúr, Bratislava, Slovakia
[4]Département de Géologie et Génie Géologique, Université Laval, Québec, Canada
[5]Slovenská Banská, Ltd., Hodruša-Hámre, Slovakia

Abstract. Banská Hodruša intermediate sulfidation gold-rich deposit is hosted by a low-angle shear zone in the centre of the Neogene Štiavnica stratovolcano. It occurs on the historical Rozália mine, where base metal stockwork mineralisation and Cu-rich veins were mined in the past too. Geological evolution started with the emplacement of a granodiorite pluton, followed by its rapid exhumation and related sector collapse of the volcano at the base with the flat shear zone, later penetrated by quartz-diorite sills and final resurgent horst uplift related to accumulation of residual rhyolitic magma in the magma chamber. Tectonic events include cracking of the apical part of granodiorite on cooling and hydraulic fracturing, development of ring and subhorizontal structures above the granodiorite due to the relative subsidence of the central block into the chamber, two-stage formation of faults in the shear zone and final creation of steep faults related to the resurgent horst uplift. Hydrothermal events include exsolution of fluids from the granodiorite magma and their heterogenization, long-lasting fluid exsolution from the upper-crustal magma chamber and finally fluid exsolution from the residual rhyolitic magma. Supercritical fluids subsequently penetrated contraction cracks, andesite-granodiorite contact, shear zone, horst faults and they were variably affected by fluid mixing and boiling.

1 Introduction

The Au-Ag-Pb-Zn-Cu epithermal deposit Banská Hodruša of intermediate-sulphidation type is located in the central zone of Middle Miocene Štiavnica stratovolcano on the inner side of the Carpathian arc. It is the last active ore mine in Slovakia, with estimated total production ~10 t Au and 6 t Ag (Kubač et al. 2018). This deposit occurs at the historical Rozália mine 400–650 m below the current surface and it represents an unusual subhorizontal multi-stage vein system, hosted by a shear zone, corresponding to a low-angle normal fault zone (LANF). Epithermal Au-rich ore has been exploited here since 1992, but in the past this mine was also used to exploit steep Cu-Pb-Zn epithermal veins and a base-metal stockwork mineralization.

During the last decades, a considerable amount of geological, petrological, structural, mineralogical, geochemical and genetic data were obtained from this area (Table 1). This work presents a review of these data that are used to develop a complex genetic model of the deposit, including other spatially and genetically associated types of mineralisations present at the Rozália mine (Fig.1).

2 Mineralisations at the Rozália mine

The Au-Ag-Pb-Zn-Cu epithermal veins, hosted by the shear zone, occur in the pre-caldera andesites near the flat roof of a granodiorite pluton. The ore deposit developed in several stages (Kubač et al. 2018). The early stage consists of low-grade silicified breccia at the base of the deposit, occurring along E-W oriented subhorizontal structures dipping 20-30° to SE. The main ore mineralisation consists of stockwork of early steep veins (E-W, 40-60° to S) and a later system of veins inside the shear zone (NE-SW, ~45° to SE), accompanied by complementary detachment-hosted veins (<30°) in the roof of the shear zone. Veins consist of early quartz-rhodonite assemblage (incl. Mn-carbonates, chlorite) and later sulphide-gold assemblage (incl. sphalerite, galena, chalcopyrite, pyrite, rare Te-minerals and various gangue minerals). Mined ore contains 14 g/t Au, 17 g/t Ag, 0.6% Zn, 0.45% Pb, and 0.15% Cu in average. The shear zone was intruded by mostly post-mineralisation system of quartz-diorite porphyry sills. Post-ore veins include rare barren quartz veins of variable orientation mostly hosted by the porphyry. Major veins are accompanied by adularia, quartz and illite. Strong argillisation (illite ± quartz, pyrite) occurs in the roof of the shear zone (Koděra et al. 2017).

The stockwork mineralisation occurs some 1.5 km south of the Au-Ag deposit, mostly hosted by apical porphyritic part of the granodiorite pluton. It resembles a porphyry hydrothermal system including potassic alteration in the granodiorite, and advanced argillic alteration in overlying pre-caldera andesite (Koděra et al. 2004). Mined ores contained 2.5% Pb, 3.5% Zn, 0.4% Cu, 10 g/t Ag. Ore grades and intensity of potassium alteration decrease with depth.

The steep epithermal veins (50–70° to NE–SW) cut the base-metal stockwork, the gold-rich veins as well as quartz-diorite porphyry sills. They belong to an extensive system of veins in the central zone of the volcano with a zonal arrangement (Pb-Zn-Cu, Ag-Au, Au-Ag) and multi-stage filling (Kovalenker et al. 1991). At the Rozália mine the most important is the Rozália vein, mined for Cu-rich base metal ore (0.5 - 0.8% Cu, 0.2% Pb, 0.3% Zn, 10-20 g/t Ag, 0.1-0.2 g/t Au).

<table>
<tr><th>Stage</th><th colspan="2">I</th><th>II</th><th>III</th><th colspan="2">IV</th><th>V</th><th>VI</th></tr>
<tr><td>Age</td><td colspan="2">13.6 Ma</td><td colspan="4">13.6 – 13.5 Ma</td><td>13.5 – 13.0 Ma</td><td>12.2 - 11.4 Ma</td></tr>
<tr><td rowspan="2">Mineralisation / host rock</td><td rowspan="2">Fe-skarns / basement carbonates</td><td rowspan="2">Advanced argillic alteration / andesite</td><td rowspan="2">Pb-Zn-Cu stockwork / apical part of granodiorite & andesite</td><td rowspan="2">Silicite / subhorizont. structures in andesite in contact with granodiorite</td><td colspan="2">Shear-zone hosted epithermal Au-Ag-Pb-Zn-Cu veins / andesite</td><td rowspan="2">Post-mineralisation Qtz veins / andesite & Qtz-diorite porphyry</td><td rowspan="2">Pb-Zn-Cu-Ag-Au horst veins / andesite & Qtz-diorite porphyry</td></tr>
<tr><td>Qtz-Rdn vein filling</td><td>Sulf-Au vein filling</td></tr>
<tr><td rowspan="2">Geological evolution</td><td colspan="2" rowspan="2">Emplacement of granodiorite pluton between prevolcanic basement and andesite, cooling, fluid exsolution during its crystallization</td><td colspan="4">Fluid saturation in magma chamber, migration of fluid-saturated magma between subsiding basement and granodiorite pluton together with continuous granodiorite uplift and exhumation</td><td rowspan="2">Final magma chamber cooling, cupola of fluid-saturated rhyolitic magma, horst uplift, fluid penetration into deep horst faults</td></tr>
<tr><td>Penetration of fluids into contraction cracks</td><td>Penetration of fluid into andesite-granodiorite contact</td><td colspan="2">Sectoral collapse of volcano at the base with argillites, fluids-filled structures, and basement carbonates; fluid penetration in the shear zone</td><td>Emplacement of most sill of Qtz-diorite porphyry</td></tr>
<tr><td>Tectonic evolution</td><td colspan="2">Contraction cracking of granodiorite during cooling in subsolidus conditions</td><td>Fracturing due to relict contractional stress & hydraulic fracturing</td><td>Subhorizon. structures above the granodiorite & hydraulic fracturing</td><td>Initial N-S movement on shear zone</td><td>NW-SE reorientation of movement on shear zone</td><td>Ring and subhorizontal structures at sides and above granodiorite</td><td>Resurgent horst uplift in caldera centre, system of steep faults</td></tr>
<tr><td rowspan="2">Fluid evolution</td><td colspan="2">Heterogenisation of fluids exsolved from granodiorite magma</td><td colspan="5">Continued fluid exsolution from magma chamber, ascend in the form of supercritical fluids</td><td>Ascend of supercritical fluids</td></tr>
<tr><td>Brine cooling & mixing with meteoric water</td><td>Vapor condensantion</td><td>Mixing of magmatic - meteoric fluids</td><td>Cooling of magmatic fluids</td><td colspan="2">Boiling of magmatic fluid due to decompression</td><td>No data</td><td>Boiling and mixing of magmatic - meteoric fluids</td></tr>
</table>

Table 1. Summary of geological, tectonic and fluid evolution related to all major types of mineralisation in the Rozália mine in Banská Hodruša. Ages are based on data of Chernyshev et al. (2013) and Lexa et al. (2019).

3 Geological evolution

Stages of evolution related to mineralisation at the Rozália mine (Table 1, Fig. 1) are interpreted based on the structural and magmatic evolution of the Štiavnica stratovolcano (Chernyshev et al. 2013, Rottier et al. 2019) and dating of subvolcanic intrusions and caldera filling (Lexa et al. 2019). The most characteristic features of the volcano include an extensive caldera, a late-stage resurgent horst in the caldera centre and a large subvolcanic intrusive complex. Magmas associated with the hydrothermal mineralization were sourced from an upper crustal reservoir (1 to 3 kbar at 960 to 700 °C) that was active more than 3 million years. Ore deposits formed during periods of reservoir cooling when the residual melt reached fluid saturation.

The first evolutionary stage associated with mineralisations at the Rozália mine is related to the emplacement of the granodiorite magma between the prevolcanic basement and the pre-caldera andesite at a minimum depth of ~2 km (13.6 Ma). The intrusion has a relatively flat roof, probably as a consequence of a descent of the central block of basement rocks into the upper crustal magmatic reservoir, compensated by the displacement of magma above the block. On cooling and progress of crystallization, exsolution of fluid appeared, which was responsible for adjacent Fe-skarn mineralisation and advanced argillic alteration in the apical part of the pluton (Koděra et al. 2014).

During the next four evolutionary stages, cooling and possibly mixing of the magma in the reservoir, evidenced by thermobarometry and petrography, led to its saturation by fluids and their exsolution. This caused a decrease in magma density and its migration and emplacement between the subsiding basement block and the granodiorite intrusion. Magma decompression in turn accelerated the fluid exsolution. These fluids migrated upwards using contraction cracks forming the base metal stockwork hydrothermal system (Stage 2) and later they penetrated the andesite-granodiorite contact forming barren silicites (Stage 3). The continuous emplacement of the fluid-saturated magma was also responsible for a rapid resurgent uplift and exhumation of the granodiorite pluton, finally leading to a sector collapse of the volcano, at the base with argillites, fluids-filled structures, and basement carbonates (Stage 4). Fluid penetration along a flat shear zone at the base of the collapse was responsible for the currently mined Au-rich veins. The accumulation of differentiated magma of lower density in the magmatic reservoir finally led to the emplacement of the post-mineralisation system of sill and dykes of quartz-diorite porphyry (13.5 – 13.0 Ma), especially using structures of the shear zone, and terminated the gold-forming hydrothermal activity in the area of the Rozália mine (Stage 5).

Subsequent geological evolution of the volcano did not directly affect mineralisation at the mine. It was represented by a caldera subsidence linked with extrusive activity of evolved andesites and post-caldera andesitic effusive activity. However, fluid saturation was not reached, as magma was relatively hot (up to 970 °C), probably due to large inputs of mafic magma into the upper-crustal reservoir.

The last evolutionary stage at the mine (Stage 6) is related to the final cooling of the magma chamber (<750 °C), when a cupola of fluid-saturated rhyolite magma developed in the chamber, representing

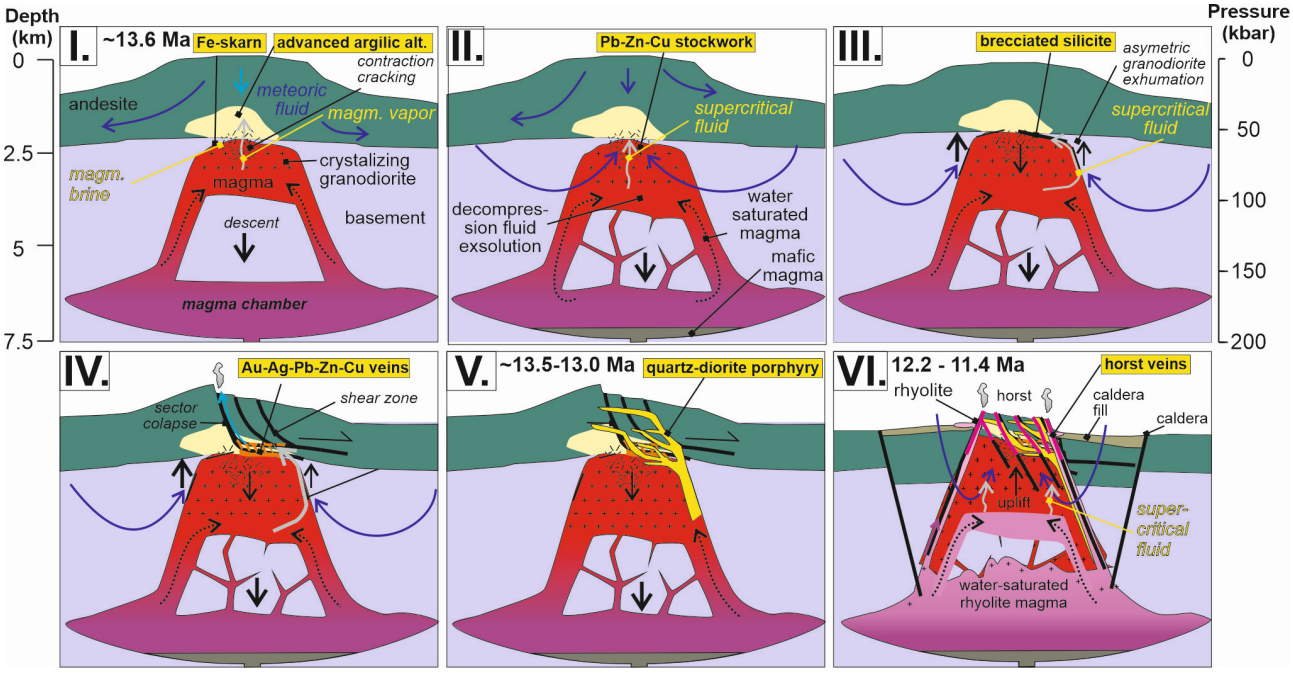

Figure 1. Stages and timing of geological evolution related to various mineralisation types at the Rozália mine, including corresponding tectonic and fluid evolution. See text and Table 1 for details.

interstitial melt segregated from the crystal mush. low density of the fluid saturated magma resulted in an uplift of the central zone of the volcano, forming a resurgent horst dome, and emplacement of rhyolite dikes and domes (12.2 - 11.4 Ma, outside the mine). Penetration of exsolved fluid into deep horst faults resulted in an extensive system of horst-related epithermal veins.

4 Tectonic evolution

Tectonic events and development of fractures were important for creation of fluid flow paths and the origin of various mineralisations at the Rozália mine. Tectonic evolution related to mineralisation is based on regional-scale and mine-scale structural analyses (Nemčok et al. 2000; Kubač et al. 2018).

The early base metal stockwork is related to a relict contractional stress in the granodiorite during cooling of the apical part of the intrusion, further enhanced by hydraulic fracturing. The resulting network of fractures enabled migration of fluids exsolving from the magma reservoir.

Silicites and silicified breccias of hydraulic fracturing on subhorizontal structures at the andesite-granodiorite contact are linked to the subsidence of the basement block into the upper-crustal magma chamber, including the solidified granodiorite pluton. Magmatic fluids released from the chamber penetrated the contact at a pressure close lithostatic.

Epithermal Au-Ag-Pb-Zn-Cu veins are related to the origin of the shear zone during the sector collapse of the volcano and the shear zone creation. The early movement on the shear zone was N-S oriented, forming an early stockwork of E-W oriented veins. Later movements on the shear zone were NW-SE oriented, forming a later system of veins of NE-SW orientation. Post-ore emplacement of quartz-diorite porphyry magma was enabled by the same subhorizontal structures as the ore veins and fed from ring structures, both related to the reactivated underground cauldron subsidence of the central block.

Latest base metal epithermal veins are hosted by a complex system of steep NE–SW oriented faults related to the long-lasting resurgent horst uplift.

5 Fluid evolution

Evolution of fluids related to the various stages of mineralisation at the mine is interpreted from stable isotope, fluid inclusion and illite thermometry data from the skarn and base metal stockwork mineralisation (Koděra et al. 2004), from the gold-rich veins (Koděra et al. 2005; Kubač et al. 2018) and from the horst-related base metal veins (Kovalenker et al. 1991, Koděra et al. 2005), including recent LA ICMPS of fluid inclusions (Koděra et al. 2019, 2021).

Inclusions in quartz from the granodiorite showed that the magmatic fluid exsolved from the granodiorite magma experienced a phase separation into a hot (>600°C) hypersaline brine (up to 71 wt % NaCl eq.) and a vapor. Skarn mineralisation was produced from the brine mixed with meteoric water (215°–370°C, up to 23 wt% NaCl eq.). Coeval advanced argillic alteration above the apical part of the granodiorite pluton originated from condensed magmatic vapor (191°–367°C, up to 5 wt% NaCl eq.).

Base metal stockwork ore crystallised from fluids showing a positive correlation between salinity (5 - 0.5 wt.% NaCl eq.) and temperature (330 - 190 °C), indicative for mixing of magmatic and meteoric

fluids, also confirmed by combined O and H isotope data. The absence of boiling due to pressure constraints (granodiorite was still not sufficiently uplifted) could explain the absence of gold in ores.

Fluids associated with the gold-rich, shear-zone hosted veins had salinities (1-4 wt.% NaCl eq.) and temperatures (~250-310 °C) similar to the stockwork. Gold precipitation was mostly induced by boiling of decompressed fluids evolving from suprahydrostatic to hydrostatic conditions at a depth of ~550 m. Boiling in this subhorizontal system of veins was mostly related to opening of dilatational structures that enabled an active suction of fluids and their decompression. The main migration of paleofluids occurred along low-angle normal faults of the shear zone from S-SE to N-NW, as indicated by the geological setting of the quartz-diorite porphyry sills that intruded the shear zone at the end of the hydrothermal activity from S-SE. The main ore mineralisation is associated with areas with densely distributed dilatational structures, where both major boundaries of the shear zone were relatively close together, i.e. where the hanging-wall argillite was relatively close to foot-wall silicite. The strongly argillised upper boundary of the shear zone probably worked as a collector of hydrothermal fluids flowing along the shear zone, as well as a collector of vapour and gases escaping from boiling fluids throughout the entire thickness of the shear zone.

Fluids associated with the base metal horst-related veins have wide ranges of salinities (0.5 - 11.5 wt.% NaCl eq.) and temperatures (360 - 110 °C), related to their multistage filling, with evidence for boiling and mixing of fluids.

Magmatic fluids associated with the base metal stockwork and all epithermal mineralisations show increased B, As and Sb contents which indicates that these vapor-affiliated elements were not lost during fluid heterogenisaton on ascent from the magma chamber. Thus, the fluid source was likely supercritical in nature, later contracted to liquid. The relatively constant composition of most inclusions (including metals) indicates a common long-lasting source of the fluids exsolved from the magma chamber. Furthermore, the composition of silicate melt inclusions from corresponding coeval magmatic rocks (Rottier et al. 2019) is in a good agreement with published fluid-melt fractionation factors.

6 Conclusions

The presented complex genetic model of the epithermal gold deposit and associated mineralisation types at the Rozália mine includes a sequence of events that started with the emplacement of a granodiorite pluton. Fe-skarns and advanced argillic alteration are related to heterogenisation of a fluid exsolved from the granodiorite magma. It follows fluid exsolution from the upper crustal magma chamber and penetration of supercritical fluids into contraction cracks in the intrusion, resulting in the origin of Pb-Zn-Cu stockwork mineralization due to mixing with meteoric water. Gold-rich veins hosted by the shear zone are related to the rapid exhumation of the granodiorite, sector collapse of the volcano and penetration of the shear zone by supercritical fluids which were affected by boiling due to decompression. This hydrothermal activity was terminated by the emplacement of quartz-diorite porphyry sills in the shear zone. The latest base metal vein mineralisation at the mine is related to the development of a fluid-saturated residual magma in the magma chamber, resulting in a resurgent horst uplift and a system of steep faults, penetrated by supercritical fluids, later affected by boiling and mixing with meteoric water.

Acknowledgements

This work was supported by grants VEGA No. 1/0313/20 and APVV-15-0083.

References

Chernyshev IV, Konečný V, Lexa J, Kovalenker VA, Jeleň S, Lebedev VA, Goltsman YuV (2013) K-Ar and Rb-Sr geochronology and evolution of the Štiavnica Stratovolcano, Central Slovakia. Geol Carpath 64:327-351.

Koděra P, Lexa J, Rankin AH, Fallick AE (2004) Fluid evolution in a subvolcanic granodiorite pluton related to Fe and Pb-Zn mineralization, Banská Štiavnica ore district, Slovakia. Econ Geol 99:1745-1770.

Koděra P, Lexa J, Rankin AH, Fallick AE (2005) Epithermal gold veins in a caldera setting: Banská Hodruša, Slovakia. Miner Depos 39:921-943.

Koděra P, Kubač A, Uhlík P, Osacký M, Vojtko R, Chovan M, Lexa J, Žitňan P (2017) Hydrothermal alteration of a shallow-dipping epithermal Au-Ag-Pb-Zn-Cu deposit Banská Hodruša, Slovakia. Proc 14th SGA Bien Meeting, Québec City, Canada, Vol 1: 159-162.

Koděra, P., Kubač, A., Uhlík, P., Vojtko, R., Chovan, M., Lexa, J., Milovský, R., Laurent, O., Fallick E.A., 2019: Fluid evolution and genesis of epithermal gold deposit hosted by a shear-zone: Banská Hodruša. Proc 15th Biennial SGA Meeting, 3, 1042 - 1045.

Koděra P, Kubač, A., Lexa J, Rottier, B., Laurent, O., 2021: External controls govern metal endowment and styles of ore mineralisation in andesite volcanoes – example from the Štiavnica stratovolcano, Slovakia. In Proc 16th Biennial SGA Meeting, 2, 96.

Kovalenker, V.A., Jeleň, S., Levin, K.A., Naumov, V.B., Prokofjev, V.J., Rusinov, V.L., 1991: Mineral assemblages and physical-chemical model of the formation of gold-silver-polymetallic mineralisation on the deposit Banská Štiavnica (Central Slovakia). Geol Carpath, 42, 291 - 302.

Kubač A, Chovan M, Koděra P, Kyle JR, Žitňan P, Lexa J, Vojtko R (2018) Mineralogy of the epithermal precious and base metal deposit Banská Hodruša at the Rozália mine (Slovakia). Miner Petrol 112:705–731.

Lexa, J., Rottier, B., Yi,K., Audétat, A., Broska, I., Koděra, P., Kohút, M. 2019: Magmatic evolution of the Štiavnica volcano. Proc. Geol Carpath 70 Internat. Conf., 5 pp.

Nemčok M, Lexa O, Konečný P (2000) Calculations of tectonic, magmatic and residual stress in the Štiavnica Stratovolcano, Western Carpathians: implications for mineral precipitation paths. Geol Carpath 51: 19-36

Rottier, B., Audétat, A., Koděra, P., Lexa, J., 2019: Magmatic evolution of the mineralized Štiavnica volcano (Central Slovakia): Evidence from thermobarometry, melt inclusions, and sulfide inclusions J Volcan Geoth Res, 401, 106967.

Numerical simulations of pulsed epithermal ore-forming events in geothermal systems with incrementally growing magma reservoirs

Maximilian Korges[1], Philipp Weis[1,2]
[1]Institute of Earth and Environmental Science, University of Potsdam, Potsdam, Germany
[2]GFZ German Research Centre for Geosciences, Potsdam, Germany

Abstract. Numerical models can provide unique insights into the temporal and spatial relationships of ore-forming processes. We use a model for magma reservoir growth to investigate the impact of sill injection rates on the hydrothermal system. The simulations with more episodic, low injection rates (<1.3 x10^{-3} km³/y) result in a highly variable fluid plume which allows almost pure magmatic fluids to migrate to shallower and cooler regions where they can phase separate and potentially form epithermal ore deposits. The modelling results point towards a relatively short time span of potential ore formation of a few thousands of years until the magmatic fluid plume retreats. Long-lived magma reservoirs which are forming at higher injection rates hamper the formation of high-grade epithermal deposits, but are more favourable for high-grade porphyry Cu deposits.

1 Introduction

Epithermal ore deposits are important resources for various precious (e.g. Au, Ag) and base (e.g. Cu, Pb, Zn) metals. They form within the uppermost 1.5 km of Earth's crust by circulation of hydrothermal fluids through fractured and porous rocks in geothermal and volcanic systems (Hedenquist & Arribas, 2022). The ore-forming fluids can be of pure meteoric or magmatic origin (potentially also including seawater), or variable mixtures of these end-members. Low-sulfidation epithermal deposits are characterized by low to moderate sulphur contents in the hydrothermal fluids, while high-sulfidation deposits have high sulphur contents, which is typically inferred to be related to a stronger influence of magmatic volatiles. High-sulfidation deposits can form at temperatures of 200-300°C (Hedenquist et al. 2000; Hedenquist & Arribas, 2022), which requires cooling of ascending magmatic (-dominated) fluids compared to volcanic fumaroles.

Many hydrothermal veins in epithermal deposits show evidence for pulsed ore formation with high metal contents limited to distinct growth zones. As a particularly efficient mechanism for metal enrichment to economic grades, transport and precipitation of precious metals has been proposed to occur by isochemical contraction of a single-phase magmatic vapor (which originated from an underlying magmatic-hydrothermal system where phase separation occurred) followed by a second phase-separation event of near-surface boiling (Heinrich et al. 2004). However, the timing and duration of epithermal mineralization as well as the evolution and state of the underlying, driving magmatic systems within the crust are still debated. The total time of ore precipitation has been suggested to be less than 10 kyrs (e.g. Moncada et al. 2019), but the relationship to a magmatic system, which can be active for several hundreds of thousand years (Schöppa et al, 2017), remains unclear.

We used numerical models to investigate the connection of magma reservoir formation by incremental growth, fluid flow above a magmatic system and phase separation at shallow depths. The simulations are based on studies evaluating the formation of porphyry Cu deposits with connected distal epithermal mineralization (Korges et al. 2020). The numerical models focus on the physical hydrology by using non-linear fluid and rock properties, but so far cannot resolve the evolution of sulphur contents and other chemical fluid properties (e.g. pH, redox state). Nevertheless, they can give new insights into processes that are typically not exposed in active geothermal systems or preserved within the deposits.

2 Methods

Numerical simulations of magmatic-hydrothermal systems using CSMP++ have previously prescribed one large magmatic intrusion during model initialization (Weis et al., 2012). We have developed a new functionality that allows to resolve sill injection events as hot horizontal sheets of magma at variable intervals (Figure 1; Korges et al., 2020).

We assume that the simulated magma reservoirs grow from the top downwards by injecting the sills at a constant depth of 5 km and moving the mass and energy conserving variables of the control volumes within and below the sill location downwards. Sills are injected episodically after a specified time interval according to a time-integrated average magma flux. Every sill is represented by a selection of computational nodes spanning a total width of about 10 km and a thickness of 400 m.

All simulations start with an initial intrusion (3 sills in height) and are followed by 8 further intrusion events of single sills every 2.5, 15, or 30 thousand years of simulation time until the total volume of injected magma reaches approximately 210 km³ (11 sills). The different intervals correspond to average magma injection rates ranging from 7.5 x 10^{-3} km³/y to 0.6 x 10^{-3} km³/y.

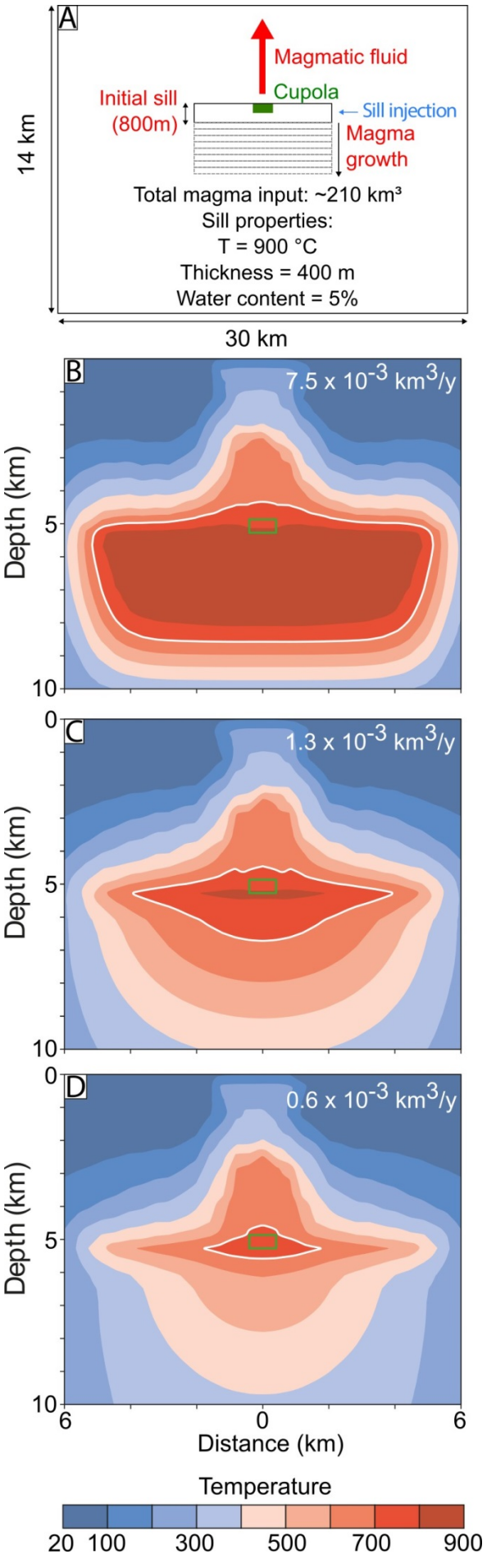

Figure 1. A Modelling setup and initial condition of the sills. The green box refers to the fluid injection location of the magma chamber (cupola). **B-D** Magma chamber dimensions after last sill injection with decreasing injection rate from B to D. All magma chambers show the state at 4 kyrs after the last sill. White lines correspond to the solidus temperature of 700°C. Adapted from Korges et al., 2020.

Saline magmatic fluids (10 wt% NaCl) are released through the central top part of the magma chamber, assuming a focussing mechanism within the magmatic system (e.g. Lamy-Chappuis et al., 2020) by processes unresolved in the simplified model used in this study. This "cupola" region is 800 m wide and has a fixed location. The spatial distribution of magmatic fluids during the evolution of the modelled system is monitored as a passive tracer. For the hydrothermal system, we apply a dynamic permeability model with depth-, temperature-, and pressure-dependent variations related to the brittle-ductile transition and hydraulic fracturing (Weis et al., 2012). The host rock is initially saturated with pure water to represent meteoric fluids.

3 Results

3.1 High magma-injection rate

High sill injection rates (7.5 x 10^{-3} km³/y) result in rapid growth of a magma chamber with a vertical extent of 2-3 km while retaining the initial horizontal sill width (Figure 1B; Korges et al., 2020). During sill intrusion and after the last sill, the formed magma chamber contains regions with high melt contents and therefore also high amounts of fluid. The cooling rate of the magma reservoir thus leads to a continuous fluid release in which the event of the sill injection only has a minor influence on the extension of the fluid plume (Figure 2; videos of the fluid plumes are visualized in Korges et al. (2023)).

The magmatic water fraction in the near-surface epithermal domain is constant during the cooling of the system and only shows small variations over time with values of around 0.7 (referring to 70% of magmatic fluid and 30% of meteoric fluid). Due to the steady fluid release rate, the temperature distribution within the fluid plume is also stable over time (Figure 3). Figure 2 further displays the saturation of vapor within the fluid plume and at the surface, which is only slightly variable during the simulation.

3.2 Low magma-injection rate

Low sill injection rates of 1.3 x 10^{-3} km³/y or 0.6 x 10^{3} km³/y result in a small magma chamber or complete crystallization between the sill emplacements, respectively (Figures 1C, D; Korges et al., 2020). Therefore, each new sill is injected in a cooler environment with (almost) no preserved melt, resulting in rapid cooling of the new intrusion and therefore high fluid release rates. The expelled magmatic fluid can reach the surface with magmatic

water fractions of 0.9 to 1 (almost pure magmatic fluid) for up to 1000 years after each pulse (Figure 3).

Due to the more dynamic fluid plume, the host rock at this region is cooler compared to fast-injection setups and, thus, even though the magmatic fluids dominate, the temperatures still first remain below 200°C due to thermal equilibration with the host rock. During the fluid release event, the host rock close to the surface gets heated to similar temperatures as in the high injection-rate setting (ca. 240°C). At these temperatures, the magmatic water fraction already starts to decrease because most fluids have left the magma reservoir due to its rapid cooling after sill injection. 3000 to 4000 years after the sill intrusion, the fluid plumes in the slow settings decline, while the host rock at the surface keeps the elevated temperatures for several more thousands of years, again due to thermal buffering in the rock-dominated porous medium (Figure 3).

The occurrence of phase separation within the fluid plume in the simulation with lower injection rates is also more heterogeneous, with a decrease in the area of phase separation between pulses compared to the constant vapor region at higher rates (Figure 2). At the lowest simulated frequencies, phase separation at depth ceases before the next sill injection. In contrast, phase separation in the shallow epithermal regions persists over time in all settings. Larger regions with higher degrees of vapor saturation tend to form slightly after the magmatic fluid reaches the surface.

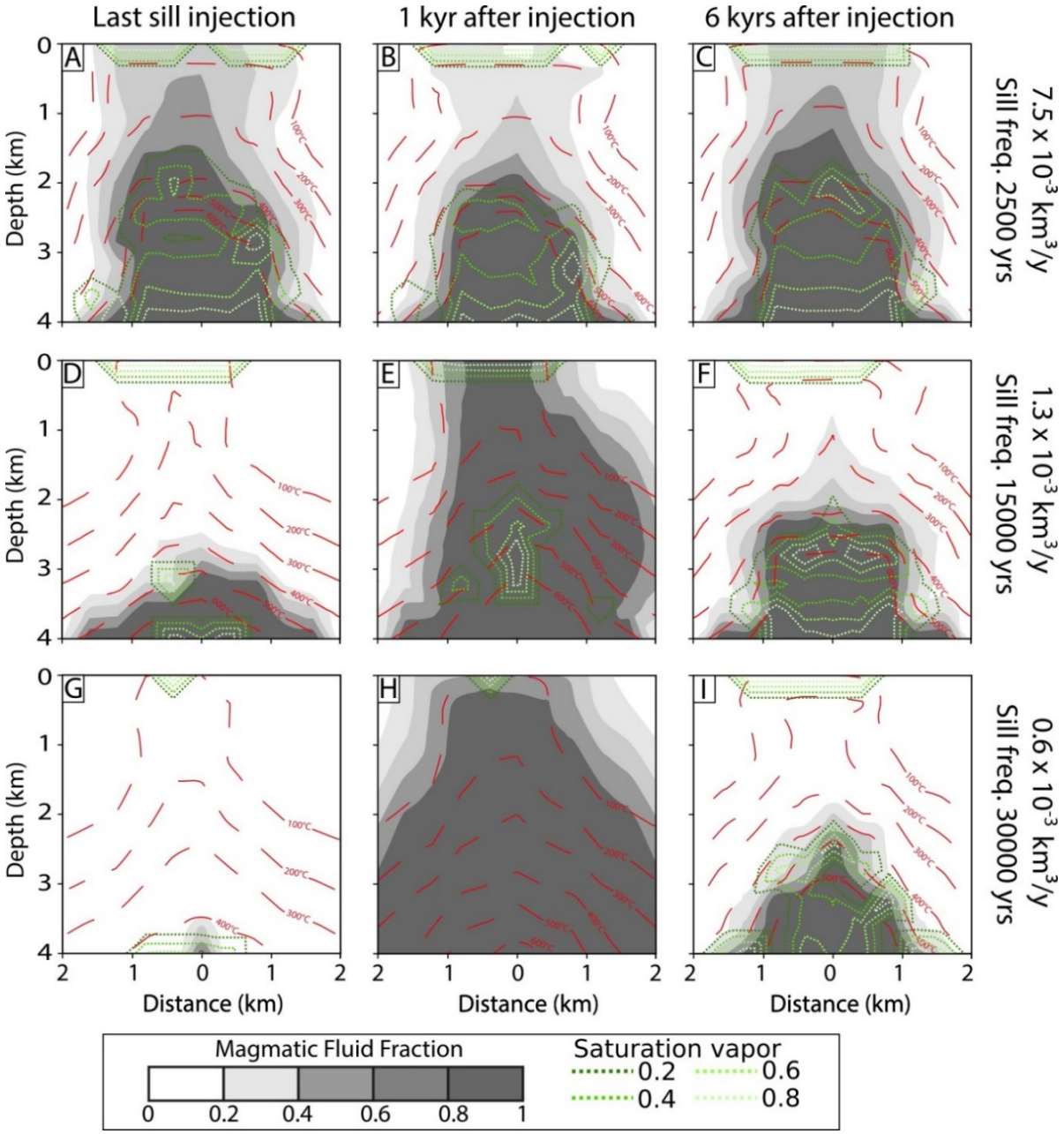

Figure 2. Fluid plumes above the cupola region of the magma reservoir (injection location at 5 km depth). **A-C**: High sill injection rates result in a steady fluid plume and little variations in fluid properties at the surface. **D-F**: Low injection rates result in a small magma chamber and a distinct impact of the sill injection on the fluid plume. **G-I**: The lowest used growth rate leads to a complete crystallization of the magma reservoir and a high impact of each sill injection on the fluid plume.

4 Discussion and Conclusions

The formation of high-sulfidation epithermal deposits requires large amounts of metal-enriched fluids at shallow depths. Our numerical simulations suggest that these conditions are more likely for a magmatic environment that produces distinct events of fluid exsolution and thus in settings with a rather low magmatic influx rate of <1.3 x 10^{-3} km³/y. At these conditions, almost pure magmatic fluids can reach the epithermal domain, while the temperature regime is still dominated by the geothermal system that was prevalent before the fluid release event and agrees with high-sulfidation epithermal mineralization at 200-300°C (Hedenquist et al. 2000; Hedenquist & Arribas, 2022). Our simulations do not produce volcanic fumaroles at higher temperatures.

The simulations point toward the possibility of pure magmatic fluids at the surface which did not undergo previous phase separation at greater depth, although it only occurred for a short time period of less than 500 years. For most settings, two phase-separation events occur at different depths. Phase separation at depth can allow the fast-ascending vapor to contract and phase separate again at the surface. This process has been inferred as an efficient mechanism to preferentially transport precious metals with a vapor phase from deeper to shallower levels, where they get precipitated by the second phase separation event (Hedenquist et al. 2000, Heinrich et al 2004).

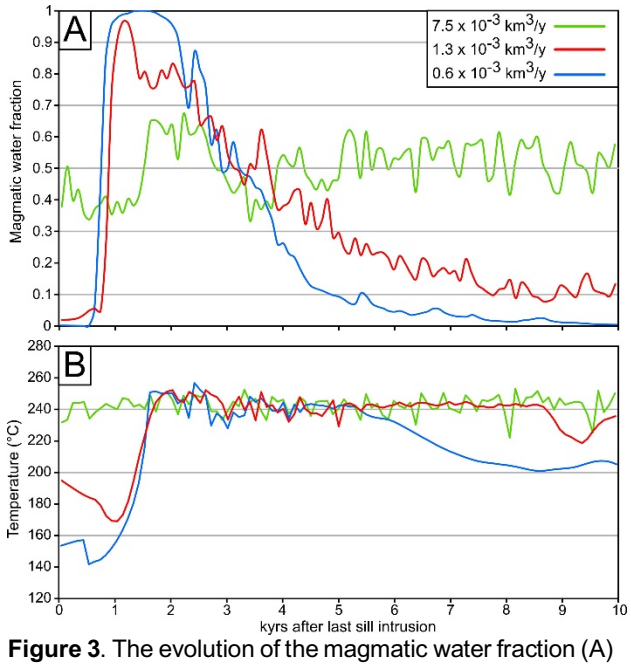

Figure 3. The evolution of the magmatic water fraction (A) and the temperature (B) in the center and 400 m below the surface of the simulation setup within 10000 years after the last sill intrusion.

The modelled ore-forming time span of several thousands of years is in line with recent fluid flow studies (Moncada et al., 2019). Our simulations suggest that rapid magma reservoir agglomerations hamper the formation of high-sulfidation epithermal ore deposits, while at the same time are more likely to produce high-grade porphyry Cu deposits (Korges et al., 2020). Interestingly, our simplified simulations suggest that events of high-sulfidation mineralization with (almost) pure magmatic fluids are more likely to occur by sill injections into a long-lived geothermal system underlain by magma mush reservoirs, rather than systems with larger magma reservoirs with higher melt contents, which may be more characteristic for volcanic systems.

However, our generic simulations still rely on a large number of simplifications and assumptions, such as prescribed locations for sill injections and focused fluid release. Full reactive transport will be required to quantify the geochemical consequences of the physical hydrology. Future developments of the numerical model will provide more detailed insights into the interplay between porphyry and epithermal ore formation in geothermal and volcanic systems.

Acknowledgment

The authors thankfully acknowledge funding by the German Federal Ministry of Education and Research (BMBF; r4 program) and the German Research Foundation (DFG; DOME program).

References

Hedenquist, J.W., Arribas, A., Gonzalez-Urien, E. (2000): Exploration for epithermal gold deposits. Reviews in Economic Geology 13, 45-77.

Hedenquist, J.W. & Arribas, A. (2022): Exploration Implications of Multiple Formation Environments of Advanced Argillic Minerals. Economic Geolology 117, 3, 609-643.

Heinrich, C.A., Driesner, T., Stefánsson, A., Seward, T.M. (2004): Magmatic vapor contraction and the transport of gold from the porphyry environment to epithermal ore deposits, Geology, 32, 761-764.

Korges, M., Weis, P., Andersen, C. (2020): The role of incremental magma chamber growth on ore formation in porphyry copper systems, Earth and Planetary Science Letters, Vol. 552, 116584.

Korges, M., Weis, P., Andersen, C. (2023): Visualization of the incremental magma growth related to porphyry copper deposits obtained with numerical modeling, GFZ Data Services.

Lamy-Chappuis, B., Heinrich, C.A., Driesner, T., Weis, P. (2020): Mechanisms and pat-terns of magmatic fluid transport in cooling hydrous intrusions. Earth Planet. Sci. Lett. 535, 116111.

Moncada, D., Rimstidt, J.D., Bodnar, R.J (2019): How to form a giant epithermal precious metal deposit: Relationships between fluid flow rate, metal concentration of ore-forming fluids, duration of the ore-forming process, and ore grade and tonnage, Ore Geology Reviews, Volume 113, 103066.

Schöpa, A., Annen, C., Dilles, J.H., Sparks, R.S.J., Blundy, J.D. (2017): Magma emplace-ment rates and porphyry copper deposits: thermal modeling of the Yerington Batholith, Nevada. Econ. Geol.112, 1653–1672.

Weis, P., Driesner, T., Heinrich, C. (2012): Porphyry-copper ore shells form at stable pressure-temperature fronts within dynamic fluid plumes, Science 338, 1613-1616.

Coupling structural evolution and fluid flow in metallogenic and geothermal systems

Patrick Ledru[1], Guoxiang Chi[2], Gaétan Milesi[1], Julien Mercadier[1]
[1]GeoRessouces, CNRS, Université de Lorraine, Labcom CREGU, Vandœuvre-lès-Nancy, France
[2]University of Regina, Canada

Abstract. Understanding the structural framework of metallogenic provinces and identification of transient events during which fluid circulation and trapping of mineralization occur is a major challenge for exploration of mineral systems. Analogies between geothermal systems, orogenic gold and unconformity related deposits reveal the role of permeability enhancement during episodes marked by the coupling of tectonic activity and fluid flow. Thus, in the case of Unconformity-Related Uranium deposits of the Athabasca Basin (Saskatchewan, Canada), a new model can be proposed considering that the interplay between compressional fault reactivation and thermal convection is the main driver of this fluid flow system. Short-lived, deformation-driven fluid flow are recorded by the structural and mineralogical evolution of the reactivated basement-hosted fault system.

1. Introduction

The mineral system concept applied to Unconformity-Related Uranium (URU) deposits of the Athabasca Basin (Ledru 2019, Bruce et al. 2020, Ledru et al. 2023;) highlights the major role of crustal scale structures and of the geodynamic context in the onset and sustainability of the hydrothermal systems driving formation of the main orebodies. Within a structural framework defined by the geometry, kinematics and mechanical properties of the fault systems, the identification of transient pulses during which mineralizing fluids are circulating and trapped is critical for the reassessment and definition of exploration pathfinders and guides (McCuaig and Hronsky 2014).

Analogies between hydrothermal ore deposits formed at overpressured conditions during high fluid flux through fault zones and geothermal systems has been developed by Cox (2016). In the case of Enhanced Geothermal Systems, the overpressure induced by injection of fluids produces a stimulation of the permeability network of the drilled domain accompanied by seismic swarms that give a scanning of the fault system. Recent experiments in the Rhine graben have also demonstrated that following the early stages of stimulation, a geothermal reservoir hosted in the fault network has been revealed and can be considered as a self-organized hydrothermal system (Glass et al. 2021).

In the case of the Unconformity-Related Uranium deposits, recent studies have revealed common features with this configuration in which the coupling between structural evolution and fluid flow is critical to explain the formation of large deposits.

2. The architecture and the structural framework

The tectonic history of deeply rooted structures is critical to understand the natural processes at the origin of metallogenic provinces (McCuaig et al. 2010). These structures are responsible for crustal segmentation and are natural links between deep and shallow processes. They guided in many cases the intrusion of magma extracted from the mantle or generated during crustal melting and have recorded significant retrograde metamorphic evolution and hydrothermal alteration during the late orogenic evolution. By referring to geophysical imagery, Card (2020, Tschirhart et al. 2022) considers that protracted reactivation of deep-seated structures and their subsidiaries was a fundamental control on uranium mineralization in the southwestern Athabasca Basin. Based on the structural analysis and resulting cross sections (Ledru et al. 2023) and on numerical modelling (Poh et al. 2020), a similar interpretation is proposed for the Wollaston-Mudjatik transition zone that concentrates the main large to giant uranium deposits.

At the prospect and camp scale, the structural control for focusing mineralizing fluids and mineralization is well established as ore formation is spatially and temporally focused by the reactivation of the pre-Athabasca fault system (Jefferson et al. 2007). The general concept summarized in IAEA (2018) is that deposits were formed in fault zones and along the unconformity where reduced fluids from the basement and oxidized fluids from the basin were mixed. Structural traps opened during active faulting and were repeatedly brecciated (Hoeve and Quirt 1987; Kyser et al. 2000). In more detail, the alteration haloes considered to be related to the deposits are always developed in the vicinity of a fault system that crosscuts the unconformity. Most of these faults correspond to reactivated-inherited fault zones of the basement and have an associated reverse offset of the unconformity, up to several hundred meters along the Virgin River shear zone and below 100 m in the Wollaston-Mudjatik Transition Zone. These faults are often graphite-rich and cohesive to non-cohesive breccias are the most obvious expression of this reactivation.

At the camp scale, detailed structural and microstructural works reveal the polyphase history of these faults, rooted in the basement and propagating into the basin. Alteration paragenesis display a variety of association with microstructures that are often controlled by local faults and their

morphology (thickness and infilling of core and damage zones) and lithological contrast. The hydrothermal alteration within these deeply rooted faults, prior to the mineralization and presumably related to the pre-Athabasca exhumation, seems to have an efficient control on the further channeling of the mineralizing fluid, having deeply modified the original properties of the host rocks. Micro-brecciation and brittle fracturing associated with the polyphase history show how the permeability of these zones has been enhanced (Benedicto et al. 2021).

3. The transient effect

Recent findings and the comparison with their modern counterpart exploited as geothermal reservoirs, suggest that the lifetime of such hydrothermal systems might be much shorter and more dynamic than previously assumed (McCuaig and Hronsky. 2014; Cox 2016). Such pulsations could correspond to modifications of the crustal stress regime marked by highly localized deformation and enhancement of the permeability of the geological systems (Manga et al. 2012). Although no geochronological constraints exist on the time required to form the Athabascan deposits, first-order approximation from Raffensperger and Garven (1995) and Dargent et al. (2015) suggest that 0.1–1Myr is a viable estimate for the duration of the mineralizing event that could then correspond to transient events limited in time and space.

Based on regional geochrono-stratigraphic data, it has been proposed that the deposits were formed at depths of < 3 km (Chi et al. 2018). This mineralization depth estimation has important implications for the hydrodynamic regime and the geothermal gradient, both affecting the potential mechanisms of fluid flow related to U mineralization. A shallow burial environment, together with the sandstone-dominated nature of the basin sediments, favors a hydrostatic regime in the basin (Chi et al. 2013), instead of a lithostatic regime as assumed in the conventional model that considers a paleodepth of 5km. A hydrostatic regime facilitates establishment of fluid convection in the basin, which is further enhanced by elevated geothermal gradients as implied by high temperatures at shallow depths (Wang et al., 2021). This regime at the base of the basin in a shallow burial environment suggests that the unconformity surface is unlikely a hydraulic interface between hydrostatic and lithostatic regime; such an interface is likely located at greater depths in the basement. This hypothesis is supported by the study of graphite in basement faults hosting URU deposits (Song et al. 2022), which suggests that the faults may be reactivated due to the fault-valve mechanism ~5 km below the unconformity surface, whereas the upper tip of the faults may attracts fluids both from the basement and basin via the suction pump mechanism. Thus, the formation of the URU deposits may be considered a result of coupled fault-valve and suction pump mechanism.

Dominantly C-O-H(-N) fluid inclusions trapped within ductile-brittle graphitic shear zones have been considered as associated to the retrograde metamorphism during the exhumation of the Trans-Hudson orogen (Martz et al. 2017). However, the temperature of the mineralizing fluids (150-250° C), suggested by the alteration mineral assemblages and fluid inclusion studies (Richard et al. 2016) and the revised paleodepth of the unconformity of <3km implies high geothermal gradient. The possible origin of such high geothermal gradient remains poorly constrained as no intrusion or volcanic activity has been so far identified within the basin. However, large wavelength anomalies related to mantle upwelling may have developed during the Nuna supercontinent breakup (Pehrsson et al. 2016). A bright band of reflectivity at about 8000m depth has been interpreted as a series of sub-horizontal sheet like diabase intrusions related to the Mackenzie igneous event at 1270 Ma (Jefferson et al. 2007) but nothing excludes that they could correspond to an earlier intrusion related to this Nuna breakup. Finally, modelling suggests that deeply rooted fault systems inherited from the pre-Athabasca orogens could operate as conduits to bring fluids and heat towards the upper parts of the crust, in particular during episodes of tectonic reactivation (Poh et al. 2022). In this case, the mineralized zones showing a high geothermal gradient could be “hot spots” situated at the intersection between this fault system and the unconformity. The discovery of carbonatite dykes within the fault system of the Patterson Lake corridor is another observation that supports such coupling between deep-seated and shallow processes (Johnstone et al. 2021).

In this context, possible deeply rooted basement fluids mixed with fluids originated from the basin lead to a major revision of the current model (Rabiei et al. 2021). Investigating gradients downdip in the main reactivated shear zones recorded by mineralogy and fluid inclusions could be one way to test the hypothesis that brittle faults marking a significant offset of the unconformity could be rooted at depth and have a ductile equivalent enabling metamorphic fluids to be generated. Thus, the role of active faulting and shearing processes would be a trigger of the initiation of a self-organized hydrothermal system (Micklethwaite et al. 2010, Hronsky 2011) and the brittle-ductile transition could be considered as a threshold barrier.

Thermo-Hydraulic and Mechanic (THM) modelling evaluates different scenarios under which the fluid flow was controlled by faulting-related deformation and permeability enhancement. Modelling of simplified geometries of several deposits (Li et al. 2018, 2020; Eldursi et al. 2020), shows that basement faults generally promote fluid flow, fluids circulating downwards

from the basin within the basement (ingress flow) or upwards from basement reservoirs towards the basin (egress flow) both generated by either compressional deformation or fluid convection. The actual flow direction for a given basement fault is influenced by a combination of many factors, especially the dip angle and dip direction as well as spacing of neighbouring basement faults (Chi et al. 2013).

Understanding the geodynamic trigger of this reactivation is a major stake. Based on the dispersion of the U/Pb ages of the mineralization, many attempts of correlation with compressional far-field tectonic events have been done (Kyser and Cuney 2015). These correlations are based on geochronological data which are too much spread to be conclusive (Chi et al. 2018). Several structural observations can be advanced to constrain this trigger. Because of the unfavourable dip of these faults in the compressive stress field, their reactivation could only occur when fluid pressure exceeded the lithostatic load (Sibson et al. 1988; Sibson 2020). The presence of significant amount of graphite must also be underlined as a lubricant facilitating faulting and fluid flow that led to uranium mineralization (Song et al. 2022).

4. Discussion

The review of these different parameters highlights several critical elements that are compatible with other mineral systems (McCuaig and Hronsky 2014). A new model can be proposed considering that the interplay between compressional fault reactivation and thermal convection is the main driver of this fluid flow system (Li et al. 2020, Song et al. 2022). Short-lived, deformation-driven fluid flow are recorded by the structural and mineralogical evolution of the reactivated basement-hosted fault system. This tectonically active period may be associated with a far-field tectonic event and separated by long periods of quiescence. However, by analogy with enhanced or natural geothermal systems (Cox 2016), the possibility that these episodes are related to transient tectonic activity caused by fluid over-pressure should be also considered, interplay between compressional fault reactivation and thermal convection being still applicable. Thus, the formation of the giant deposits could happen during times when the prevailing geodynamic conditions impose strong threshold barriers to fluid flow, causing fluid-flux systems to become self-organized (Hronsky 2011). In this scenario, the presence of a basement hosted reservoir is suggested and the fluid expulsion occurred through transient exit pathways, faults acting like valve system (Sibson et al. 1988, Sibson 2020). In this framework, uranium may precipitate in structural traps as jogs and veins within the core and damage zones of the faults during inter seismic periods, graphite and sulphide being potential reducing agents facilitating the precipitation or reach the unconformity and be trapped in the permeable sediments at the base of the basin if a clay or silicified cap is present.

5. Conclusion

Analogies between geothermal and mineral systems are applied to evaluate the processes at the origin of unconformity-related uranium deposits as known in the Athabasca Basin. Thus, the stimulation of inherited permeability networks and the role of structures in a given tectonic context appear as essential conditions in both systems to initiate, develop and sustainably operate high fluid fluxes within heat exchangers and chemicals that will lead to the formation of geothermal deposits or reservoirs. The recently conceptualized analogies between the induced seismicity of experiments in the development of improved geothermal reservoirs and the polyphase injection of hydrothermal fluids in the shear zones (Cox 2016) open new perspectives for the predictive targeting of reactivated and mineralized fossil zones in the deposits by comparison of the coupling between the deformation regimes and the circulation of fluids in the systems stimulated in a natural (deposits) and anthropogenic (improved geothermal) way.

Acknowledgements

The authors acknowledge the support of the French Agence Nationale de la Recherche (ANR), under grant ANR-21-CHIN-0006 (project GeomiIn3D).

References

Benedicto, A., Abdelrazek, M., Ledru, P., Mackay, C. (2021). Structural controls of uranium mineralization in the Athabasca Basin, Saskatchewan, Canada. Geofluids, 2021, Article ID 3853468, https://doi.org/10.1155/2021/3853468.

Bruce, M., Kreuzer, O., Wilde, A., Buckingham, A., Butera, K., Bierlein, F. (2020). Unconformity-Type Uranium Systems: A Comparative Review and Predictive Modelling of Critical Genetic Factors. Minerals, 10, 738.

Card, C. (2020). The Patterson Lake corridor of Saskatchewan, Canada: defining crystalline rocks in a deep-seated structure that hosts a giant, high-grade Proterozoic unconformity uranium system. Geochem. Explor. Environ. Anal., 21, geochem2020-007. https://doi.org/10.1144/geochem2020-007

Chi, G., Bosman, S., Card, C. (2013). Numerical modeling of fluid pressure regime in the Athabasca basin and implications for fluid flow models related to the unconformity-type uranium mineralization. J. Geochem. Explor., 125, 8-19.

Chi, G., Li, Z., Chu, H., Bethune, K.M., Quirt, D., Ledru, P., Normand, C., Card, C., Bosman, S., Davis, W.J., Potter, E.G. (2018). Shallow-burial mineralization system driven by magmatic heat sources at depth: a new perspective on factors controlling unconformity-related uranium deposits associated with Proterozoic basins. Econ. Geol., 113(5), 1209-1217

Chi G., Xu D., Xue C., Li Z. , Ledru P., Deng T. , Wang Y., Song H. (2022). Hydrodynamic Links between Shallow and Deep Mineralization Systems and Implications for Deep Mineral Exploration. Acta Geologica Sinica (English Edition), 96(1): 1–25.

Dargent, M., Truche, L., Dubessy, J., Bessaque, G., Marmier, H. (2015). Reduction kinetics of aqueous U(VI) in acidic chloride brines to uraninite by methane, hydrogen or C-graphite

under hydrothermal conditions: Implications for the genesis of unconformity-re lated uranium ore deposits. Geochim. Cosmochim. Acta, 167, 11-26.

Glaas, C., Patrier, P., Vidal, J., Beaufort, D., Genter, A. (2021). Clay Mineralogy. A Signature of Granitic Geothermal Reservoirs of the Central Upper Rhine Graben. Minerals, 11, 479. https://doi.org/10.3390/min11050479.

Cox, S.F. (2016). Injection-driven swarm seismicity and permeability enhancement: implications for the dynamics of hydrothermal ore systems in high fluid-flux, overpressured faulting regimes - an invited paper. Econ. Geol., 111, 559-587.

Eldursi K., Chi, G., Bethune, K., Li, Z., Ledru, P., Quirt, D. (2020). New insights from 2- and 3-D numerical modelling on fluid flow mechanisms and geological factors responsible for the formation of the world-class Cigar Lake uranium deposit, eastern Athabasca Basin, Canada. Miner. Deposita, https://doi.org/10.1007/s00126-020-00979-5.

Hoeve, J., Quirt, D. (1987) A stationary redox front as a critical factor in the formation of high-grade, unconformity-type uranium ores in the Athabasca Basin, Saskatchewan, Canada. Bull. Mineral., 110, 157-171.

Hronsky, J.M.A. (2011). Self-Organized Critical Systems and Ore Formation: The Key to Spatial Targeting? SEG Newsletter, 84, 14-16.

IAEA (2018). Unconformity-related Uranium Deposits. TECDOC, 1857.

Jefferson CW, Thomas DJ, Gandhi SS, Ramaekers P, Delaney G, Brisbin D, Cutts C, Portella P, Olson RA. (2007) Unconformity-associated uranium deposits of the Athabasca basin, Saskatchewan and Alberta. Geological Association of Canada, Mineral Deposits Division, Special Publication No. 5, pp. 273-305.

Johnstone, D.D., Bethune, K.M., Card, C.D., Tschirhart, V. (2021). Structural evolution and related implications for uranium mineralization in the Patterson Lake corridor, southwestern Athabasca Basin, Saskatchewan, Canada. Geochem. Explor. Environ. Anal., 21, geochem2020-030, https://doi.org/10.1144/geochem2020-030.

Kyser, T.K., Hiatt, E., Renac, C., Durocher, K., Holk, G., Deckart, K. (2000). Diagenetic fluids in Paleo- and Mesoproterozoic sedimentary basins and their implications for long protracted fluid histories. In: Fluids and Basin Evolution, Kyser, T.K. (Ed.), Min. Assoc. Can. Short Course, 28, 225-262.

Kyser, K., Cuney, M. (2015). Basins and uranium deposits. In: Geology and Geochemistry of Uranium and Thorium Deposits. Short course Series, 46, 224-250.

Ledru, P. (2019). The Mineral System concept applied to unconformity-related uranium deposits of the Athabasca Basin (Canada). In: *Proceedings of the 15th SGA Biennial Meeting*, Glasgow, Scotland. 1179-1182.

Ledru P., Benedicto A., Chi G., Khairallah C., Mercadier J., Poh J., Robbins J. (2023). The unconformity-related uranium mineral system of the Athabasca Basin (Canada). Wiley, ISTE, Natural Resources: Applied Basic Research, Chapter 3.

Li, Z., Chi, G., Bethune, K.M, Eldursi, K., Thomas, D., Quirt, D., Ledru, P. (2018). Synchronous egress and ingress fluid flow related to compressional reactivation of basement faults: the Phoenix and Gryphon uranium deposits, SE Athabasca Basin, Saskatchewan, Canada. Miner. Deposita, doi 10.1007/s00126-017-0737-5.

Li, Z., Chi, G., Bethune, K.M, Eldursi, K., Thomas, D., Quirt, D., Ledru, P., Thomas D. (2020). Interplay between thermal convection and compressional fault reactivation in the formation of unconformity-related uranium deposits. Miner. Deposita, doi.org/10.1007/s00126-020-01011-6.

Manga, M., Beresnev, I., Brodsky, E.E., Elkhoury, J.E., Elsworth, D., Ingebritsen, S. E., Mays, D.C., Wang, C.Y. (2012). Changes in permeability caused by transient stresses: Field observations, experiments, and mechanisms. Rev. Geophys., 50, RG2004, doi:10.1029/2011RG000382.

Martz, P., Cathelineau, M., Mercadier, J., Boiron, M.C., Jaguin, J., Tarantola, A., Demacon, M., Gerbeaud, O., Quirt, D., Doney, A., Ledru, P. (2017). C-O-H-N fluids circulations and graphite precipitation in reactivated Hudsonian shear zones during basement uplift of the Wollaston-Mudjatik Transition Zone: Example of the Cigar Lake U deposit. Lithos, 222-245, doi: 10.1016/j.lithos.2017.10.001.

McCuaig, T.C., Hronsky, J.M.A. (2014). The Mineral System Concept: The Key to Exploration Targeting. Soc. Econ. Geol., Special Publication, 18, 153-175.

McCuaig, T.C., Beresford, S., Hronsky, J.M.A. (2010). Translating the mineral systems approach into an effective exploration targeting system. Ore Geol. Rev., 38, 128-138.

Micklethwaite, S., Sheldon, H.A., Baker, T. (2010). Active fault and shear processes and their implications for mineral deposit formation and discovery. J. Struct. Geol., 32, 151-165.

Pehrsson, S.J., Eglington, B.M., Evans, D.A.D., Huston, D., Reddy, S.M. (2016). Metallogeny and its link to orogenic style during the Nuna supercontinent cycle. In: Supercontinent Cycles Through Earth History Li, Z. X., Evans, D.A.D., Murphy, J. B. (eds), Geol. Soc., London, Special Publications, 424, 83-94.

Poh, J., Yamato, P., Duretz, T., Gapais, D., Ledru, P. (2020). Precambrian deformation belts in compressive tectonic regimes: A numerical perspective. Tectonophysics, 777, doi.org/10.1016/j.tecto.2020.228350.

Poh, J., Eldursi K., Ledru, Yamato, P., Chi G., Benedicto A. (2022). Role of Hydrothermal Circulation along and above Inherited Basement Structures Relating to Unconformity-Related Uranium Mineralization. Geofluids Volume 2022, Article ID 9131289, doi.org/10.1155/2022/9131289

Rabiei, M., Chi, G., Potter, E.G., Tschirhart, V., MacKay, C., Frostad, S., McElroy, R., Ashley, R., McEwan, B. (2021). Fluid evolution along the Patterson Lake corridor in the SW Athabasca Basin: constraints from fluid inclusions and implications for unconformity-related uranium mineralization. Geochem. Explor. Environ. Anal., 21, geochem2020-029, //doi.org/10.1144/geochem2020-029.

Raffensperger, J.P., Garven, G. (1995). The formation of unconformity-type uranium ore-deposits. Coupled groundwater-flow and heat transport modeling. Am. J. Sci., 295, 581-636. doi.org/10.2475/ajs.295.5.581.

Richard, A., Cathelineau, M., Boiron, M.-C., Mercadier, J., Banks, D.a., Cuney, M., 2016. Metal-rich fluid inclusions provide new insights into unconformity-related U deposits (Athabasca Basin and basement, Canada). Mineral. Deposita, 51, 249–270.

Sibson, R.H. (2020). Preparation zones for large crustal earthquakes consequent on fault-valve action. Earth Planets Space, 72, 31, doi.org/10.1186/s40623-020-01153-x.

Sibson, R.H., Robert, F., Poulsen, K.H. (1988). High angle reverse faults, fluid pressure cycling, and mesothermal gold-quartz deposits. Geology, 16, 551-555.

Song, H., Chi, G., Wang, K., Li, Z., Bethune, K.M., Potter, E.G., Liu, Y. (2022). Raman spectroscopy as a tool to decipher the role of graphite in uranium mineralization – a case study of the world-class Phoenix uranium deposit in the Athabasca Basin, Canada. Am. Mineral., 107, 2128–2142.

Tschirhart, V., Potter, E. G., Powell, J. W., Roots, E. A., & Craven, J. A. (2022). Deep geological controls on formation of the highest-grade uranium deposits in the world: Magnetotelluric imaging of unconformity-related systems from the Athabasca Basin, Canada. Geophysical Research Letters, 49, e2022GL098208. https://doi.org/10.1029/2022GL098208

Wang, K., Chi, G., Bethune, K.M., Li, Z., Blamey, N., Card, C., Potter, E.G., Liu, Y. (2018). Fluid P-T-X characteristics and evidence for boiling in the formation of the Phoenix uranium deposit (Athabasca Basin, Canada): implications for unconformity-related uranium mineralization mechanisms. Ore Geol. Rev., 101, 122-142.

Trace element variations and sulphur isotopic ratios of enargite and alunite from the quartz-pyrite-gold orebodies, Mankayan District, Philippines

Pearlyn Manalo[1], Ryota Mine[1], Ryohei Takahashi[1], Akira Imai[2], Andrea Agangi[1], Glenn Alburo[3], Leo Subang[3], Rhyza Ruth Parcon-Calamohoy[3], Mervin de los Santos[3]
[1]Graduate School of International Resource Sciences, Akita University, Japan
[2]Department of Earth Resource Engineering, Kyushu University, Japan
[3]Lepanto Consolidated Mining Company, Inc., Philippines

Abstract. The quartz-pyrite-gold orebodies in the Mankayan District, Philippines is a high-sulfidation epithermal gold deposit that are hosted by Cretaceous metavolcanic basement rocks and Pliocene to Pleistocene dacitic porphyry and pyroclastics (Garcia 1991). This study focuses on two of the several quartz-pyrite-gold orebodies, namely the 1) Northwest orebody and 2) Florence East orebody. We investigate the variation of mineral chemistry of alunite and enargite, which are the dominant gangue and ore minerals, respectively. Compositional maps of alunite from the Northwest orebody show variation of K and Na contents within a single grain and across multiple grains. The element distribution of alunite crystals is either irregular or follows the crystal growth pattern. Meanwhile, the composition of alunite from the Florence East orebody is mostly homogeneous. Enargite shows variable degrees of As being locally substituted by Sb and Te through apparent oscillatory zones. Sulphur isotopic compositions of alunite range from -3.4 to +24.2 ‰, with the values from the Northwest orebody generally higher than those of the Florence East orebody. Meanwhile, the sulphur isotopic compositions of enargite in both orebodies are similar, ranging from -6.2 to -2.3 ‰. The trace element compositions and sulphur isotopic ratios of ore and gangue minerals reflect the varying conditions of the mineralizing environment.

1 Introduction

Alunite and enargite are the main gangue and ore minerals in high-sulfidation epithermal systems (Arribas, 1995; Deyell 2001). Previous studies proposed that the variation of alunite mineral chemistry reflects variations of several factors, such as temperature and composition of hydrothermal fluid (e.g. Deyell 2001). Relatively fewer studies have dwelled on the trace element composition of enargite (Deyell et al. 2011; Liu et al. 2019), focusing on different scales of element zoning. The factors that affect the trace element content of enargite are yet to be established.

The sulphur isotopic ratios of alunite have also been shown useful for the determination of the environment of formation (Rye 2005). Much less is known about the sulphur isotopic behaviour of enargite, as compared to the other ore minerals such as pyrite, galena, and sphalerite. The fractionation factor of enargite and H_2S is only assumed to be like that of sphalerite due to their similar structure (Hedenquist et al. 2017). Contributions of isotopic data from enargite would further increase our understanding of how the values are affected by the environment of formation.

In high-sulfidation deposits, alunite and enargite usually coexist and are sometimes coeval (e.g. Manalo et al. 2018; 2020). The mineral chemistry of one mineral may affect the mineral chemistry of the other. Furthermore, the variations in the sulphur isotopic compositions of the two minerals have implications for the evolution of the bulk hydrothermal fluids. Understanding the variations in the mineral chemistry and isotopic compositions of coexisting ore and gangue minerals may lead to better understanding of the mineralizing system, in general. Thus, this study presents the preliminary results of a side-by-side comparison of the mineralogical and isotopic characteristics of alunite and enargite, in an attempt to see how fluid fluctuations are documented by the gangue and ore.

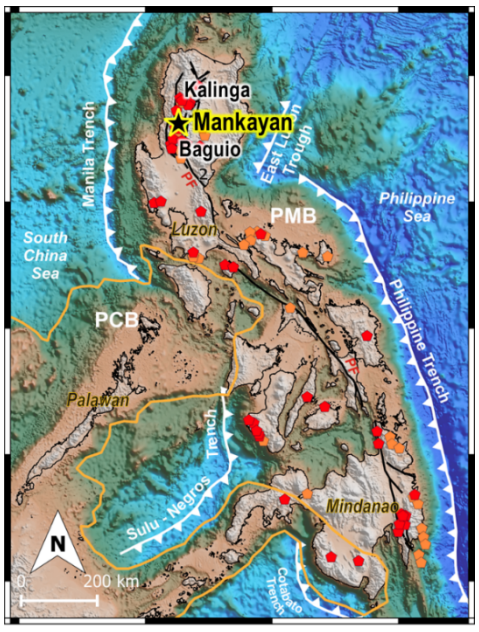

Figure 1. The Mankayan District is located in Luzon Island, Philippines. The area is affected by different tectonic elements, such as the subduction zone along the Manila Trench and the Philippine Fault Zone (Tsutsumi and Perez 2013). Several porphyry copper (red polygons) and epithermal gold (orange polygons) deposits are known throughout the archipelago (Jimenez 2002). Topography and bathymetry data is from Amante and Eakins (2011).

2 Geological Background

The Mankayan District is located within the Central Cordillera in western Luzon, Philippines (Figure 1). The oldest rocks in the district are the Cretaceous to Eocene Lepanto Metavolcanics (Figure 2; Garcia, 1991). These are unconformably overlain by volcaniclastic sequences of the Balili Formation and Apaoan Formation. Periods of magmatism in the district are recorded by the Middle Miocene Bagon Intrusives and the Plio-Pleistocene Imbanguila and Bato dacitic rocks, which occur as porphyry domes and pyroclastic deposits.

There are four types of mineralization in the Mankayan District. These comprise porphyry Cu-Au orebodies, carbonate Au-Ag-base metal veins, enargite-Au orebodies, and the quartz-pyrite-gold orebodies. The ages of the different types of deposits vary. The oldest reported age is 3.5 Ma of the Guinaoang porphyry deposit (Sillitoe and Angeles 1985), while the youngest age is 1.45 Ma of the Far Southeast porphyry deposit (Arribas et al. 1995). The ages of alunite related to the different high-sulfidation orebodies also vary. Arribas et al. (1995) reported K-Ar ages of alunite from the Lepanto Main enargite orebody ranging from 1.56 Ma to 1.17 Ma. Ar-Ar ages on alunite from the quartz-pyrite-gold veins in Northwest and Florence range from 3.0 Ma to 1.9 Ma (Manalo et al. 2018; 2020; Mine 2022).

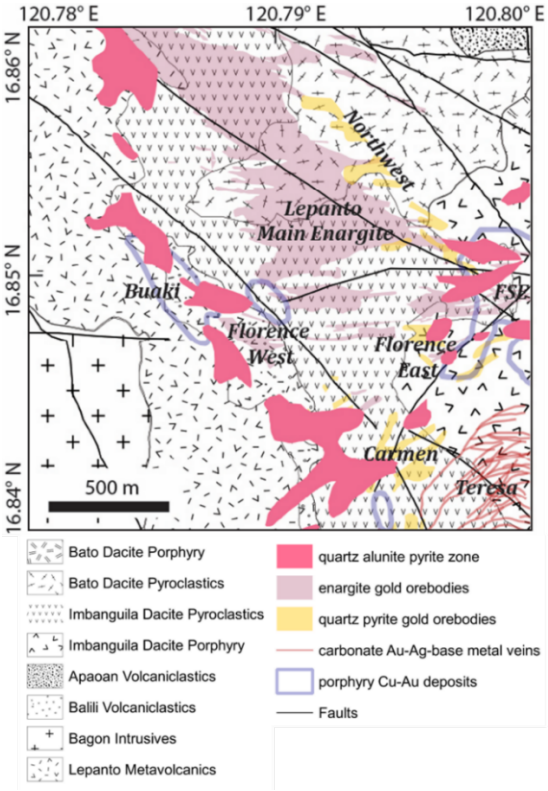

Figure 2. Location of the Northwest and Florence East Quartz-Pyrite-Gold orebodies in Lepanto, Mankayan, Philippines. The mineralization is mainly hosted by the Lepanto Metavolcanics and the Imbanguila Dacite Porphyry and Imbanguila Dacite Pyroclastics (modified from Garcia 1991).

3 Methods

Polished sections of rock samples collected from drill cores and underground tunnels of the Northwest and Florence orebodies were prepared, Descriptions of the samples have mostly been reported by Manalo et al. (2018, 2020). A Nikon Eclipse LV100N POL polarizing microscope was used for transmitted and reflected light petrography.

The chemical composition of alunite was analysed using a JEOL JXA-8230 electron probe microanalyzer in wavelength-dispersive mode. Potassium, Fe, Al, Na, P, Ba, S, Pb and Ca were analysed using a 15 kV acceleration voltage, 10 nA beam current and 15 µm beam diameter, as suggested by Deyell 2001). The same instrument was used for the analysis of concentrations of As, Se, Fe, S, Sb, Te, Bi, Pb, Ag, Cu, Zn, Co, Ni, Au and Sn in enargite crystals. The measuring conditions are 20 kV acceleration voltage, 20 nA beam current and 5 µm beam diameter. For alunite and enargite, standard specimens include the compounds $KAlSi_3O_8$, $NaAlSi_2O_6$, Al_2O_3, $BaSO_4$, $Ca_5(PO_4)$, FeS_2, SnSe, GaAs, Sb_2S_3, Bi_2S_3, PbS, ZnS, and pure metals, Ag, Cu, Co, Ni, Au, and Te.

Crystals of alunite and enargite were carefully separated by handpicking using a binocular microscope. About 20 mg of enargite was decomposed using 20mL 16N HNO_3 and 2mL liquid Br_2 at 90 °C. The residue after overnight evaporation was redissolved using 10mL 6N HCl and was subsequently diluted to 100 mL using distilled water. The solution was then filtered to remove the undissolved residue. The filtered solution was passed through a cation exchange column. Ten millilitres of 10% $BaCl_2$ was added to the 300 mL eluent to precipitate $BaSO_4$ crystals.

About 250 mg of alunite was dissolved using 0.5 M NaOH solution at 80 °C overnight. Undissolved materials were filtered. The solution passed through a cation-exchange column. The eluent was acidified using 10mL 6N HCl and 10 mL of 10 % $BaCl_2$ solution was added to the solution to precipitate the $BaSO_4$ crystals.

The $BaSO_4$ precipitate was collected using a membrane filter and 50 mL syringe. After the precipitate dried, 0.4 to 0.5 mg of the $BaSO_4$ precipitate was packed with 2 to 3 mg V_2O_5 in a tin foil. The samples were combusted in a quartz tube at 1020 °C and the resulting SO_2 gas was isolated using a Thermo Fisher Scientific Flash 2000 Elemental Analyzer. The isotopic ratios were measured using Thermo Fisher Scientific Delta V Advantage isotope ratio mass spectrometer. Calibration curves were constructed using IAEA NBS-127, IAEA SO-5 and IAEA SO-6 standards. The sulphur isotopic ratios are presented relative to the sulphur isotopic ratio of the troilite of the Canon Diablo meteorite in per mil. The analytical uncertainty is ±0.2 ‰.

4 Results

4.1 Sample description

The Northwest and Florence East orebodies display differences in the occurrence of enargite and alunite. In the Northwest orebody, alunite and enargite occur in distinct paragenetic sequences. Most of the alunite in the Northwest orebody is closely associated with abundant coarse-grained pyrite (Figure 3A), while enargite is more closely associated with quartz. The alunite deposited in an earlier stage than that of the enargite ore (Manalo et al. 2018). In contrast, enargite and alunite in the Florence East orebody are closely associated, and likely belong to the same stage (Figure 3B; Manalo et al. 2020).

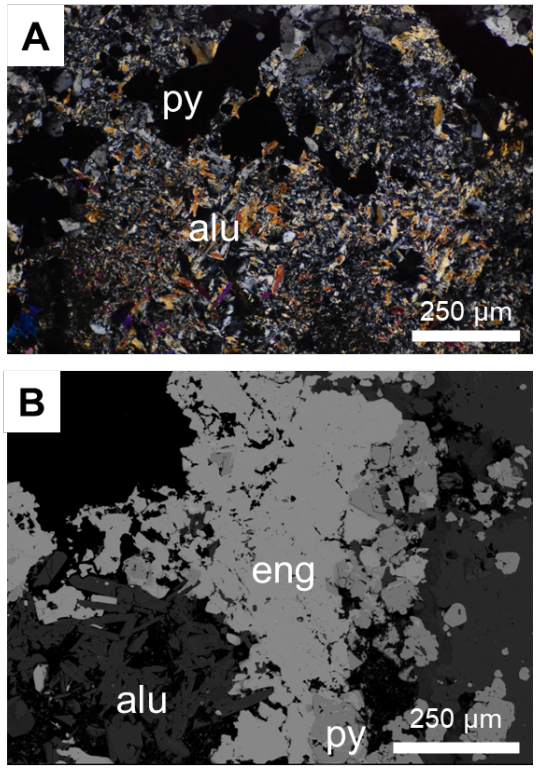

Figure 3. A A photomicrograph of a sample from the Northwest orebody showing alunite (alu) and pyrite (py) association. **B** A backscattered electron image of enargite (eng) coexisting with alunite in the Florence East orebody.

4.2 Mineral chemistry of alunite

In the Northwest orebody, coarse-grained tabular alunite commonly shows variation in K and Na contents, while Al and S contents are mostly uniform within a single grain and across multiple grains (Figure 4). There are apparent systematic variations in the concentrations of K and Na, which follow the crystal structure. Wide variations in the amount of Na substitution were observed in the samples from the Northwest orebody. However, some samples display irregular zonation. In the Florence East orebody, we observed relatively homogenous K-rich alunite.

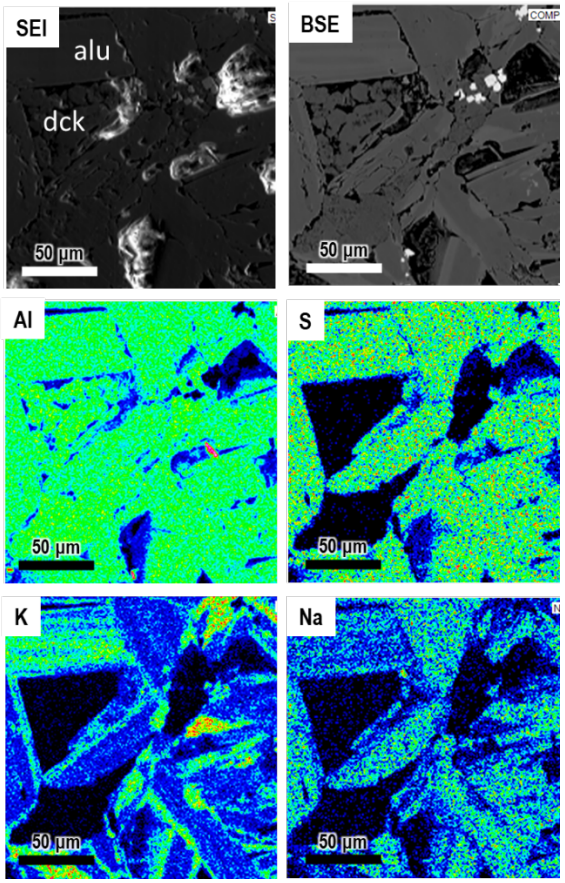

Figure 4. Elemental distribution maps of alunite from the Northwest orebody (alu – alunite; dck – dickite).

4.3 Mineral chemistry of enargite

The crystal habit of enargite in the Northwest and Florence East orebodies varies from being subhedral to anhedral. Luzonite commonly occurs with enargite. Antimony is the most abundant trace element in enargite, followed by Fe and Te. The average Sb content is 5000 ppm, with some values reaching 2 wt%. Tellurium concentration averages at 630 ppm, with several anomalous points reaching up to ~6000 ppm. The average concentration of Fe in enargite is 1840 ppm, with anomalous values reaching up to 1 wt%.

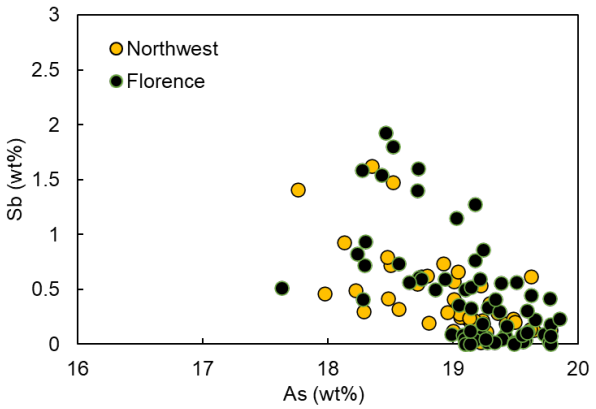

Figure 5. Bivariate plot comparing the As and Sb contents of enargite in the Northwest and Florence East orebodies.

Figure 6 shows oscillatory variations in Sb and Te contents of enargite that is limited only to a certain part of crystal. It also shows Fe enrichment in other parts of the enargite crystal.

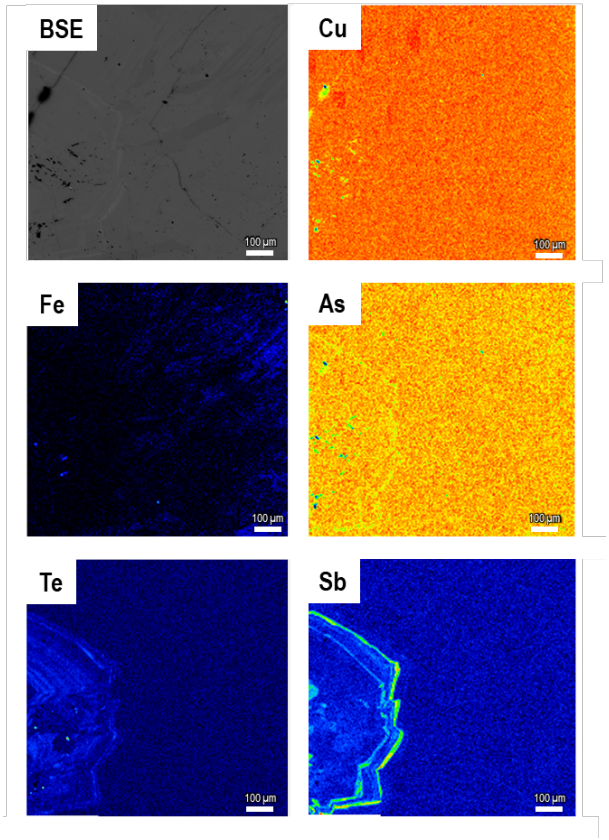

Figure 6. Elemental distribution maps of enargite from the Northwest orebody.

The concentration of Au in enargite is 250 ppm on average and 600 ppm maximum. Silver concentration varies from below the limit of detection (< 35 ppm) to 200 ppm. The concentration of Pb and Se were below the limits of detection in all the points analysed.

4.4 Sulphur isotopes

The sulphur isotope ratios of alunite show two distinct ranges. One group range from -3.4 ‰ to -1.7 ‰, while the other range is from +9.9 ‰ +24.2 ‰. The sulphur isotope ratios of enargite range from -6.2 ‰ to -2.3 ‰ (Manalo et al. 2018; Mine 2022).

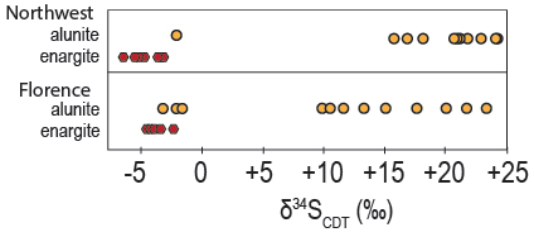

Figure 7. Variations of sulphur isotopic ratios of alunite and enargite in the Northwest and Florence East orebodies. Data of the Northwest orebody were from Manalo et al. (2018), while those of the Florence orebody were from Manalo et al. (2020) and Mine (2022).

Figure 7 shows that the sulphur isotopic ratios of alunite from the Florence orebody have wider range than those of the Northwest orebody. On the other hand, the sulphur isotopic ratios of enargite from both orebodies overlap within a narrow range. Two samples of alunite from both orebodies have similar sulphur isotopic ratios to those of enargite, which may indicate that some alunite was formed in a supergene environment. Most of the alunite samples, however, have sulphur isotopic ratios that are within the typical range of magmatic-hydrothermal alunite and magmatic-steam alunite (Rye 2005).

Acknowledgements

We are grateful to Mr. Bryan Yap of the Lepanto Consolidated Mining Co., for permission to do research on the quartz-pyrite-gold veins. This research is funded by the Japan Society for the Promotion of Science (JSPS) Grant-in-Aid for Scientific Research 21K04960, 21KK0089 and 22K14633. Funding was also provided by the 2022 Dowa Holdings Inc., Young Researcher Grant.

References

Amante, C., Eakins, B.W. (2009): ETOPO1 Arc-Minute Global Relief Model: Procedures, Data Sources and Analysis. NOAA Technical Memorandum NESDIS NGDC-24.

Arribas, Jr., A., Hedenquist, J.W., Itaya, T., Okada, T., Concepcion, R.A., and Garcia, Jr., J.S. (1995): Contemporaneous formation of adjacent porphyry and epithermal Cu-Au deposits over 300 ka in northern Luzon, Philippines, Geology, v. 23, p. 337–340.

Deyell, C.L. (2001): Alunite and High Sulfidation Gold-Silver-Copper Mineralization in the El Indio-Pascua Belt, Chile-Argentina. PhD Dissertation. University of British Columbia, Vancouver, Canada.

Garcia, Jr., J.S. (1991): Geology and mineralization characteristics of the Mankayan mineral district, Benguet, Philippines: Geological Survey of Japan, Report 277, p. 21–30.

Manalo, P.C., Imai, A., Subang, L., de los Santos, M., Yanagi, K., Takahashi, R., Blamey, R. (2018): Mineralization of the northwest quartz-pyrite-gold veins: Implications for multiple mineralization events at Lepanto, Mankayan Mineral District, northern Luzon, Philippines, Economic Geology, v. 113, p. 1609-1626.

Manalo, P.C., Subang, L.L., Imai, A., de los Santos, M.C., Takahashi, R., Blamey, N.J.F. (2020): Geochemistry and fluid inclusions analysis of vein quartz in the multiple hydrothermal systems of the Mankayan Mineral District, Philippines, Resource Geology, v. 70, p. 1-27.

Mine, R., Manalo, P., Takahashi, R., Agangi, A., Sato, H., Imai, A., Parcon-Calamohoy, R., Subang, L., de los Santos, M., Alburo, G. (2022): Characteristics of the Florence orebody, Lepanto Mine, Mankayan District, Philippines [abs], The 71st Annual Meeting of the Society of Resource Geology, June 29 - July 1, Tokyo, Japan

Rye, R.O., 2005, A review of the stable-isotope geochemistry of sulfate minerals in selected igneous environments and related hydrothermal systems: Chemical Geology, v. 215, p. 5–36.

Sillitoe, R.H., Angeles, Jr., C.A., 1985, Geological characteristics and evolution of a gold rich porphyry copper deposit at Guinaoang, Luzon, Philippines [abs.]: Institute of Mining and Metallurgy, Asian Mining, London, 1985, Abstract Volume, p. 15–26.

In-situ trace element analyses of pyrite from the Pefka epithermal Cu-Au-Te-In-Se deposit, Rhodope, Northern Greece

Margarita Melfou[1], Panagiotis Voudouris[2], Reiner Klemd[3], Manuel Keith[3], Vasilios Melfos[1], Lambrini Papadopoulou[1], Nikolaos Kantiranis[1]
[1] Faculty of Geology, Aristotle University of Thessaloniki, Greece
[2] Faculty of Geology and Geoenvironment, National and Kapodistrian University of Athens, Greece
[3] GeoZentrum Nordbayern of Friedrich-Alexander-Universität (FAU) Erlangen-Nürnberg, Germany

Abstract The Pefka epithermal deposit is a high- to intermediate-sulfidation Cu-Au-Te-In-Se deposit located in the Rhodope metallogenic province of northern Greece, displaying complex ore mineralogy. Pyrite is ubiquitous in the different mineral assemblages. Pyrite grains are identified to be associated with early galena (py_{ga}), tennantite-(Cu) ($py_{tnt\text{-}(Cu)}$), colusite (py_{col}), native-Au (py_{Au}) and late tellurides (py_{tel}). The crystal habit of the pyrite varies from euhedral to anhedral, and backscattered electron (BSE) imaging reveals at least two types of pyrite in the $py_{tnt\text{-}(Cu)}$ association. Preliminary EPMA and LA-ICP-MS data allow the quantification of the critical and rare metal concentrations. The results show that the pyrite grains are particularly enriched in In, Se, Ag, Te, Hg and Bi. The Au and Te versus As concentrations in the pyrite are used to define some of the physicochemical conditions related to the deposition of these metals through the evolution of the system.

1 Introduction

The demand for critical, rare and base metals will increase in the following years as a result of the global energy transition towards low-carbon technologies (Grandell et al. 2016). Research in the enrichment processes of base, rare and critical metals is of high importance. Rhodope is a highly prosperous district in northern Greece for future research, exploration and exploitation of critical and rare metals associated with hydrothermal deposits. The Pefka deposit is a high- (HS) to intermediate-(IS) sulfidation epithermal deposit enriched in Cu-Au-Te-In-Se (Voudouris et al. 2022). Previous studies have identified the mineralogy and the main ore stages of the complex mineralization (Dimou et al. 1994; Repstock et al. 2015; Voudouris et al. 2022). However, the physicochemical conditions of each stage and the critical and rare metal distribution in the different sulfides and sulfosalts have not been studied in detail. This contribution aims to provide new preliminary data on the critical- and rare-metal enrichment of pyrite in the Pefka HS-IS epithermal mineralization and to constrain a part of the metallogenic evolution (HS and IS stages) of the mineralization based on these data.

2 Geological context

A highly prosperous district for epithermal mineralization hosted in Oligocene-Miocene volcanic rocks, is the Rhodope metallogenic province in Greece (Fig. 1a), located in the broader Western Tethyan metallogenic belt (Melfos and Voudouris 2017; Voudouris et al. 2019). Rhodope is characterized by metamorphic core complexes exhumed during Late Cretaceous and Tertiary, by supra-detachment sedimentary basins, and by mafic to felsic magmatism of Late Eocene to Early Miocene age (Marchev et al. 2005; Voudouris et al. 2022). Intense hydrothermal alteration is associated with the magmatic rocks and thus the occurrence of numerous porphyry Cu-Mo-Au-Re and HS to IS epithermal mineralization is widespread (Voudouris et al. 2019, 2022).

The Pefka deposit belongs to the Pefka-Loutros area, part of the Rhodope, which hosts numerous HS and IS epithermal mineralization in hydrothermally altered volcanic rocks. Numerous precious and base-metal unexplored mineralizations occur in the area exhibiting complex alteration and mineral zonation patterns. The southern and western part of the Pefka-Loutros area exhibits silicic and advanced argillic altered outcrops associated with E-trending faults, which are rimmed outwards and downwards by sericitic and argillic alteration (Fig. 1b) (Voudouris et al. 2022).

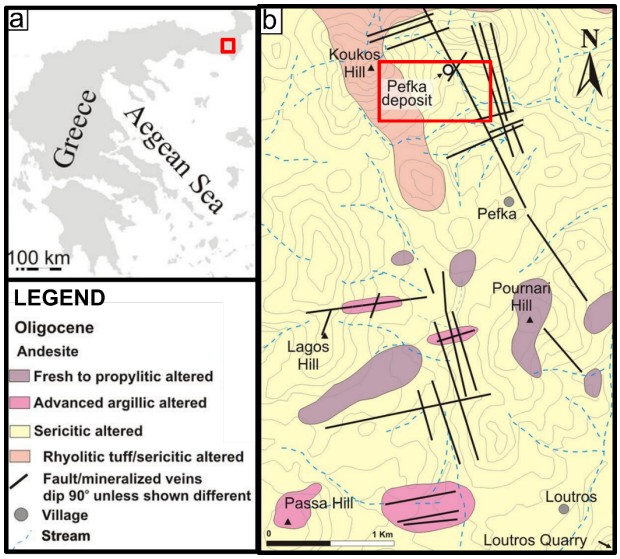

Figure 1. (a) Geological map of Greece. (b) Alteration map of the Pefka-Loutros area. Modified after Voudouris et al. (2022). The Pefka deposit is highlighted with the red rectangle in both images.

The Pefka deposit is hosted by altered andesites that are mainly related to intermediate argillic and sericitic to argillic alteration (Fig. 1b) (Voudouris 2006; Voudouris et al. 2022). It is

enriched in base, rare and critical metals (Cu, Fe, Au, Ag, Pb, Zn, Bi, Sn, Ge, Ga, In, Mo, V, As, Hg, Te and Se) displaying exceptional and rare ore mineralogy including numerous sulfides, sulfosalts, tellurides and native metals (Melfos and Voudouris 2012; Repstock et al. 2015; Voudouris et al. 2019, 2022). The deposit is characterized by at least three distinct mineralization styles. An early massive Se-rich galena vein has been identified crosscutting the altered host rocks. This early stage is followed by an NNW-trending HS vein system composed of quartz, enargite/luzonite, goldfieldite, watanabeite, colusite, chalcopyrite, roquesite, tennantite-(Cu), and native gold (Repstock et al. 2015; Voudouris et al. 2022). In this HS stage, tennantite develops at the rims of the early galena grains and is extremely rich in In, up to 6.5 wt%, which is the highest concentration ever reported (Voudouris et al. 2022). Tennantite-(Cu) is part of the HS assemblage and also characterizes the transition from the HS stage to the IS stage (Voudouris et al. 2022). The late ore stage is characterized by a NE-trending, IS vein system that is composed primarily of carbonates, tellurides and tetrahedrite-(Zn) (Repstock et al. 2015; Voudouris et al. 2022).

3 Methods

Five representative samples of pyrite spatially associated with galena (py_{ga}), tennantite-(Cu) ($py_{tnt-(Cu)}$), colusite (py_{col}), native-Au (py_{Au}) and tellurides (py_{tel}) from the Pefka mineralization were collected from surface outcrops at the Pefka mine. Mineral identification and detailed imaging were conducted with scanning electron microscope - energy dispersive X-ray spectroscopy (SEM-EDS) and backscattered electrons (BSE), respectively, at the Faculty of Geology of the Aristotle University of Thessaloniki (AUTh). Further analyses for the major and trace elements in the pyrite grains of the Pefka mineralization were conducted with an electron probe micro-analyzer (EPMA) and laser ablation inductively coupled plasma mass spectrometry (LA-ICP-MS) at the GeoZentrum Nordbayern of Friedrich-Alexander-Universität (FAU) Erlangen-Nürnberg. The S content of the pyrite grains from the EPMA analyses was used as the internal standard for the quantification of the LA-ICP-MS data, with Glitter 4.4.4 software (Achterberg et al. 2001). The beam diameter was varied from 20 to 35 µm depending on the homogeneity and size of the targeted pyrite grains.

4 Results

4.1 Petrography of pyrite

Macroscopically, pyrite is associated with the galena (py_{ga}) (Fig. 2a), the quartz ($py_{tnt-(Cu)}$, py_{col}, py_{Au}) (Fig. 2b-c), and the carbonate (py_{tel}) (Fig. 2d) veins. It occurs as semi-massive veins or disseminations in quartz veins where it is surrounded by sulfosalts (Fig. 2b) or is spatially related to barite grains (Fig. 2c). It also occurs in disseminations at the carbonate veins (Fig. 2d) and is associated with chalcopyrite.

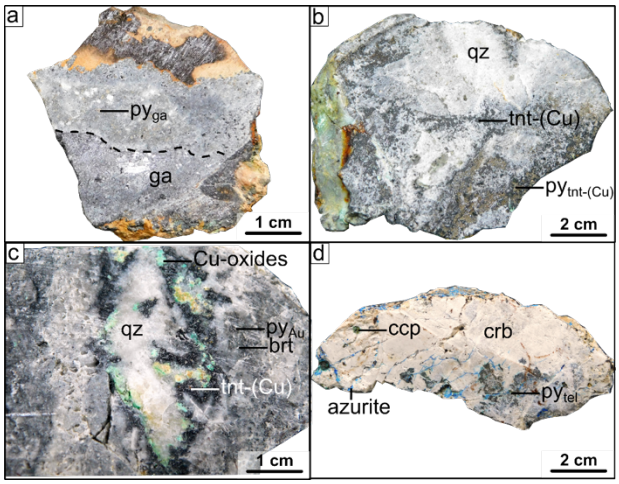

Figure 2. Images from the ore-related samples of Pefka mineralization with a focus on the relationships between alteration/ore mineralization and pyrite. (a) Galena vein in contact with altered rock with disseminated pyrite (py_{ga}). The dashed black line represents the border of the massive galena. (b) Massive quartz vein with pyrite ($py_{tnt-(Cu)}$) grains that are surrounded by tennantite-(Cu). (c) Quartz vein with tennantite-(Cu) and Cu-oxides. Pyrite (py_{Au}) occurs in disseminations in the quartz matrix closely associated with barite. (d) Carbonate vein with pyrite (py_{tel}), chalcopyrite and azurite. Mineral abbreviations after Whitney and Evans (2010) and Au: native Au, tnt-(Cu): tennantite-(Cu), tel: tellurides.

Based on microscopy observations, pyrite occurs as euhedral or anhedral grains. Py_{ga} in spatial association with the early galena is usually euhedral and contains inclusions of rutile (Fig. 3a). Tennantite-tetrahedrite with small chalcopyrite inclusions is found as mineral inclusions near the rims of the pyrite grains (Fig. 3a).

In samples from the NNW-trending HS vein system (Fig. 3b-d), $py_{tnt-(Cu)}$ is subhedral to anhedral and usually surrounded by massive or semi-massive tennantite-(Cu), (Fig. 3b-d) or supergene iron oxides (Fig. 3b-c). Py_{Au} grains are in proximity to native Au that is associated with tennantite-(Cu) usually near elongated barite grains (Fig. 3e). Late py_{tel} is euhedral and is related to chalcopyrite and Zn-tetrahedrite (Fig. 3f). It usually hosts various mineral inclusions of the tetrahedrite-(Zn) and tellurides, e.g. coloradoite (HgTe). Back-scattered images show a slight zonation of the $py_{tnt-(Cu)}$ grains (Fig. 3a and d).

4.2 Trace element abundances in pyrite (EPMA and LA-ICP-MS)

Pyrite varies from As-poor (below detection limit) to As-rich (up to 1.5%) (Fig. 4a). Critical and rare metals are enriched in the pyrite grains, with up to 103 ppm In (Fig. 4b), up to 751 ppm Se (Fig. 4c), up to 1949 ppm Ag (Fig. 4d), up to 4977 ppm Te, up to 1110 ppm Hg and up to 760 ppm Bi. The measured

very high Se, Te, and Hg content of pyrite is possibly a result of the incorporation of mineral inclusions in the analytical volume. The presence of other metals has been also identified, with up to 61 ppm V, 4146 ppm Mn, 220 ppm Co, 161 ppm Ni, 3.5% Cu, 196 ppm Zn, 40 ppm Ga, 37 ppm Ge, 47 ppm Mo, 50 ppm Cd, 10 ppm Sn, 0.1% Sb, 4 ppm Au, 529 ppm Tl, and 5% Pb.

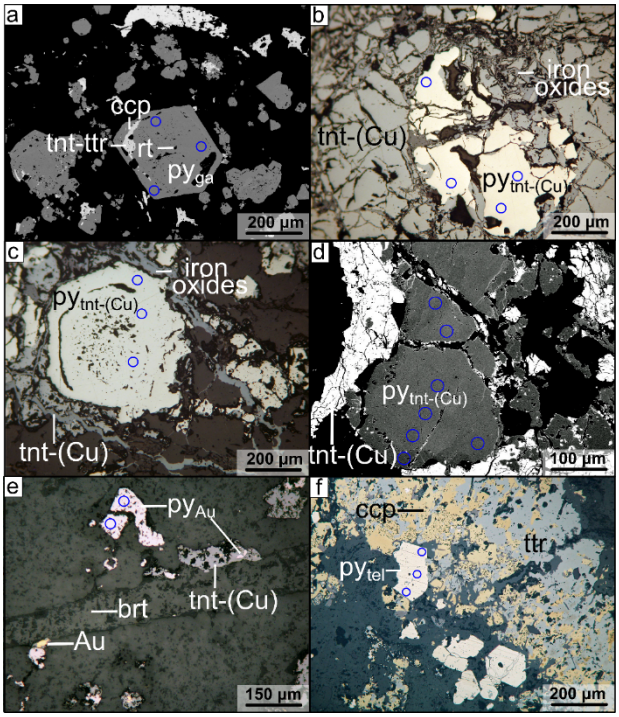

Figure 3. Microphotographs of sulfides-sulfosalts from the Pefka deposit with a focus on pyrite grains and their relationship to the other minerals, under reflected light (b, c, e and f) and on BSE images (a and d). The blue circles represent the LA-ICP-MS spots. (a) Euhedral py_{ga} grain spatially associated with the galena assemblage that encloses rutile and tennantite-tetrahedrite with small chalcopyrite grains. (b) $Py_{tnt-(Cu)}$ surrounded by tennantite-(Cu). (c) Subhedral $py_{tnt-(Cu)}$ with porous core and clear rim. (d) $Py_{tnt-(Cu)}$ with a brighter core and darker rim on the BSE image and in association with tennantite-(Cu). (e) Py_{Au} in the proximity of a barite grain that is in contact with tennantite-(Cu) and native Au grains. (f) Subhedral py_{tel} in association with chalcopyrite and tetrahedrite. Mineral abbreviations after Whitney and Evans (2010) and Au: native Au, tnt-(Cu): tennantite-(Cu), tel: tellurides.

5 Discussion

5.1 Pyrite occurrence in the different ore stages

Py_{ga} is present as euhedral crystals in an altered volcanic rock in proximity to the early massive galena vein. However, it is not clear if it is contemporaneous and genetically related to the galena as intergrowths or crosscutting relationships have not been observed. Therefore, we chose to distinguish this sample and call it py_{ga}, as it shows different chemistry from the rest of the samples (Fig. 4), but its relation to galena remains controversial. The appearance of $py_{tnt-(Cu)}$, py_{col}, py_{Au} in the HS stage varies from subhedral to anhedral. The BSE imaging reveals that the dark rim of the $py_{tnt-(Cu)}$ in Fig. 3d, hosts inclusions of tennantite-(Cu). This suggests that there are at least two types of pyrite in the HS stage. The first was probably pre-existing and the second was contemporaneous with the deposition of the sulfosalts. Py_{Au} of the HS stage is also interpreted to accompany the native Au deposition, as it is found as mineral inclusions in the sulfosalts that host the Au (Fig. 3e). Py_{tel} occurs at the late IS telluride-related stage accompanying the carbonates and the tetrahedrite-chalcopyrite assemblage. In this stage, py_{tel} is usually subhedral (Fig. 3f).

Therefore, combining these observations with the paragenetic sequence of Voudouris et al. (2022), the early IS galena is probably temporally related to the py_{ga}, the HS assemblage is accompanied by the $py_{tnt-(Cu)}$, the py_{Au} and the py_{col}, and the subsequent IS assemblage is accompanied by the py_{tel}.

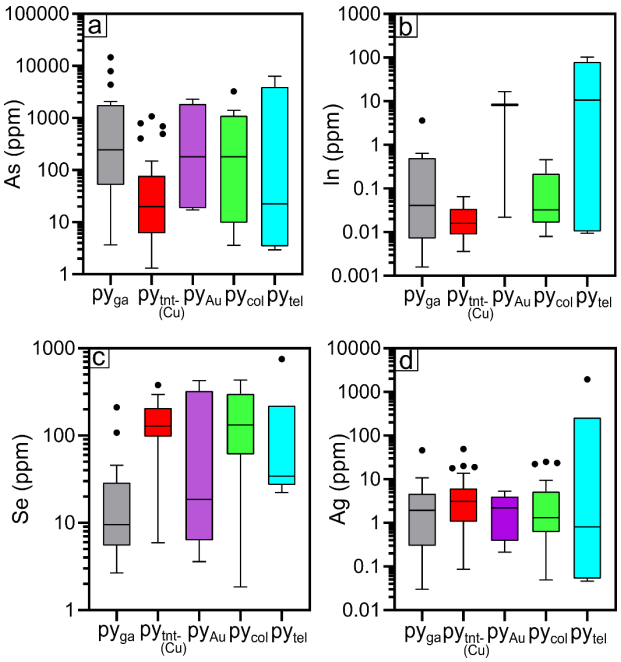

Figure 4. Tukey boxplots of As (a), In (b), Se (c) and Ag (d) variations of pyrite grains from the Pefka deposit for the different samples. Points represent outliers of the main cluster of the data and the horizontal line of each boxplot represents the median of the data. Mineral abbreviations after Whitney and Evans (2010) and Au: native Au, col: colusite, tnt-(Cu): tennantite-(Cu), and tel: tellurides.

5.2 Metallogenic implications through pyrite chemistry

Deditius et al. (2014) demonstrated that there is an increase in As and Au concentration in pyrite during the transition from the porphyry to the epithermal environment and showed that arsenian pyrite preserves the Au/As ratio of the parental fluids and thus can be used as a monitor for hydrothermal fluid evolution.

The results of Au and As concentration in pyrite from the Pefka deposit (Fig. 5a) from the different samples show that the Au/As ratio increases from the py_{ga} to the $py_{tnt-(Cu)}$, py_{col} and py_{Au} (HS stage)

and then again slightly decreases (but still remaining high) to the final py_{tel} (IS stage) (obvious from the blue dashed arrow of Fig. 5a). This indicates that the deposition of Au in the system mainly occurred during the HS and IS stage, which is consistent with the interpretation of Voudouris et al. (2022), and that the Au/As ratio of the fluids was higher during the HS stage.

The extreme enrichment of Te in Pefka is interpreted by Voudouris et al. (2022) to be related to extensive boiling processes. The increasing content of Te along with As concentration in the system from the HS to IS stage is evident from the increasing content of Te in pyrite from the early stages (py_{ga}, $py_{tnt\text{-}(Cu)}$, py_{Au}, py_{col}) to the IS stage with the deposition of tellurides (Fig. 5b). All the samples display several points that exceeds the solubility line of Te, that suggests that native Te inclusions are present in the pyrite. However, the py_{tel} displays Te as high as 4977 ppm (Fig. 5b), which is explained by the contemporaneous precipitation of tellurides of the IS stage. Keith et al. (2018) suggested that Te-rich pyrite precipitates from reduced fluids. Thus, an evolution from probably oxidized fluids of the HS stage towards reduced fluids of the IS stage may be assumed for the Pefka deposit.

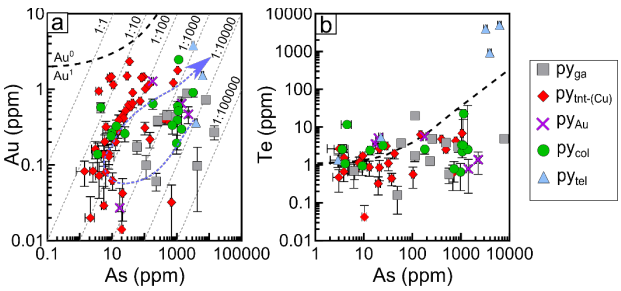

Figure 5. Concentrations and 1-sigma error ranges of Au (a) and Te (b) as a function of As in pyrite from the different samples of the Pefka deposit. The black dashed lines define the solubility limit of Au (a) and Te (b) below which Au and Te, respectively, are present in the structure of pyrite, while above is present as Au^0 and Te^0 inclusions in pyrite (after Reich et al. 2005; Keith et al. 2018). The blue dashed arrow in (a) represents the evolution of the average of the Au/As ratio of each sample compared to the paragenetic sequence. Mineral abbreviations after Whitney and Evans (2010) and Au: native Au, col: colusite, tnt-(Cu): tennantite-(Cu), and tel: tellurides.

6 Conclusions

Pyrite grains from the Pefka deposit are spatially associated with galena (py_{ga}), tennantite-(Cu) ($py_{tnt\text{-}(Cu)}$), colusite (py_{col}), native-Au (py_{Au}) and tellurides (py_{tel}). The pyrite grains are particularly enriched in In, Se, Ag, Te, Hg and Bi. The Au and As concentrations of pyrite from the Pefka deposit suggest that the deposition of Au in the system occurred both in the HS and IS stages. The positive correlation of Te and As contents of the pyrite grains also suggests that at least the final IS assemblage was deposited from reduced fluids.

Acknowledgments

We gratefully acknowledge that part of this project is supported by the Society of the Economic Geologist (SEG) 2022 Student Research Grants (SRG 22-47) through the Hugh McKinstry Fund. Dr. Brätz is thanked for her assistance during the LA-ICP-MS analyses and data processing.

References

Achterberg E, Ryan C, Jackson S, Griffin W (2001) Data reduction software for LA-ICP-MS. Laser Ablation ICP-MS in the Earth Science 29:239–243

Deditius AP, Reich M, Kesler SE, Utsunomiya S, Chryssoulis SL, Walshe J, Ewing RC (2014) The coupled geochemistry of Au and As in pyrite from hydrothermal ore deposits. Geochimica et Cosmochimica Acta 140:644–670. https://doi.org/10.1016/j.gca.2014.05.045

Dimou E, Michael C, Serment R (1994) Mineralogical composition of epithermal polymetallic mineralization at Pefka. Rhodope. In: Bull. Geol. Soc. Greece. 30, 553–1550. pp 553–1550

Grandell L, Lehtilä A, Kivinen M, Koljonen T, Kihlman S, Lauri LS (2016) Role of critical metals in the future markets of clean energy technologies. Renewable Energy 95:53–62. https://doi.org/10.1016/j.renene.2016.03.102

Keith M, Smith DJ, Jenkin GRT, Holwell DA, Dye MD (2018) A review of Te and Se systematics in hydrothermal pyrite from precious metal deposits: Insights into ore-forming processes. Ore Geology Reviews 96:269–282. https://doi.org/10.1016/j.oregeorev.2017.07.023

Marchev P, Kaiser-Rohrmeier M, Heinrich C, Ovtcharova M, von Quadt A, Raicheva R (2005) 2: Hydrothermal ore deposits related to post-orogenic extensional magmatism and core complex formation: The Rhodope Massif of Bulgaria and Greece. Ore Geology Reviews 27:53–89.

Melfos V, Voudouris P (2017) Cenozoic metallogeny of Greece and potential for precious, critical and rare metals exploration. Ore Geology Reviews 89:1030–1057. https://doi.org/10.1016/j.oregeorev.2017.05.029

Melfos V, Voudouris P (2012) Geological, Mineralogical and Geochemical Aspects for Critical and Rare Metals in Greece. Minerals 2:300–317. https://doi.org/10.3390/min2040300

Reich M, Kesler SE, Utsunomiya S, Palenik CS, Chryssoulis SL, Ewing RC (2005) Solubility of gold in arsenian pyrite. Geochimica et Cosmochimica Acta 69:2781–2796. https://doi.org/10.1016/j.gca.2005.01.011

Repstock A, Voudouris P, Kolitsch U (2015) New occurrences of watanabeite, colusite, “arsenosulvanite” and “Cu-excess” tetrahedrite-tennantite at the Pefka high-sulfidation epithermal deposit, northeastern Greece. njma 192:135–149. https://doi.org/10.1127/njma/2015/0276

Voudouris P (2006) A comparative mineralogical study of Te-rich magmatic-hydrothermal systems in northeastern Greece. Mineralogy and Petrology 87:241–275. https://doi.org/10.1007/s00710-006-0131-y

Voudouris P, Mavrogonatos C, Spry PG, Baker T, Melfos V, Klemd R, Haase K, Repstock A, Djiba A, Bismayer U, Tarantola A, Scheffer C, Moritz R, Kouzmanov K, Alfieris D, Papavassiliou K, Schaarschmidt A, Galanopoulos E, Galanos E, Kołodziejczyk J, Stergiou C, Melfou M (2019) Porphyry and epithermal deposits in Greece: An overview, new discoveries, and mineralogical constraints on their genesis. Ore Geology Reviews 107:654–691. https://doi.org/10.1016/j.oregeorev.2019.03.019

Voudouris P, Repstock A, Spry PG, Frenzel M, Mavrogonatos C, Keith M, Tarantola A, Melfos V, Tombros S, Zhai D, Cook NJ, Ciobanu CL, Schaarschmidt A, Rieck B, Kolitsch U, Falkenberg JJ (2022) Physicochemical constraints on indium-, tin-, germanium-, gallium-, gold-, and tellurium-bearing mineralizations in the Pefka and St Philippos polymetallic vein- and breccia-type deposits, Greece. Ore Geology Reviews 140:104348. https://doi.org/10.1016/j.oregeorev.2021.104348

Whitney D, Evans B (2010) Abbreviations for Names of Rock-Forming Minerals. American Mineralogist 95:185–187.

Fault Permeability and Active Hydrothermal Systems: A Key to Infer the Formation of Unconformity-Related Uranium Deposits from Athabasca Basin (Canada)

Gaétan Milesi[1], Patrick Ledru[1], Paul Marchal[1], Matthieu Bourges[1], Clément Perrière[1], Jacek Scibek[2,3], Anthony Le Beux[4], Julien Mercadier[1]
[1]GeoRessouces, CNRS, Université de Lorraine, Labcom CREGU, France
[2]RWTH Aachen University, Germany
[3]Kyoto University, Japan
[4]ORANO, France

Abstract.
The Athabasca Basin region (Saskatchewan, Canada) hosts the highest grade and among the largest tonnage uranium deposits in the world. The formation of unconformity-related uranium (URU) deposits was essentially triggered by intense fluid circulations at the basin/basement interface that were channelized in a complex fault network. The development and the geometry of the fault systems had a first-order impact on the location and the size of uranium deposits. The intense fluid/rock interaction which affected that environment more than 1 Ga ago, however, strongly limits the characterization and quantification of these critical parameters. To overcome this problem, physical properties of fault systems and natural flow rates from active hydrothermal systems available in open databases have been used to define the possible range of values associated to fault permeability and fluid flow in the forming context (geometry/timing) of URU deposits.

1 Structural control on the formation of URU deposits of the Athabasca Basin

The Athabasca Proterozoic Basin region hosts some of the world's largest URU deposits (e.g. McArthur River, Cigar Lake) with uranium grading over 1% of up to 20% (Jefferson et al., 2007; Kyser and Cuney, 2015). These uranium deposits located at the interface between the basin and its crystalline basement were strongly controlled by a specific structural network marked by: i) the reactivation of basement-hosted faults and ii) the propagation of these fault and fracture networks through Athabasca Basin. The unconformity offset associated to fault reactivation is limited to 100s of meters and extends up to several kilometers along strike (Thomas et al., 2016; Ledru et al., 2022). Some of these fault systems channelized circulations of large volumes of uranium mineralizing fluids, the largest hydrothermal system being associated to the formation of "Giant" URU deposits. Such massive circulation of fluids, in addition to uranium deposition, is marked by large alteration haloes developed in both basement and basin (Kyser and Cuney, 2015; IAEA, 2018).

In this context, key elements for the formation of the URU deposits in the Athabasca Basin are questioned by Boiron et al. (2010), in particular: i) the origin and the composition of uranium mineralizing fluids, ii) fault fluid flows associated to mineralizing event and iii) timing and duration of the paleo-fluid circulations. Concerning i), the fluids are marked by the highest content of uranium known so far in crustal fluids (Richard et al. 2012). The questions regarding the nature and conditions of fluid flow(s) and their timing/duration are, however, still open and have mainly been approached based on ore deposit models and footprints (Jefferson et al. 2017, IAEA, 2018) or numerical simulations (e.g. Li et al. 2018; Poh et al., 2022). In order to constrain these parameters and define criteria that favored the formation of "giant deposits" in such environment, we propose to compare the geological models resulting from exploration and mined deposits with active or fossil systems on which properties of the faults and fluid flow have been better constrained. Large new databases on fault permeability (Scibek, 2020) and natural thermal springs (Tamburello et al., 2022) allow to investigate: i) the range of possible fault permeability according to the displacement, and kinematics of the faults and ii) flow rates associated to active hydrothermal systems. These parameters cannot be precisely quantified on fossil hydrothermal systems, and we therefore propose an analogical approach to characterize them.

2 Fault zone permeability and fluid flow

2.1 Fault zone permeability

The petrophysical properties active faults can provide critical information (e.g. Faulkner et al., 2010). Fault zones are characterized by two main domains of deformation with different hydro-mechanical properties: i) Core Zone(s) (CZ) associated to fault rocks: breccias, cataclasites, gouges… These zones commonly act as a barrier for fluid circulation when the fault is not active (e.g. Sibson, 2000), ii) Damage zones (DZ) that are a fractured rock volume along fault core, characterized by an increase in fracture density compared to the surrounding host rocks (Caine et al., 1996). The damage due to the fault activity increases the permeability of the host rock by several orders of magnitude, thus allowing fluid circulation in fault zone (Mitchell and Faulkner, 2012). It is worth noting that the permeability can be increased significantly during the deformation, especially for high fluid flux hydrothermal systems (Cox, 2010). The fault permeability database of

Scibek (2020) allowed to discuss the range of permeability in fault zones considering fault displacement and kinematic (Fig. 1).

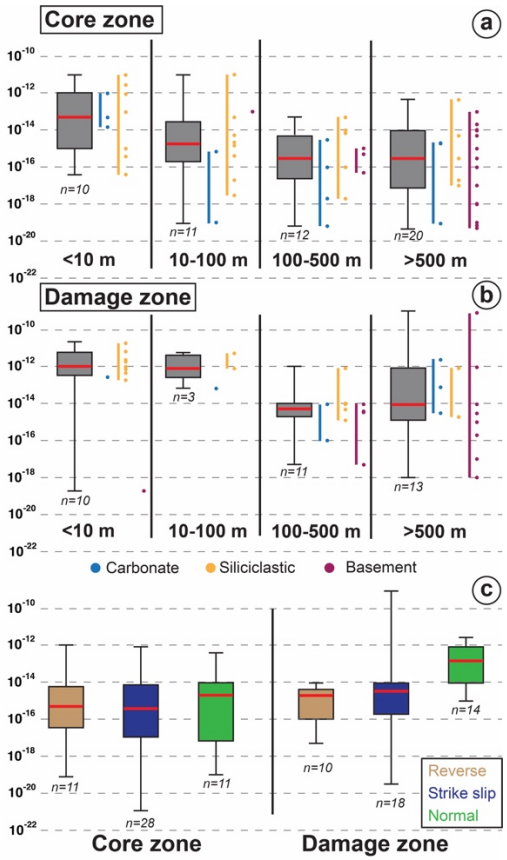

Figure 1. Box plots of CZ (a) and DZ (b) fault permeabilities according to different range of fault displacement, CZ and DZ permeabilities according to fault kinematic (c). The nature of host rocks is also considered. Database of Scibek (2020).

The CZ permeability (Fig. 1a) correlates to the fault displacement with median value ~10^{-13}-10^{-15} m^2 for displacement <100 m and ~10^{-16} m^2 for fault with displacement >100 m. This significant decrease of permeability could be representative of fault rock evolution from breccias to gouges (Fischer and Knipe, 2001). In the basement, CZ permeabilites for fault displacement >500 m show a wide range of values from 10^{-13} to 10^{-19} m^2. The permeability values obtained for the DZ (Fig. 1b) are globally higher than for the CZ. For fault displacement <100 m, DZ permeability are >10^{-13} m^2. The DZ permeability for fault displacement >100 m is lower with median value between 10^{-13} and 10^{-15} m^2. In the basement, DZ permeability for fault displacement >500 m shows a wide range of values from 10^{-12} to 10^{-18} m^2.

The apparent correlation between displacement and permeability must be interpreted with caution due to the lack of data for some fault displacement and results only for sedimentary photoliths for fault displacement <100 m. Basement faults with fault displacement >100 m are characterized by a wide range of permeability for CZ and DZ. Permeabilities in fault hosted in siliciclastics lithologies appear to be controlled by the fault displacement. It is important to consider that the evolution of thickness of the DZ associated to the fault displacement (Mayolle et al., 2019 and references inside) and its heterogeneity is not considered here.

Median CZ permeability is similar for the different fault kinematics, while median DZ permeability is higher for normal kinematic (~10^{-13} m^2) compared to reverse and strike-slip faults (~10^{-15} m^2, Fig. 1c). It is important to note a wide range of DZ permeability for strike-slip context. These values must be considered with caution because the fault length and initial protolith are not considered.

2.2 Water flow in active hydrothermal system

Tamburello et al. (2022) constitutes a database on ~6,000 worldwide thermal springs, including 1,483 flow rates. This synthesis shows a wide range of water flow values from 10^{-5} to ~5 $m^3.s^{-1}$ that are associated to various hydrothermal contexts. This important database gives typical values on fluid flow of natural hydrothermal systems. Extreme values (10%) that could be representative of atypical hydrothermal systems (e.g. volcanic systems, deep sea vents) and potential bias in the database are not considered. 90% of the value are representative of natural hydrothermal flow, that represent fluid flow between 10^{-4} (0.1 l/s) and 4.10^{-1} $m^3.s^{-1}$ (400 l/s) with a median value of 3.10^{-3} $m^3.s^{-1}$ (3 l/s). The range obtained are consistent with values obtained on other natural fault hydrothermal systems (Milesi, 2020) or geothermal systems (Glaas et al., 2021).

3 Implications for URU deposits of the Athabasca Basin

3.1 Fault zone permeability and geometry of uranium deposits

The characterisation of alteration halo and mineralisation geometries is essential for assessing uranium reserves and/or alteration clay volumes. We investigate the impact of faults to better understand how permeability contrasts between fault structures and the protolith can affect fluid flow, using a simple flow model, based on a Fast Marching Method (scikit-fmm), which relies on a permeability-based velocity field, using the Eikonal equation with F(x) the velocity field and T(x) the arrival time field:

$$F(x) * \overrightarrow{grad}\, T(x) = 1$$

The models in Figure 2a reproduces the main geometry of the Athabasca Basin with a tabular sedimentary basin (S_0) overlying a sub-vertical metamorphic basement (S_1). We used the same fault zone geometry: DZ of ~60 m and CZ of ~1 m with a basement source of fluid in the different models. Given that we used geologically realistic values of permeability, we tested different contrasts between the protolith and of the damage zone. This contrast is varying between 10^2 and 10^6 (Fig. 2a). The shape of the front has been assimilated to a

limit of alteration or mineralisation to calculate the area affected for the different scenarios (Fig. 2b). These models are a first approach, as they only consider the permeability (k) as a control of the front propagation. According to Zhang et al (2016), other parameters like fluid compressibility and fluid dynamic viscosity should be considered.

The numerical modeling results obtained (Fig. 2a) highlight a significant control of the damage zone permeability on the development of fluid front, with a global increase of the alteration area consistent with the permeability contrast between DZ and protolith. The results between basin and basement show some differences (Fig. 2b). A global area increase is observed both for basement and basin. We can note a sharp increase for basement alteration area from 10^6 contrast of permeability. A significantly higher contrast of 10^{10} is needed to observe an alteration area increase in the basin.

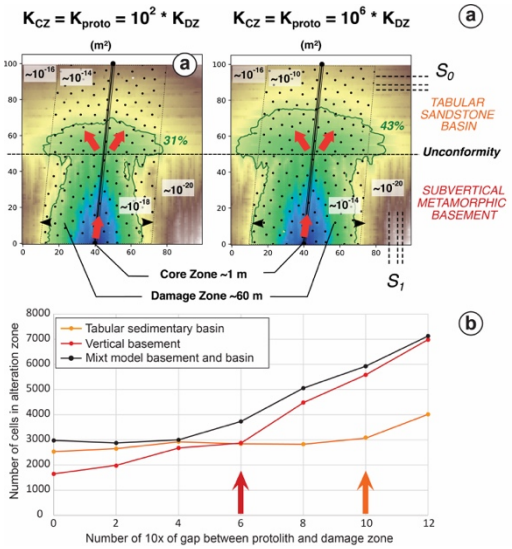

Figure 2. Front propagation model using fmm-scikit showing the effect of changing the permeability contrast on flow and altered areas.

3.2 Water flow implication for timing of formation of uranium deposits

Based on the database of Tamburello et al. (2022), we tested the minimum (0.1 l/s), maximum (400 l/s) and median value (3 l/s) for natural fluid flow using different uranium content in fluids: 0.1, 1 and 100 ppm to form a "giant deposit" of 100,000 tU. We considered 100%, 50% and 1% of uranium precipitation from fluids (Table 1).

The results obtained show that for the scenario of 100% of uranium precipitate from fluid all the fluid flow and uranium content in fluid can be generated from a range of time between 31.7 Myr and few years except for the lowest fluid flow and U content (317 Myr). For 50% of uranium precipitation efficiency, the results are between 63.4 Myr and ~1 kyr. Except for low uranium content in fluid (0.1 ppm) and fluid flow of 0.1 and 3 l/s, time to form U deposit are above 100 Myr. The last example, with only 1% of uranium precipitation efficiency from the fluid show the need of fluid flow of 400 l/s and/or high U content (100 ppm) to form "giant deposit" in less than 100 Myr.

Table 1. Table of fluid circulation duration to formed "giant deposit" of 100,000 tonnes U, Values with no indication are in Myr, the red values are duration above 100 My.

100% of uranium content in fluid mineralized				
		Fluid U content (ppm)		
		0.1	*1*	*100*
Fluid flow (l/s)	*0.1*	*317*	31.7	0.3
	3	11	1.0	0.01
	400	0.08	8 kyr	80 yr
50% of uranium content in fluid mineralized				
		Fluid U content (ppm)		
		0.1	*1*	*100*
Fluid flow (l/s)	*0.1*	*634*	63.4	0.6
	3	*22*	2.0	0.02
	400	0.16	0.02	> 1 kyr
1% of uranium content in fluid mineralized				
		Fluid U content (ppm)		
		0.1	*1*	*100*
Fluid flow (l/s)	*0.1*	*31700*	*3170*	31.7
	3	*1056*	*105*	1.0
	400	7.9	0.7	< 8 kyr

4 Implications for URU deposits of the Athabasca Basin

Numerical modelling results showed significant increase of the altered area for very high contrasts of permeability between the DZ and protolith, i.e., 10^{10} in the basin and 10^6 for the basement. Fluid circulation in the basin will be channelized both by fault and permeable layers of the basin (Fig. 2a). Considering, the important initial permeability of siliciclastic protolith compared to the basement lithologies (Fisher and Knipe, 2001), this very high contrast of permeability between fault DZ and basin protolith seems difficult to reach for faults with displacement ≤500 m (Fig. 1b). In Athabasca, the basement experienced several episodes of deformation (with different kinematics) that likely formed different generation of fractures and alteration. This tectonic superposition could have stimulated the permeability of these structures (e.g. Chauvet, 2019). The large range of values observed for DZ permeability (Fig. 1b) shows the potential of basement fault to localize high permeability contrast that can channelize large volume of mineralizing fluids until the unconformity.

The fluid flow associated to fault structures in the Athabasca Basin has been investigated using flow rates from active hydrothermal systems as analogy. The lifetime of hydrothermal circulation required for forming a giant U deposit is between 10 years and several hundred Myrs (Table 1) depending on the efficiency of redox, flow rates and U content in fluids. In the Athabasca Basin, Richard et al. (2012) proposed high U content in mineralizing fluids (>100 ppm) for the formation of "giant uranium deposits". Several authors considered also efficient redox processes associated to the formation of uranium deposits in the Athabasca Basin (e.g. Richard et al., 2012; Dargent et al., 2015). For such conditions, the lifetime of mineralizing hydrothermal circulation required for the formation of a "giant

deposit" can be estimated as less than 3 Ma regardless of the flow rate (Table 1). The formation of URU deposits is rapid at the geological time scale. This does not allow one to decide between a DZ-scale sustained fluid convection or fluid pulses associated with deformation (Cox, 2016). Further investigations in weakly mineralized zones could provide new clues to better understand the key phenomena in the formation of "giant uranium deposits".

5 Conclusions

Our results questioned the formation of URU deposits of the Athabasca Basin that could be also controlled by the contrast of permeability in basement fault zones. The location of uranium and alteration associated in the basin appear mainly controlled both by structural network and permeable layers. The flow rates do not constitute the only critical parameter for the formation of URU deposits. Considering the high U fluid content and efficient redox processes previously proposed in this area, a brief hydrothermal circulation from few years to ~3 Myr can form "Giant" URU deposits of the Athabasca Basin.

Acknowledgements

The authors acknowledge ANR funding, grant ANR-21-CHIN-0006 (project Geomin3D). T. Driesner for the abstract review.

References

Boiron M-C, Cathelineau M, Richard A (2010) Fluid flows and metal deposition near basement /cover unconformity: lessons and analogies from Pb-Zn-F-Ba systems for the understanding of Proterozoic U deposits. Geofluids. https://doi.org/10.1111/j.1468-8123.2010.00289.x

Caine JS, Evans JP, Forster CB (1996) Fault zone architecture and permeability structure. Geol 24:1025. https://doi.org/10.1130/0091-7613(1996)024<1025:FZAAPS>2.3.CO;2

Chauvet A (2019) Structural Control of Ore Deposits: The Role of Pre-Existing Structures on the Formation of Mineralised Vein Systems. Minerals 9:56. https://doi.org/10.3390/min9010056

Cox SF (2010) The application of failure mode diagrams for exploring the roles of fluid pressure and stress states in controlling styles of fracture-controlled permeability enhancement in faults and shear zones. Geofluids. https://doi.org/10.1111/j.1468-8123.2010.00281.x

Dargent M, Truche L, Dubessy J, et al (2015) Reduction kinetics of aqueous U(VI) in acidic chloride brines to uraninite by methane, hydrogen or C-graphite under hydrothermal conditions: Implications for the genesis of unconformity-related uranium ore deposits. Geochimica et Cosmochimica Acta 167:11–26. https://doi.org/10.1016/j.gca.2015.06.027

Faulkner DR, Jackson CAL, Lunn RJ, et al (2010) A review of recent developments concerning the structure, mechanics and fluid flow properties of fault zones. Journal of Structural Geology 32:1557–1575. https://doi.org/10.1016/j.jsg.2010.06.009

Fisher Q J and Knipe R J (2001) The permeability of faults within siliciclastic petroleum reservoirs of the North Sea and Norwegian Continental Shelf. Marine and Petroleum Geology, 18(10), 1063-1081. https://doi.org/10.1016/S0264-8172(01)00042-3

Glaas C, Vidal J, Genter A (2021) Structural characterization of naturally fractured geothermal reservoirs in the central Upper Rhine Graben. Journal of Structural Geology 148:104370. https://doi.org/10.1016/j.jsg.2021.104370

IAEA (2018) Uranium 2018: Resources, Production and Demand, in: OECD (Ed.), Red Book. p. 550.

Jefferson CW, Thomas DJ, Gandhi SS, et al (2007) Unconformity-associated uranium deposits of the Athabasca basin, Saskatchewan and Alberta. Geological Association of Canada, Mineral Deposits Division, Special Publication No. 5, pp. 273-305.

Kyser K and Cuney M. (2015) Chapter 8: Basins and uranium deposits: Mineralogical Association of Canada. Mineralogical Association of Canada, Short Course Series, 46: 225–304.

Ledru P, Benedicto A, Chi G et al (2022) The unconformity-related uranium mineral system of the Athabasca Basin (Canada). Dans Ressources métalliques 2, Decrée, S. (dir.). ISTE Editions, Londres

Li Z, Chi G, Bethune KM et al. (2018) Numerical simulation of strain localization and its relationship to formation of the Sue unconformity-related uranium deposits, eastern Athabasca Basin, Canada. Ore Geology Reviews, vol. 101, pp. 17–31, 2018. https://doi.org/10.1016/j.oregeorev.2018.07.004

Mayolle S, Soliva R, Caniven Y, et al (2019) Scaling of fault damage zones in carbonate rocks. Journal of Structural Geology 124:35–50. https://doi.org/10.1016/j.jsg.2019.03.007

Mitchell TM, Faulkner DR (2009) The nature and origin of off-fault damage surrounding strike-slip fault zones with a wide range of displacements: A field study from the Atacama fault system, northern Chile. Journal of Structural Geology 31:802–816. https://doi.org/10.1016/j.jsg.2009.05.002

Milesi G (2020). Analyse thermochronologique, géochimique et structurale du système hydrothermal de la faille de la Têt (Pyrénées, France): un nouvel outil d'exploration géothermique. Doctoral dissertation, University Montpellier. HAL Id: tel-0334031.

Poh J, Eldursi K, Ledru et al (2022) Role of Hydrothermal Circulation along and above Inherited Basement Structures Relating to Unconformity-Related Uranium Mineralization. Geofluids. https://doi.org/10.1155/2022/9131289

Richard A, Rozsypal C, Mercadier J, et al (2012) Giant uranium deposits formed from exceptionally uranium-rich acidic brines. Nature Geosci 5:142–146. https://doi.org/10.1038/ngeo1338

Scibek J (2020) Multidisciplinary database of permeability of fault zones and surrounding protolith rocks at world-wide sites. Sci Data 7:95. https://doi.org/10.1038/s41597-020-0435-5

Sibson RH (2000) Fluid involvement in normal faulting. Journal of Geodynamics 29:469–499. https://doi.org/10.1016/S0264-3707(99)00042-3

Tamburello G, Chiodini G, Ciotoli G, et al (2022) Global thermal spring distribution and relationship to endogenous and exogenous factors. Nat Commun 13:6378. https://doi.org/10.1038/s41467-022-34115-w

Thomas D. Aubin A., Zaluski G. (2016). What Does an Athabasca Basin Uranium Deposit Footprint Look Like? Empirical characteristics and the relevance to exploration. Saskatchewan Geological Society Luncheon, Nov. 2016.

Zhang Y, Bansal N, Fujita Y et al (2016). From Streamlines to Fast Marching : Rapid Simulation and Performance Assessment of Shale-Gas Reservoirs by Use of Diffusive Time of Flight as a Spatial Coordinate. SPE Journal, 21(05), 1883-1898. https://doi.org/10.2118/168997-PA

Study of Hydrothermally Altered Zones within the Gujarat-Khachkovi Ore Field Using Terra ASTER Multispectral Satellite Data. Georgia.

Giorgi Mindiashvili
Ivane Javakhishvili Tbilisi State University. Faculty of Exact and Natural Sciences, Department of Geology.

Abstract. This work involves the interpretation of data obtained through remote sensing analyses and techniques to identify geological features and potential ore fields in the Gudjareti-Khachkovi area of South-East Georgia, utilizing ASTER Multispectral satellite data. The conducted research indicates the significant roles of magmatic processes and hydrothermally altered zones within the studied area, which are characterized by pyritized, oxidized, and clay-altered rocks. These rocks are frequently highly fractured and cemented by quartz, as well as quartz-gold veins of various sizes, shapes, and orientations. It is evident that hydrothermal alterations and mineralization types do not fully depict the current geological processes in the study area. However, the research demonstrates a genetic relationship between ore mineralization processes and the region's magmatic activities. We anticipate that our findings will contribute to the enhanced utilization of remote sensing methods and increase the efficiency of ore exploration in Georgia.

1 Introduction

The study area exhibits abundant vegetation, snow, and glaciers, and is frequently affected by cloud cover. Consequently, efforts were made to acquire the most suitable satellite data from the available ASTER images to accurately represent the area while minimizing snow and cloud coverage. The satellite data was collected on November 24, 2021. The ASTER image used in this study indicates approximately 2% cloud cover, 20% vegetation, and 35% snow cover across the entire region. Despite the dense vegetation in the area, various rock types have been identified and characterized through lithological descriptions, mineral mapping techniques, and geological feature analyses. To verify the observed anomalies, ground truth studies should be conducted in the licensed areas. However, due to the small size of the area, it was not feasible to carry out these studies. Therefore, all analyses were performed using the complete ASTER image to detect all available geological features in the region. The Adjara-Trialeti region was formed as a rift zone at the end of the Cretaceous period and underwent folding during the Paleogene era. It primarily consists of trachytic and trachytic-andesitic volcanogenic-sedimentary rocks, although plutonic rocks also play a significant role in the overall structure. Plutonic rocks in the area include syenite, monzonite, and gabbro. Modern research suggests that syenite-trachytic magmatic activity can occur in subduction zones, mantle plume activity regions, post-collisional tectonic areas, and continental rift environments. In all cases, the formation of this type of magmatism is influenced by mantle magma on the lithosphere, followed by processes such as hybridism, assimilation, and metasomatism. The plutons within the Adjara-Trialeti folded zone form various types and sizes of bodies that intersect with igneous sedimentary rocks. Based on paleontological data, the volcanic-sedimentary formations are dated to the middle Eocene. Some researchers consider the plutonic bodies in the Adjara-Trialeti zone to be synchronous with volcanic activity, categorizing them as middle Eocene. Others identify multiple phases of intrusion. It is important to note that intensive hydrothermal ore mineralization processes often occur in the contact zones between igneous sedimentary rocks and plutonic bodies, leading to the formation of significant ore fields such as Merisi Vakijvari, Zoti, Garta-Dzama, Gujareti-Khachkovi, and others. The focus of our research is the Gujareti-Khachkovi ore field, which was investigated using remote sensing techniques. This research carries substantial scientific and practical importance.

2. Method of Study

Terra ASTER satellite data has been specifically developed for the purpose of detecting geological features on Earth. Depending on the objectives of the study, various data can be obtained through the analysis of the area. Consequently, the remote sensing method and analyses exhibit differences based on the specific objectives. A comprehensive examination of the entire ASTER image has been conducted, involving multiple analyses to determine lithological variations and perform the mineral mapping. Additionally, different algorithms have been employed to uncover details regarding structural elements and interpret the formation type. This study aims to explore the gold mine and associated geological features in the proposed Gudjareti-Khachkovi ore fields. The investigations conducted do not directly focus on analysing metallic minerals but rather aim to understand the formation environment of the considered mine deposit. Furthermore, methods have been applied to investigate alterations in mineralogy and the formation environment. ASTER data consists of three types of spectral bands: VNIR (visible near-infrared), SWIR (shortwave infrared), and TIR (thermal infrared). Initially, these spectral bands

were combined to create a comprehensive dataset. Subsequently, the ASTER data underwent atmospheric correction processing to eliminate moisture content and other atmospheric particles that could potentially impact the analysis negatively. The satellite image was georeferenced by incorporating the UTM (Universal Transverse Mercator) coordinate system and the WGS 84 datum in zone 38. Following the pre-processing stage, remote sensing analysis was conducted in accordance with internationally recognized standards and algorithms specifically developed for mine exploration. Due to the significant vegetation cover, snow, and wetlands present in the majority of the area, these regions were excluded from the image analysis and masked out. Thus, vegetation, snow, clouds, and wetlands were disregarded in the analysis. Only areas where rocks were observed in the images were selected for further image processing. Consequently, the investigation focused on examining the lithological and mineralogical features observed in very specific and narrow areas. In this process, regions, where these features exhibited continuity, were identified, and interpretations were made based on these specific areas. Therefore, not only the study area but the entire territory captured in the full image was thoroughly investigated.

2.1 Image analysis and results

It is important to note that the study in the study area was conducted for the first time using the remote sensing method. While it is evident that hydrothermal alterations and mineralization types may not fully depict the current geological processes of the study area, the conducted works have demonstrated a genetic relationship between ore mineralization processes and the magmatic activities in the region. The following analyses were carried out, and the results were obtained using ASTER data (Fig. 1). Through the remote sensing method, hydrothermally altered zones were identified, and the areas exhibiting geochemical anomalies were delineated (Fig. 2).

3. Conclusion

The conducted works have demonstrated that the data acquired through the remote sensing method accurately replicate the contours of the known mineral manifestations. This finding highlights the effectiveness of remote sensing in detecting and delineating existing mineralized zones. Additionally, the method has enabled the identification of several previously unknown and significant mineralization zones. These findings signify the potential for further exploration and prospecting activities within the study area. Based on the interpretation of the conducted studies, we emphasize the need for focused attention on the northern side of the research object. The presence of mineralization zones in this specific area warrants thorough investigation and exploration efforts. It is crucial to allocate resources and conduct detailed geological surveys, including fieldwork and geophysical studies, to gain a comprehensive understanding of the potential mineral deposits in the region. In conclusion, the promising results obtained from the remote sensing analysis of the Gudjareti-Khachkovi ore field indicate the importance of conducting comprehensive geological works in the future. These investigations should involve a multidisciplinary approach, incorporating various geological and geophysical techniques to further delineate and assess the potential for the presence of economically viable mineral deposits. Such endeavours will contribute to the broader understanding of the region's geological characteristics and aid in the identification of industrial-grade mineral resources.

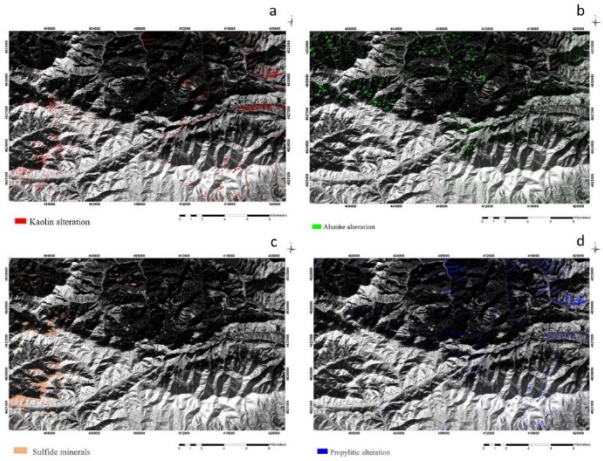

Figure 1. ASTER SWIR bands. Anomalies of mineralization zones

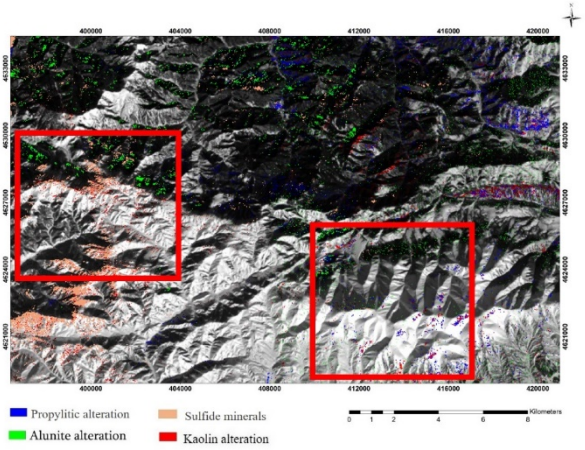

Figure 2. Complete picture of the survey conducted by the remote sensing method

Acknowledgements

This research [PHDF-21-179] has been supported by Shota Rustaveli National Science Foundation of Georgia (SRNSFG)

References

Gamkrelidze I. (1986) Geodynamic evolution of the Caucasus and adjacent areas in Alpine time. Tectonophysics, 127: 261-277.

.Duggen S., Hoernle K., Bogaard P. et al. (2005) Post-collisional transition from subduction- to intraplate-type magmatism in the westernmost Mediterranean: evidence for continental-edge delamination of subcontinental lithosphere. *J. Petrology*, 46: 1155-1201.

Ashwal L., Torsvik T., Horvath P., Harris C., et al. (2016) A mantle-derived origin for Mauritian trachytes. *J Petrology*, 57: 1645-1676.

Chung S.-L., Chu M.-F., Zhang Y. et al. (2005) Tibetan tectonic evolution inferred from spatial and temporal variations in post-collisional magmatism. *Earth-Sci. Rev*, 68: 173-196.

. Peccerillo A., Barberio M. R., Yirgu G. et al., (2003) Relationships between mafic and peralkaline silicic magmatism in continental rift settings: a petrological, geochemical and isotopic study of the Gedemsa volcano, central Ethiopian rift. *J. Petrol,* 44: 2003-2032.

David Bluashvili, Keti Benashvili, Giorgi Mindiashvili, David Makadze (2020) New Data on the Dzama-Gudjareti Ore Knot (Georgia), Bulletin of the Georgian National Academy of Scineses, vol. 14. No. 3.

Jong S.M.., Meer F.D.., Clevers J.G. (2004) Basics of Remote Sensing. In: Jong S.M.D., Meer F.D.V. Remote Sensing Image Analysis: Including the Spatial Domain. Remote Sensing and Digital Image Processing, vol. 5. Springer, Dordrecht. https://doi.org/10.1007/978-1-4020-2560-0_1

Yamaguchi, Y. & Naito, C. (2003) Spectral indices for lithological discrimination and mapping by using the ASTER SWIR bands. International Journal of Remote Sensing, 24, 4311- 432

Van Der Meer, F. (2002) Basic physics of spectrometry. In: F.D. Van Der Meer & S.M. De Jong (Eds.), Imaging Spectrometry. Basic Principles and Prospective Applications (pp. 3- 16). Hingham (MA), USA: Kluwer Academic Publishers.

Rowan, L., Hook, S., Abrams, M. & Mars, J. (2003) Mapping hydrothermally altered rocks at Cuprite, Nevada, using the advanced space borne thermal emission and reflection radiometer (ASTER), a new satellite-imaging system. Economic Geology, 98, 1019-1027.

Alimohammadi M., Alirezaei S., Kontak D.J., 2015. Application of ASTER data for exploration of porphyry copper deposits: A case study of Daraloo–Sarmeshk area, southern part of the Kerman copper belt, Iran. Ore Geology Reviews 70, 290–304.

Galley, A.G., Hannington, M.D., Jonasson, I.R., 2007. Volcanogenic massive sulphide deposits. In: GOODFELLOW W. D. ed. Mineral deposits of Canada: a synthesis of major deposit-types, district metallogeny, the evolution of geological provinces, and exploration methods. Geological Association of Canada, Mineral Deposits Division, Special Publication no. 5. St. John's, NL, Canada 141-161.

Hosseinjani Zadeh, M., Tangestani. M.H., Roldan. F.V., Yusta. I., 2014a. Spectral characteristics of minerals in alteration zones associated with porphyry copper deposits in the middle part of Kerman copper belt, SE Iran. Ore Geology Reviews 62, 191–198.

Mars, J.C., Rowan, L.C., 2006. Regional mapping of phyllic and argillic-altered rocks in the Zagros magmatic arc, Iran, using Advanced Spaceborne Thermal Emission and Reflection Radiometer (ASTER) data and logical operator algorithms. Geosphere 2, 161–186.

Mineralogy, Pb isotopes in galena, and Nd isotopes in associated dykes from the Ag-Hg Imiter deposit, Anti-Atlas, Morocco: implications for metal sources

Mehdi Ousbih[1], Brian Cousens[2], Yves Geraud[3], Alexiane Favier[3], Hafida El Bilali[4,5], Mohamed Ezzghoudy[1], Askkour Fatiha[1], Salim El Mouden[6], Abdelaziz Gaouzi[6], Oubaassine Hssane[7], Richard Ernst[4,5], Moha Ikenne[1]

[1]Department of Geology, Faculty of Sciences, Ibn Zohr University, Agadir, Morocco.
[2]Isotope Geochemistry and Geochronology Research Centre, Department of Earth Sciences, Carleton University.Ottawa, Canada.
[3]University of Lorraine-CNRS-GeoRessources, Nancy, France.
[4]Department of Earth Sciences, Carleton University, Ottawa, Canada.
[5]Department of Geology and Geography, National Research Tomsk State University, Russian Federation.
[6]Managem Group, Casablanca, Morocco.
[7]Department of Geology, Faculty of Sciences, Cadi Ayyad University,Marrakech, Morocco.

Abstract. The Imiter deposit is a significant silver-rich base metal deposit. The deposit is primarily composed of sub-horizontal ore bodies that occur at the contact between the Saghro Group (630-604 Ma) shales and Ouarzazate Group (590-540 Ma) volcaniclastics. The silver mineralisation occurs as steeply-dipping north-trending veins, low south-dipping veins and stockwork ore within conglomerates, tuffs and andesites. The ore mineralogy consists of Ag-Hg amalgam, argentite, polybasite, tetrahedrite-tennantite, proustite-pyrargyrite, acanthite, chalcopyrite, arsenopyrite, pyrite, sphalerite, and galena. The lead isotopic data of galena reveal two distinct groups, indicating two different origins for mineralizing fluids: one from the crust and the second from the mantle. The silver deposits are closely associated with a swarm of mafic to felsic dykes with different trends: NE to N70 in the Saghro Group and N-S to N10 in the OG. The first group is characterized by initial $^{143}Nd/^{144}Nd$ ratios ranging from 0.511787 to 0.511970, moderately negative εNd values (-0.15 to -2.78), and older Nd model ages (1.3-1.7 Ga), suggesting a locally enriched mantle source or significant crustal contamination. The second group has initial $^{143}Nd/^{144}Nd$ ratios between 0.511885 and 0.512075, Nd model ages between 1.00 and 1.29 Ga, and positive εNd values between 0.02 and 2.84, indicating a more juvenile source.

1 Introduction

The main primary Ag ore deposits are predominantly of hydrothermal origin and include various types such as epithermal (low-, intermediate- and high-sulfidation), volcanogenic massive sulphides (VMS), sedimentary-exhalative (SEDEX), sediment-hosted Ag–Cu, carbonate replacement and skarns, porphyry Cu, deeply formed mesothermal Ag–Pb–Zn, and Ag–Co–Ni–As veins (Kesler and Simon 2015). The Neoproterozoic-Cambrian transition period has significant implications for ore deposit metallogenesis and igneous crustal evolution in the northwest of the Western African Craton (Fig. 1). In Morocco, the known hydrothermal deposits are mostly associated with lithological units of the Anti-Atlas region. Important examples of such deposits include the Bou Azzer and the Imiter districts, which are currently being actively mined (Levresse et al. 2004; Ikenne et al. 2007, 2021).

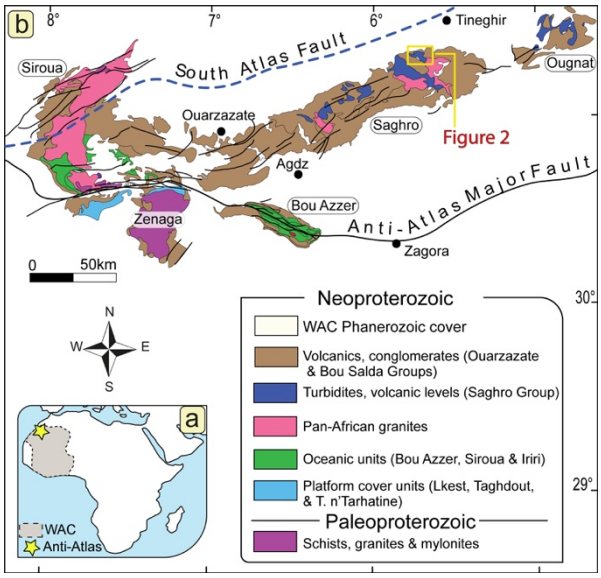

Figure 1. a. Location of the Anti-Atlas belt along the northwestern margin of the West African Craton. **b**. Simplified map of the eastern part of the Anti-Atlas belt, showing the main Precambrian inliers, with the location of the Imiter mine area labelled **Figure 2** (modified from Gasquet et al. 2005).

The Imiter Ag deposit (IAD), as the world's tenth-largest producer of Ag ores, has a long mining history dating back to the VIIIth century (Levresse et al. 2004). The ore bodies of the mine are controlled, and mainly distributed, along a major fault contact between lower Ediacaran turbiditic series and Late Ediacaran volcano-sedimentary, subvolcanic, and plutonic rocks (Fig. 2). The Ag mineralisation occurs also as steeply-dipping north-trending veins, south-dipping veins hosted within sandstones, all related to the major Imiter fault. Secondarily, the mineralization is also present in the form of stockwork ore within conglomerates, tuffs and andesites. The IAD is comprised of four main mining sectors, namely Imiter I, Imiter II, Imiter South, and Igoudrane. The mineralization exhibits diverse textures such as brecciated, ribbon, and disseminated textures, and the gangue minerals are primarily quartz and carbonates. The ore body Ag mineralization is closely associated with

intermediate to mafic dykes that crosscut the Saghro Group basement as well as the Ouarzazate Group. The genesis of the IAD has been a challenging problem in the Anti-Atlas region in recent years. Despite multiple geochemical investigations, important aspects such as the origin(s) of the ore-forming fluids, sources of heat and metal components, mechanism(s) of ore deposition, and the age of mineralization remain elusive.

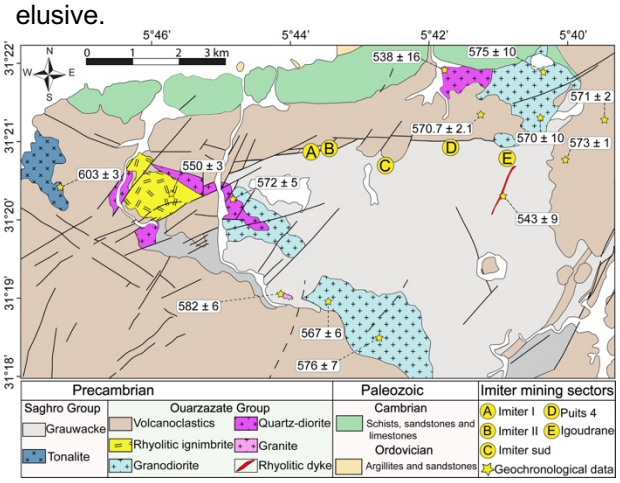

Figure 2. Geological map of the Imiter mine area showing the location of the mining sectors.

2 Methodology

Field mapping, core logging, outcrop sampling, and facies analysis were carried out during two field trips covering three cross-sections. Doubly polished thin sections were prepared for scanning electron microscopy (SEM), backscattered electron imaging (MEB), and electron probe microanalysis (EPMA). Additionally, twelve samples were selected for Pb isotope analyses based on criteria such as elevation, host rock, vein direction and orientation, mineralization texture, mineral assemblage, and Ag content. We collected twenty dykes and sills from the surface and underground workings around the mine for geochemistry and Nd isotopes. Based on their petrography, mineralogy, and texture, the dyke rocks are categorized into basalts, basaltic-andesites, andesites, quartz-microdiorites, and keratophyres.

3 Mineral chemistry

The main mineral phases associated with Ag have been analyzed in the Ag-Hg amalgam in sulfide and Ag stages (Baroudi 2002; Levresse et al. 2016): galena, pyrite, arsenopyrite, sphalerite,freibergite, and öllingite. The high Zn, Fe, Cu, and Sb contents in galena are associated with significantvariations in Pb content. Hg was absent from the analyses, ruling out the possibility of micro- inclusions of Ag-Hg amalgam. However, microanalyses conducted on other coexisting base sulfides revealed the presence of Hg, indicating that the hydrothermal system is rich in Hg and possibly supersaturated. A sharp change in physicochemical conditions (temperature, pH, salinity) likely caused the galena to incorporate higher amounts of Zn, Fe,Cu, and, to a lesser extent, Sb, Bi, and Mn, resulting in the absence of Hg (Baroudi et al. 2001; Levresseet al. 2004).

4 Pb isotope composition

The Pb isotope compositions of these samples were compared with other Anti-Atlas ores in conventional covariation diagrams, specifically the $^{207}Pb/^{204}Pb$ vs. $^{206}Pb/^{204}Pb$ and $^{208}Pb/^{204}Pb$ vs. $^{206}Pb/^{204}Pb$ diagrams. The data show a scattered distribution, but we identified two distinct groups (Fig. 3). The first group has $^{206}Pb/^{204}Pb$ values ranging from 18.172 to 18.540, observed in IGD-LN, R4, and SS1 structures. The Pb isotope values plot between the Stacey-Kramers (1975) curve and the Doe-Zartman (1979) orogene curve on the $^{208}Pb/^{204}Pb$ versus $^{206}Pb/^{204}Pb$ diagram, indicating a significant crustal component. The second group includes values ranging from 18.101 to 18.138, observed in the SS2, Igd-S, LN, N5, R6, F1S, SNN1, and F0 structures. These Pb isotope values plot significantly below both the Stacey-Kramers (1975) curve and the Doe-Zartman (1979) orogene curve on the $^{208}Pb/^{204}Pb$ versus $^{206}Pb/^{204}Pb$ diagram, consistent with a larger upper crust or mantle component.

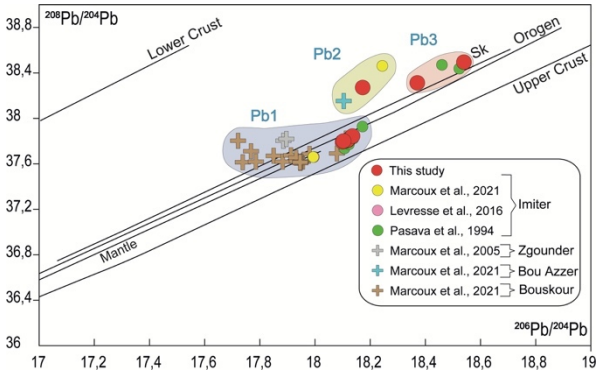

Figure 3. Plot of $^{208}Pb/^{204}Pb$ versus $^{206}Pb/^{204}Pb$ from Imiter mine and other Anti Atlas ores (Sk = Stacey-Kramers (1975); other curves from Zartman and Doe (1981)).

5 Nd isotopes of dykes

The OG cover, as well as the SG series are cross-cut by a swarm of dykes ranging in two main directions: NE to ENE in the SG series and N-S to NNE in the OG volcanoclastic series. The dykes are basalt, basaltic-andesite, dacite, microdiorite, and keratophyre. Based on the Nd isotope analyses, two distinct groups of IMD samples are identified (Fig. 4). The first group (IMD 1) displays initial $^{143}Nd/^{144}Nd$ ratios ranging from 0.511787 to 0.511970, moderately negative ℇNd values between -0.15 and -2.78, and older Nd model ages ranging from 1.3 to 1.7 Ga. In contrast, the second group (IMD 2) has initial $^{143}Nd/^{144}Nd$ ratios between 0.511885 and 0.512075, positive ℇNd values between 0.02 and 2.84, and model ages ranging from 1.00 to 1.29 Ga. Furthermore, the ℇNd values of the latter group (IMD 2) exhibit a negative correlation with SiO_2.

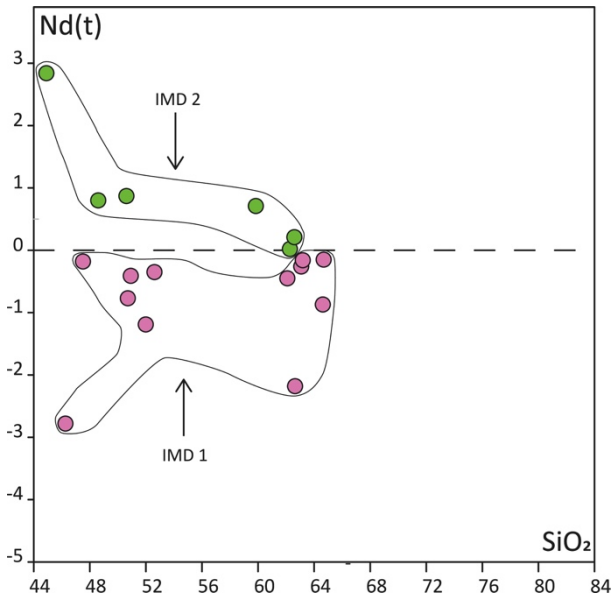

Figure 4. ᵢNd values exhibit a negative correlation with SiO_2 for the IMD 2.

6 Conclusions

The observed absence of Hg in galena is likely a result of sharp physicochemical changes, leading to enhanced incorporation of Zn, Fe, Cu, and, to a lesser extent, Sb, Bi, and Mn. The Pb isotope values exhibit two distinct groups, with the first group indicating a prominent contribution from the crust. The second group is characterized by a composition consistent with a larger influence from the upper crust or mantle. The dyke swarms associated with the IAD, including diverse silicic, mafic, and intermediate compositions, are classified into two groups based on distinctive Nd signatures.

References

Ikenne M, Ennaciri A, Ouguir H, Cousens B, Ziyadi R, Mouhagir M, El-Gaouzi A (2007) Geochemical signature and geodynamic significance of an ag-hg mineralized dyke swarm in the neoproterozoic inlier ofimiter - Anti-Atlas (Morocco). Ofioliti 32 (2): 109-18. https://doi.org/10.4454/ofioliti.v32i2.351.

Ikenne M, Souhassou M, Saintilan N. J, Karfal A, Hassani A. E, Moundi Y, Ousbih M, Ezzghoudi M, Zouhir M, Maacha L (2021) Cobalt–nickel–copper arsenide, sulfarsenide and sulfide mineralization in the Bou Azzer window, Anti-Atlas, Morocco: one century of multi-disciplinary and geological investigations, mineral exploration and mining. Geological Society, London, Special Publications 502(1): 45-66.https://doi.org/10.1144/SP502-2019-132.

Levresse G, Cheilletz A, Gasquet D, Reisberg L, Deloule E, Marty B, Kyser K (2004) Osmium, sulphur, and helium isotopic results from the giant Neoproterozoic epithermal Imiter silver deposit, Morocco: evidence for a mantle source. Chemical geology 207(1-2): 59-79. https://doi.org/10.1016/j.chemgeo.2004.02.004.

Kesler S, Simon (2015) Mineral Resources, Economics and the Environment (2nd ed.). Cambridge University Press, Cambridge https://doi.org/10.1017/CBO9781139871426.

Stacey J.S, Kramers J.D (1975) Approximation of terrestrial lead isotope evolution by a two-stage model.Earth Planet. Sci. Letters 26:207–221. https://doi.org/10.1016/0012-821X(75)90088-6.

Baroudi, Z., 2002. Le gisement Ag-Hg d'Imiter (Anti-Atlas Oriental) : minéralisation, fluides associés et conditionde dépôt. Doctoral dissertation, Thèse Doct d'Etat, Univ. Hassan II Mohammedia, Casablanca (Maroc), 280 p.

Vanadium and Indium enrichment in La Luz epithermal system, Patagonia, Argentina

Morena L.S. Pagola[1 2], Sebastián M. Jovic[1 2 3], Diego S. Palma[1 2], Diego M. Guido[1 2], Daniel Hughes[4]
1. Instituto de Recursos Minerales, Facultad de Ciencias Naturales y Museo, Universidad Nacional de La Plata, Argentina.
2. Consejo Nacional de Investigaciones Científicas y Técnicas, Argentina.
3. Departamento de Geología. Universidad de Buenos Aires, Buenos Aires, Argentina.
4. Trendix Mining S.A.

Abstract.
Vanadium and Indium are considered critical raw materials because of their economic importance and supply risk. The sustainable supply of these elements is fundamental for the global electronics industry and its role in the transition to clean energy (steel production for wind turbines, vanadium-based redox flow batteries, solar photovoltaic panels, and nuclear power in electricity generation). The La Luz project is a poorly explored intermediate sulfidation epithermal deposit located in Patagonia, Argentina. It isenriched in Cu, Ag, Pb, Au, and Zn and with rare enrichment inV, In, and W and anomalies of Ga, Bi, Mo, Sb, and Te. Recent whole rockanalyses of ore samples have shown high concentrations inthese metals (up to 1455 ppm vanadium and 310 ppm indium). The presence of these metals, mainly V, is relatively rare in this type of deposit and represents a discovery in the region.

1 Introduction

The La Luz project is in the central part of Rio Negro province, Patagonia Argentina, 30 km northwest from the town of Los Menucos in the Los Menucos mining district(Fig.1).

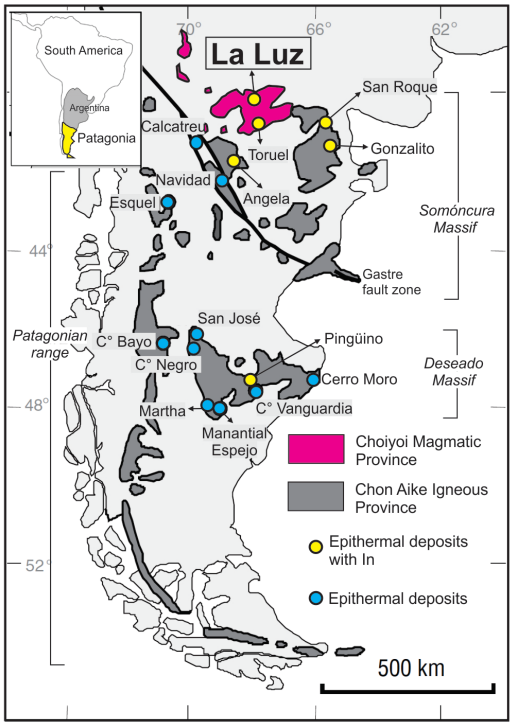

Figure 1. Map of the distribution of epithermal deposits in Argentine Patagonia, discriminating deposits where anomalous indium contents are observed. Modified from Jovic et al. (2015).

2 Regional geology

The Los Menucos mining district is located in the Somoncurá Massif, which is composed of an Early Paleozoic metamorphic complex (Pankhurst et al. 2006), overlain by marine clastic deposits (Silurian to Lower Devonian) of the Sierra Grande Formation (Caminos 1999), intruded by Permian (La Esperanza Complex), and Triassic plutonic and volcano-sedimentary rocks (Los Menucos Complex), alternating with Upper Jurassic calc-alkaline and bimodal subaerial volcanism of the Chon Aike Silicic Large Igneous Province, a long-lived (>25 Ma) extensional volcanism (Pankhurst et al., 2000). Above are Jurassic sedimentary rocks. Large basaltic lava flows of the Oligocene age cover about 15,000 km2 of this massif. There are two important Jurassic deposits at the Somoncurá massif, Navidad (23,441.7 t Ag and 1.35 Mt Pb, world-class according to Singer, 1995) and Calcatreu (2.325 g/t AuEq) which are aligned along the same Gastre regional fault, an NW-SE cortical scale structure.

3 La Luz project

The system has been interpreted as an intermediate sulfidation epithermal deposit with gold, silver, indium, lead, copper, zinc, molybdenum, and vanadium anomalies associated with quartz and carbonate vein systems. Several vein systems have been recognized in the study area, but we will focus on those in which anomalous amounts of V and In have been detected; they are the La Luz *sensustricto,* Gael, Esmeralda, and Mila I system. The main minerals identified are galena, sphalerite, malachite, chrysocolla, and native copper.

3.1 La Luz vein system

It is a system of sigmoidal quartz veins forming a structure 220 meters long and 60 meters wide. The mineralization consists of galena, chalcopyrite, and sphalerite with high silver content and minor gold (Fig. 2 A). Recent whole rock analyses of ore samples have yielded indium values up to 310 ppm and vanadium up to 744 ppm (Table I).

3.2 Gael vein system

It is composed by 14 veins of variable width ranging between 0.30 and 1.10 meters. A saccharoidal quartz vein with abundant manganese oxide, arsenic oxide, malachite, and azurite is observed at surface(Fig. 2 B). Geochemistry showed high silver, copper, and vanadium values up to 699 ppm and indium up to 50 ppm (Table I).

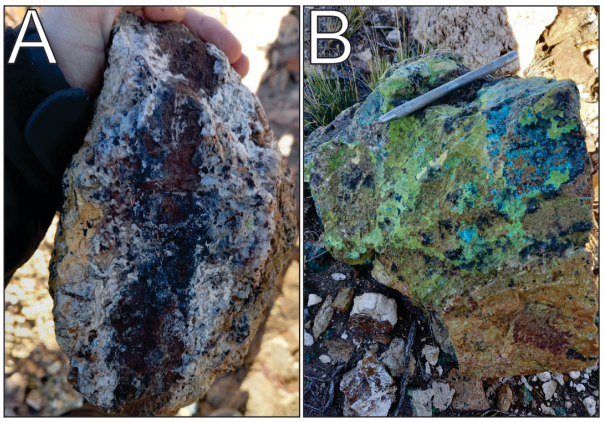

Figure 2. La Luz vein system(A) and Gael vein system(B) at the surface.

3.3 Esmeralda vein system

The vein is 40 cm thick and of unknown length. Atthe surface, it containshigh amounts of manganese and arsenic oxides with galena, sphalerite, and covellite (Fig. 3 A). ICP analyses of ore samples showed high amounts of vanadium (up to 1455 ppm), 149 ppm gallium, and 175 ppm indium (Table I).

3.4 Mila vein system

It consists of three vein structures, with a visible strike length of 250 meters varying in width from 1.10 to 2.8 meters (Fig. 3 B). A brown saccharoidal quartz vein, with fine sphalerite, minor hematite and siderite, is observed at surface. Geochemistry showed high values of silver, gold, lead, zinc, and over 880 ppm vanadium (Table I).

	La Luz	Gael	Esmeralda	Mila I
Au	0.33	2.1	0.42	13.44
Ag	159	>100	340	2.154
Cu	>10000	>10000	7152	483
Pb	>10000	>10000	55366	5292
Zn	>10000	3350	9007	2141
In	310	50.3	175	13
V	744	699	1455	882
W	440	199	420	520

Table I. Whole rock analyses in ppm (www.trendixmining.com.ar).

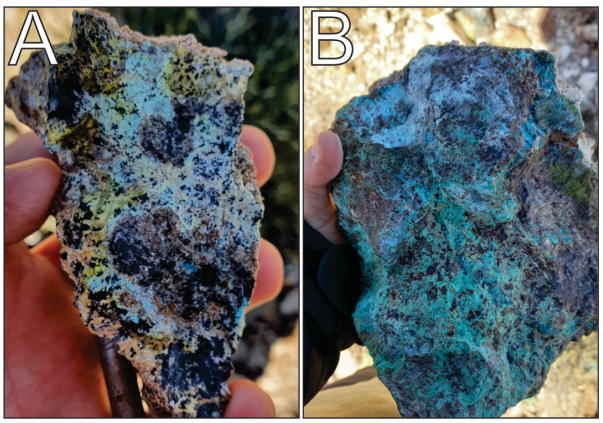

Figure 3. Esmeralda system vein (A) and Mila I vein at the surface (B).

4 Final considerations

A considerable anomaly of vanadium and indium, rare metals in this type of deposit, was found in surface samples. A positive correlation between Cu-In is observed and could reflect the coupled substitution of In and Cu in the sphalerite, for example, a coupled substitution of 2(Zn, Fe)for Cu-In (Johan 1988, Ohta 1989, Sinclair et al. 2006). A positive correlation between Pb-V is also observed, which is likely related to the presence of some lead vanadate such as vanadinite. These metals, mainly V, are relatively rare in epithermal systems and represent a discovery in the region.

Regarding the vanadium source, V^{+3} replaces Fe^{+3} in iron-rich minerals such as amphibole, biotite, magnetite, and pyroxene; and Al^{+3} in the structure of secondary minerals such as clays (micas, smectites, illite, kaolinite, and chlorite), Fe-Mn hydrated oxides and organic-rich facies during diagenesis (Lipinski et al., 2003). Carbonaceous shales can contain up to 16,000 mg kg^{-1} (Vine and Tourtelo, 1970) compared to non-carbonaceous shales that average 130 mg kg^{-1} V (Turekian and Wedepohl, 1961). Considering all this, we can think of two possible sources of V, 1) dioritic intrusions of the Los Menucos Complex or 2) sedimentary rocks (with shales and carbonaceous facies) of the Puesto Vera Formation (also belonging to the Los Menucos Complex).

The assemblage of these metals increases the mining potential and must be considered during future exploration duties.

References

Caminos, R. (1999): Geología Argentina; Subsecretaría de Minería de la Nación, Servicio Geológico Minero Argentino, Instituto de Geología y Recursos Minerales, Anales N°29.

Johan, Z. (1988): Indium and germanium in the structure of sphalerite: an example of coupled substitution with copper. Mineral. Petrol. 39, 211-229.https://doi.org/10.1007/BF01163036

Jovic, S. M., López, L., Guido, D., Redigonda, J., Páez, G., Ruiz, R., Permuy Vidal, C. (2015):Presencia de índio ensistemasepitermalespolimetálicos de Patagonia. Rev AsocGeol Argent 71: 433–437.

Ohta, E. (1989): Occurrence and chemistry of indium-containing minerals from the Toyoha mine, Hokkaido, Japan. Mining Geol. 39, 355-372.https://doi.org/10.11456/shigenchishitsu1951.39.218_355

Rapela, C. W., Pankhurst, R. J., Fanning, C. M., y Herve, F. (2005): Pacific subduction coeval with the Karoo mantle plume: the early Jurassic subcordilleran belt of northwestern Patagonia. Terrane Processes at the Margins of Gondwana; Geological Society of London, Special Publications, 246:217–239. https://doi.org/10.1144/GSL.SP.2005.246.01.0

Sinclair, W.D., Kooiman, G.J.A., Martin, D.A. &Kjarsgaard, I.M. (2006): Geology, geochemistry and mineralogy of indium resources at Mount Pleasant, New Brunswick, Canada. Ore Geol. Rev. 28, 123-145 https://doi.org/10.1016/j.oregeorev.2003.03.001

Singer, D.A. (1995): World class base and preciousmetal deposit: A quantitative analysis. EconomicGeology, v.90,p.88-104. https://doi.org/10.2113/gsecongeo.90.1.88

Turekian, K.K., Wedepohl, K.H. (1961): Distribution of the elements in some major units ofthe earth's crust. Geol. Soc. Am. Bull. 72 (2), 175–192.

Vine, J.D., Tourtelo, E., (1970): Geochemistry of black shale deposits-a summary report.Econ. Geol. 65 (3), 253–272.

Using PHREEQC for mineral prospecting in waters related to geothermal systems in Wyoming: possible precipitation of hydroxyapatite enriched with REEs

Juan David Palma Montealegre[1] , Thomas Heinrich Cramer[1]
[1] Departamento de Geociencias, Universidad Nacional de Colombia – Sede Bogotá, Colombia.

Abstract. The increasing demand for REEs related to the transition to a green energy encourages their exploration using innovative methodologies. This project discusses the use of the PHREEQC software to get information about the minerals that may precipitate in waters related to geothermal systems, as function of the temperature (T(C°)), pH, and chemical composition of water, in a case study in Wyoming, USA. We have modelled the data of 46 different samples, with an array of 18 different minor and major chemical constituents. The results show the possible precipitation of 36 diverse mineral phases, highlighting, for some minerals, a trend to increased precipitation in warmer and more basic waters. The investigation focused on 9 locations with possible precipitations of hydroxyapatite, a mineral able to capture REEs in aqueous systems. These locations are related to the Wasatch Formation, which consists of sedimentary rocks with reports of frequent detrital monazite and apatite presence. The REEs were plotted in a spider diagram to argue the potential enrichment of REEs in the hydroxyapatites of each location. This project highlights an innovative methodology for REE-bearing mineral exploration, which can be improved and potentially used in other prospective areas.

1 Introduction

Geothermal systems are important for the economic development of humanity, not only as sources of geothermal energy, but also for the mobilization of various chemical elements and their subsequent precipitation in minerals. This chemical mobilization represents an opportunity for research on critical elements for Energy Transition, such as Li and REEs, using new methodologies and techniques.

The U.S. Department of Energy has carried out numerous studies about the concentration of REEs in geothermal fluids in the USA (Quillinan et al. 2018), resulting in the elaboration of hydrogeochemical datasets that can be used for modelling using PHREEQC Version 3 (Parkhurst 2013), which is a software package that allows performing geochemical calculations for aqueous systems. It can simulate the behaviour of aqueous solutions that contain multiple dissolved species, including ions, gases, and solids. PHREEQC uses a set of thermodynamic and kinetic data to calculate the equilibrium concentrations of the various species in solution. The data processing can provide important information about the water-rock interaction and consequently the origin of the fluid and the history of its passage through underground materials in shallow and deep reservoirs (Chidambaram et al. 2012).

This project uses PHREEQC for Saturation Index (SI) calculation, which is a measure of how close the solution is to being saturated with respect to a specific mineral. The SI is defined as the log ratio of the ion activity product of the mineral to its solubility product at a given T(C°) and pressure, i.e., SI = log(IAP/Ksp), where IAP is the ion activity product, divided by the mineral solubility product (Ksp) at a given T(°C) and pressure. SI > 0 indicates supersaturation or tendency to precipitation of minerals, whereas SI < 0 means undersaturation or dissolution of minerals.

The use of PHREEQC as a tool for mineral prospection consists in looking at the relationship of SI for different mineral phases, focusing on hydroxyapatite (Hyap), with T(C°), pH, as well as the location of the water sample. This methodology was applied using a dataset called “REEs in Produced Waters in Wyoming” (Quillinan 2017) with chemical data from 46 water samples in Wyoming, USA, close to Jackson, Green River, Gillett, Riverton, and Cheyenne (Figure 1). From this dataset we retrieved information about T(°C), pH, depth (samples from wells and from springs), concentrations of minor and major constituents (Al, Ba, Ca, Cl, F, K, Li, Mg, Na, SO_4, B, Mn, P, Si, Br, Fe, NH_4, Sr) in mg/L, and concentrations of REEs (Ce, Dy, Er, Eu, Gd, Ho, La, Lu, Nd, Pr, Sc, Sm, Tb, Tm, Yb) in ng/L.

The geothermal system of Wyoming is result of at least three different factors (Breckenridge 1978): for NW-Wyoming, the convection of hot fluids associated with the Yellowstone Plateau volcanic field, as well as heat conduction from the Yellowstone Hotspot (Christiansen et al. 2002); and for middle east Wyoming, the geothermal gradient increase due to the sediment load accumulated since the Cretaceous in the Western Interior Basin (Milliken 2007).

2 Results and discussion

2.1 Saturation Indices

Using the chemical composition of the 46 water samples at different T(°C) and pH, PHREEQC calculated the SI for 36 different possible mineral phases. The SI variation is analysed as function of Temperature (Figure 2) and pH (Figure 3). The relationship between the calculated SI and T(°C) shows the tendency of each mineral to precipitate in a temperature range from 5.3 to 63.1°C.

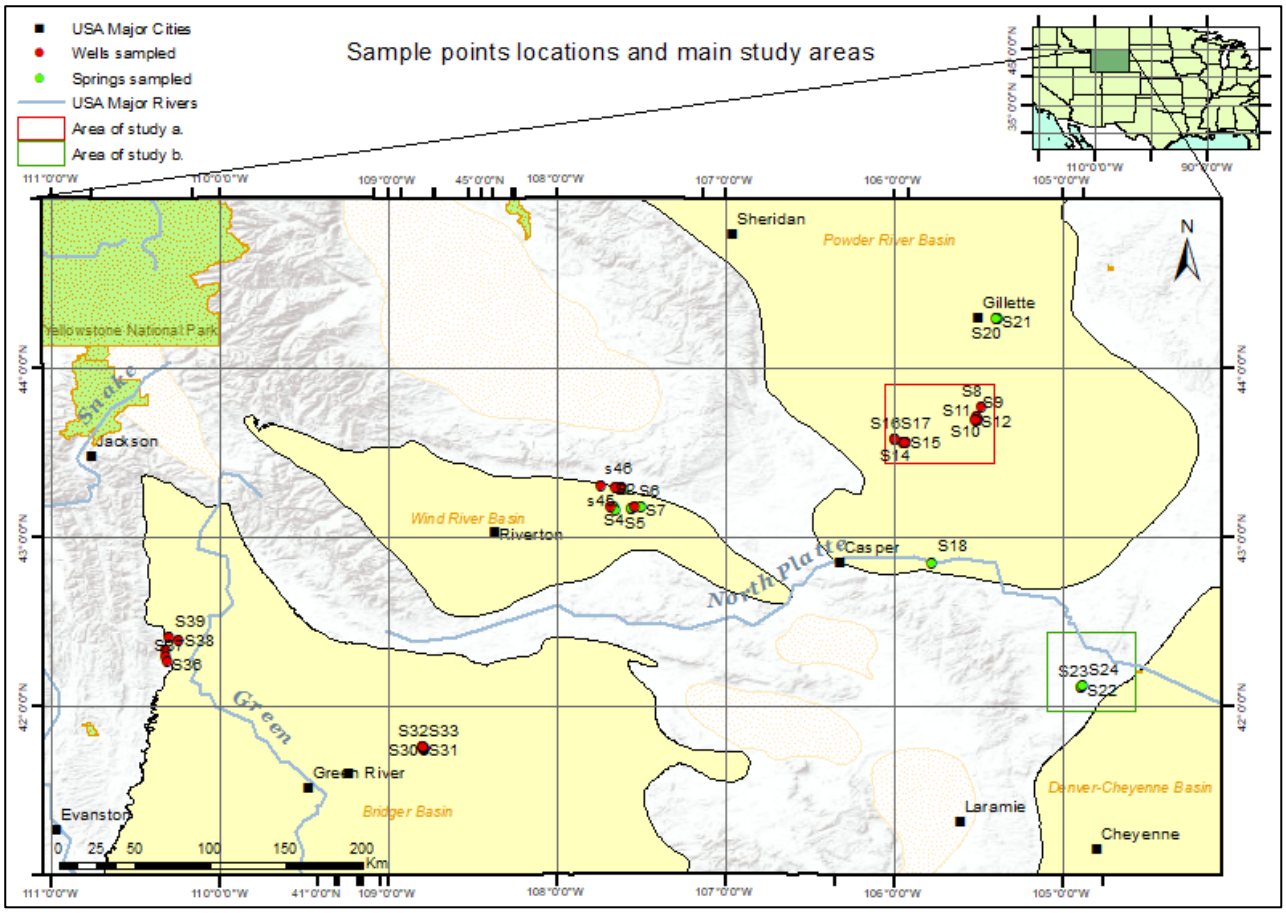

Figure 1. Map of the Wyoming state with the location of the 46 sampling points (labelled as SN (N=1-46)), and the polygons of two main study areas a) and b) discussed in Figure 5. Also shown are the principal basins, i.e., Powder River Basin, Wind River Basin, Bridger Basin, and the Denver-Cheyenne Basin

Although other variables like pH, pressure, and chemical constituent concentration must be considered, some minerals show a maximum SI value for T ≥ 45°C (albite, anorthite, Ca-montmorillonite, hydroxyapatite, illite, K-feldspar, muscovite, kaolinite, and vivianite), while others for T < 15°C ($Al(OH)_3$, alunite, anhydrite, celestite, chlorite, chrysotile, dolomite, $Fe(OH)_3$, fluorite, gibbsite, goethite, gypsum, halite, hematite, jarosite-K, rhodochrosite, sepiolite, siderite, sylvite, talc, and witherite).

The SI relationship with pH shows additional interesting tendencies to investigate. In a pH-range from 6.53 to 10.01, most of the minerals reached maximum SI values in almost neutral waters (pH 7-8) with some exceptions which reached their maximum SI values in more basic waters (pH ≥ 8). These exceptions are $Al(OH)_3$, alunite, anhydrite, celestite, chlorite, chrysotile, dolomite, $Fe(OH)_3$, fluorite, gibbsite, goethite, gypsum, halite, hematite, sepiolite, sylvite, talc, and witherite; resulting in a typical behaviour of SI in the function

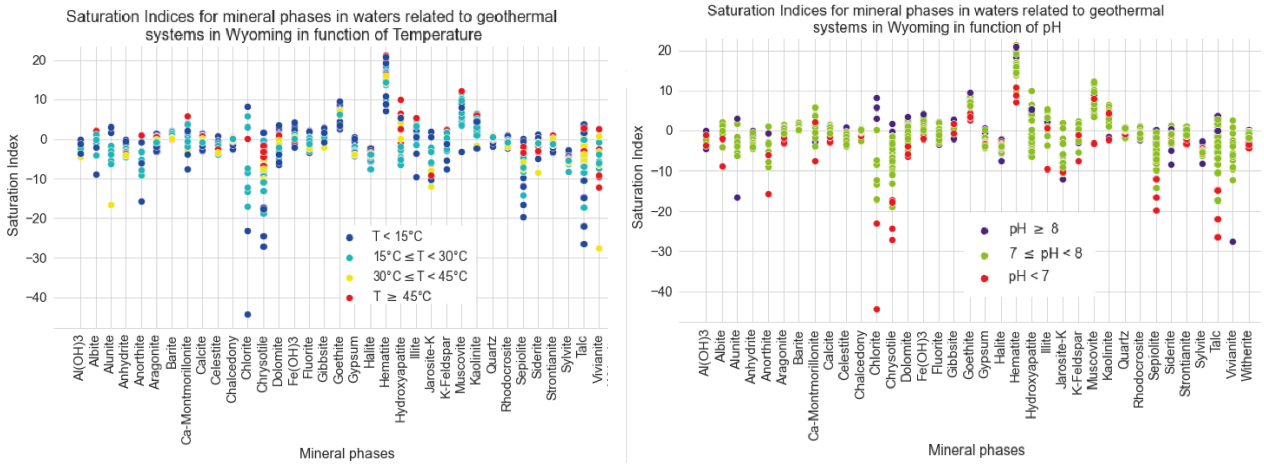

Figure 2. SI for the 36 mineral phases possibly formed in 46 water samples as function of Temperature.

of pH.

Figure 3. SI for the 36 mineral phases possibly formed in 46 water samples as function of pH.

Minerals with maximum SI-values in more basic waters are the same as those with maximum tendency to precipitate at T < 15°C, except for jarosite-K, rhodochrosite, and siderite, showing that, for some species, the pH will likely be the prevalent saturation factor, not temperature. One of the conclusions here is a higher possibility of minerals to precipitate in the water samples at T ≥ 45°C and/or pH ≥ 8.

2.2 Hydroxyapatite: REE absorption potential

Hydroxyapatite (Hyap) can effectively sorb REEs from aqueous solutions (e.g., Granados-Correa 2012, Ignjatović et al. 2019). The mechanism behind this sorption is believed to be due to the ion-exchange properties of Hyap, where the positively charged REE ions are attracted to the negatively charged phosphate groups in the Hyap structure, and a certain occupation of the two Ca^{2+}-sites in the apatite structure. Additionally, the surface properties of Hyap, such as area and porosity, can also play a role in the sorption of REEs. Hyap nanoparticles, for example, have been shown to have a high surface area-to-volume ratio, which can increase their ability to sorb REE (Fleet 1999).

2.3 Hydroxyapatite: possible distribution and geological context

The section 2.1 demonstrates the tendency of Hyap to precipitate in some water samples at locations where waters have T > 30°C or pH > 7.2. This relationship is shown in Figure 4, which is also useful to represent graphically the tendency for some minerals to form in waters with T ≥ 45°C or pH ≥ 8, a statement of the end of 2.1 section.

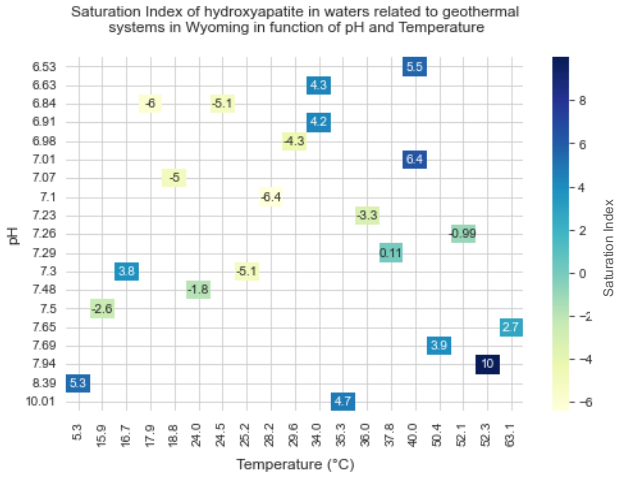

Figure 4. SI for hydroxyapatite in the function of pH and T(°C).

The sample points labelled as SN (N=1-46), show a positive Hyap-SI for: S8, S10, S11, S12, S13, S14, S15, S16, and S23. All these water samples were taken from a well in the subsurface, excluding S23, which was sampled from a spring. Their geographical distribution is shown in Figure 5, which is a map that also allows comparing the

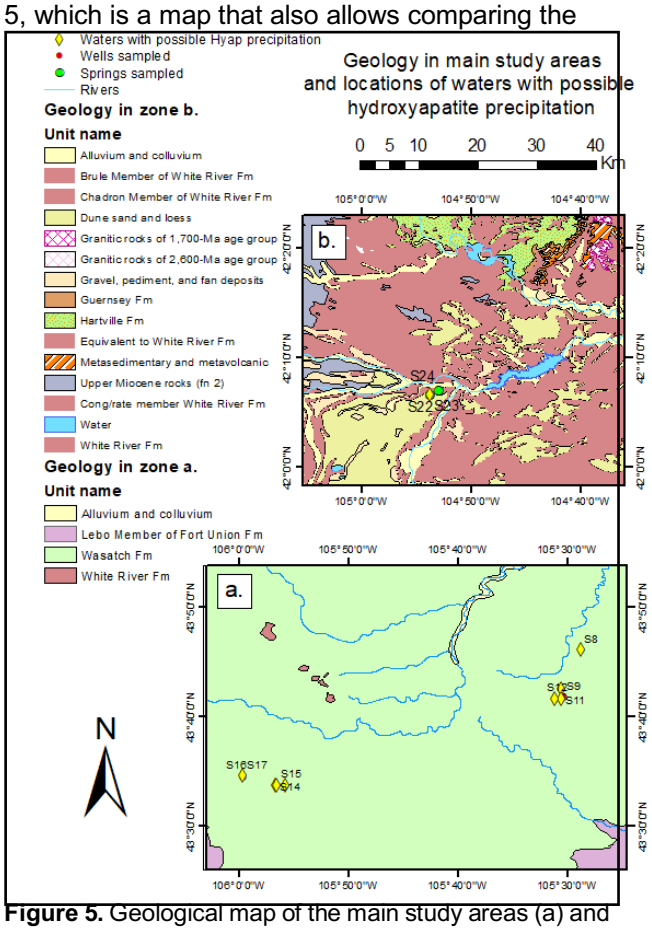

Figure 5. Geological map of the main study areas (a) and (b) with location of waters with possible hydroxyapatite precipitation.

geology of the area with the composition of the waters with positive Hyap-SI and shows the two different areas (a) and (b) from Figure 1. In zone (a) the main geological formation that can affect the composition of the water is the Wasatch Formation, which outcrops in the Powder River Basin and is made up of sedimentary rocks, including sandstone, shale, and siltstone, which were deposited during the Eocene. It contains also large amounts of coal formed from plants and trees in a lacustrine ambient (Divay 2016). This formation has also abundant detrital apatite and monazite (Pocknall 1987).

In zone (b) the principal geological formation is the White River Formation, which consists primarily of sandstone, siltstone, and mudstone, deposited in various environments such as rivers, lakes, and floodplains during the Eocene (Emry 1975).

This geology helps us explaining the presence of phosphorus and calcium to produce hydroxyapatite nowadays. In zone (a), the presence of detrital apatite and monazite can be also associated with the Bear Lodge Mountains, located in the northwest of Gillette, where an alkaline complex with REE mineralization from carbonatites outcrops which host fluorocarbonates (bastnäsite, parisite, and synchysite), ancylite, monazite, cerianite, burbankite, and carbocernaite (Moore et al. 2015), but this relationship needs to be tested in future research. Zone (b), in comparison with zone (a), has no reports of detrital apatite or monazite on the White River Formation

yet. This geological difference may be the reason why zone (a) presents higher contents of P (Table 1), but more samples must be taken in zone (b) to make the comparison clearer.

To better understand the possible REEs-Hyap absorption in waters shown in Figure 5, the REEs concentrations were plotted in the spider diagram of Figure 6 following the methodology of Quillinan (2018).

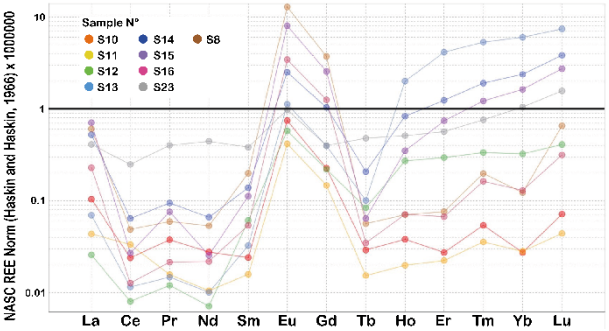

Figure 6. REE-concentration normalized to NASC in the water samples of areas (a) and (b) influenced by the clastic apatite-monazite, and carbon-rich sedimentary Wasatch Formation and the sediments of the White River Formation.

The most relevant concentrations and characteristics of the water samples with positive Hyap-SI are presented in Table 1. This work can motivate responsible REE extraction from geothermal systems as by-products using hydroxyapatite. For future research, other geothermal systems can be modelled to find correlations with this work or other possibilities for extraction of critical minerals to the development of society, like REEs themselves, lithium, and silica, among others.

Table 1. most relevant concentrations and characteristics of the water samples with positive Hyap-SI. N/A means "Not data available". Data from Quillinan (2017).

SampleN°	Location	P(mg/L)	Ca(mg/L)	T(°C)	PH	Hydroxyapatite SI	∑REE (ng/L)
S5	Close to Riverton	4.9	3	35.3	10.01	4.72	11.27585558
S8	Zone (a)	0.8	734	16.7	7.3	3.78	68.42256417
S10	Zone (a)	19.2	83	52.3	7.94	9.99	9.546970852
S12	Zone (a)	1.6	60	50.4	7.69	3.92	10.20288777
S13	Zone (a)	1.8	1680	40	7.01	6.36	54.91360515
S14	Zone (a)	14.6	814	40	6.53	5.51	53.50249862
S15	Zone (a)	5.6	386	34	6.91	4.25	62.57984922
S16	Zone (a)	1.8	1770	34	6.63	4.3	22.25289777
S23	Zone (b)	0.5	198	5.3	8.39	5.33	68.66972272
S43	Close to Riverton	2.6	13	63.1	7.65	2.74	N/A
S44	Close to Riverton	1.9	22	37.8	7.29	0.11	N/A

3 Conclusions

Using PHREEQC as a tool for mineral prospection is an innovative methodology with some limitations and uncertainties. The input data may be found in hydro-chemical databases and adjusted to the objective. For the studied waters from wells and springs close to Jackson, Green River, Gillett, Riverton, and Cheyenne in Wyoming, hydroxyapatite and absorbed REEs tend to precipitate in waters with T ≥ 45°C or pH ≥ 8.

Acknowledgments

This work was possible thanks to the support of the SGA Student Chapter, beginning with Anna Vymazalová, who encouraged the first author to make the investigation, and all the SGA Student Chapter UNAL Bogotá family. Thanks to professors Ariel Cadena, Clemencia Gómez, Germán Prieto, and Daniel Hernández. Finally, thanks to Scott Quillinan et al. for letting their database open to use, and the Universidad Nacional de Colombia for their apport in the knowledge applied in this work.

References

Breckenridge R.M., Hinckley B.S. (1978): Thermal Springs of Wyoming. The Geological Survey of Wyoming bulletin, 60: 1-3.

Chidambaram S., Anandhan P., Prasanna M.V., Ramanathan A.L., Srinivasamoorthy K., Kumar G.S. (2012): Hydrogeochemical Modelling for Groundwater in Neyveli Aquifer, Tamil Nadu, India, Using PHREEQC: A Case Study. Nat Resour Res 21(3):311–324.

Christiansen R. L., Foulger G. R., & Evans J. R. (2002). Upper-mantle origin of the Yellowstone hotspot. Geological Society of America Bulletin, 114(10), 1245-1256.

Divay J.D., Murray A.M. (2016): An early Eocene fish fauna from the Bitter Creek area of the Wasatch Formation of southwestern Wyoming, U.S.A. J Vertebr Paleontol 36(5):e1196211.

Emry R.J. (1975): Revised Tertiary Stratigraphy and Paleontology of the Western Beaver Divide, Fremont County, Wyoming. Smithson Contrib Paleobiol 25:1–20.

Fleet M.E., Liu X., Pan Y. (2000): Site Preference of Rare Earth Elements in Hydroxyapatite [Ca10(PO4)6(OH)2]. J Solid State Chem 149(2):391–398.

Granados-Correa F., Vilchis-Granados J., Jiménez-Reyes M., Quiroz-Granados L.A. (2013): Adsorption Behaviour of La(III) and Eu(III) Ions from Aqueous Solutions by Hydroxyapatite: Kinetic, Isotherm, and Thermodynamic Studies. J Chem 2013:751696.

Ignjatović N.L., Mančić L., Vuković M., Stojanović Z., Nikolić M.G., Škapin S., Jovanović S., Veselinović L., Uskoković V., Lazić S., Marković S., Lazarević M.M., Uskoković D.P. (2019): Rare-earth (Gd3+,Yb3+/Tm3+, Eu3+) co-doped hydroxyapatite as magnetic, up-conversion and down-conversion materials for multimodal imaging. Sci Rep 9:16305.

Milliken M. (2007). Geothermal resources at Naval petroleum reserve-3 (NPR-3), Wyoming. In PROCEEDINGS of Thirty-Second Workshop on Geothermal Reservoir Engineering, Stanford University.

Moore M., Chakhmouradian A. R., Mariano A. N., & Sidhu R. (2015). Evolution of rare-earth mineralization in the Bear Lodge carbonatite, Wyoming: Mineralogical and isotopic evidence. Ore Geology Reviews, 64, 499-521.

Parkhurst D.L., Appelo C.A.J. (2013): Description of input and examples for PHREEQC version 3: a computer program for speciation, batch-reaction, one-dimensional transport, and inverse geochemical calculations. Technical Report. U.S. Geological Survey.

Quillinan S., Nye C., Neupane G., and McLing T. (2017): Rare Earth Element Concentrations in Wyoming's Produced Waters. United States. U.S. Geological Survey. Technical Report. University of Wyoming. Dataset obtained from the Geothermal Data Repository.

Quillinan S., Nye C., Engle M., Bartos T.T., Neupane G., Brant J., Bagdonas D., McLing T., McLaughlin J.F., Phillips E., Hallberg L.L., Shahabadi M., Johnson M. (2018): Assessing rare earth element concentrations in geothermal and oil and gas produced waters: A potential domestic source of strategic mineral commodities. Technical Report. University of Wyoming.

3D lithological and structural model and prospectivity of the Late Cretaceous Sakdrisi Gold-Copper Epithermal deposit, Bolnisi district, Lesser Caucasus, Georgia

Nino Popkhadze[1], Badri Gogia[2], Shota Tagviashvili[2], Giga Ugrekhelidze[2], Malkhaz Natsvlishvili[2], Joni Shubititze[2], Şafak Utku Sönmez[3], Robert Moritz[3]
[1]Al.Janelidze Institute of Geology of Iv.Javakhishvili Tbilisi State University&RMG Rich Metals Group
[2]RMG Rich metals Group, Georgia
[3]Department of Earth Sciences, University of Geneva, Switzerland

Abstract. The Bolnisi mining district is located at the north-eastern extremity of the Lesser Caucasus metallogenic belt and to the west it continues into the Eastern Pontides. The Late Cretaceous Sakdrisi epithermal deposit is one of the on-going exploration targets in the Bolnisi ore district. Detailed mapping, detailed lithological and the structural database for 3D modelling allowed us to discover new ore zones and promising resources for the future. The ore zones in the Sakdrisi deposit are related to a lower volcano-sedimentary (VS) complex, where an upper VS complex consists of barren welded ignimbrite and cross cutting dikes. The main ore bodies are controlled by central and southern faults and a meridian fault located between the Sakdrisi 4 and 5 open pits. Pumice-bearing rock types together with explosive breccia where channelways for the ore-forming fluids. Thus, the deposit is both lithologically and structurally controlled.

1 Introduction

The Sakdrisi gold-copper epithermal deposit of the Bolnisi district is located in a distinct zone within the eastern extension of the eastern Pontides in Turkey (Moritz et al 2020; Yilmaz et al 2000) (Fig.1A), and belongs to the Tethyan metallogenic belt, linking the Anatolian and Iranian tectonic zones. Numerous ore deposits and prospects are known in the Bolnisi district, where Late Cretaceous bimodal volcanism resulted in mafic and felsic rock types. The latter are a major host of ore deposits and prospects, and are locally known as the felsic Mashavera and Gasandami suites. Mineralization in Bolnisi district occurs in two different age groups: in Turonian to early Santonian host rocks (Madneuli deposit; Tsiteli Sopeli, Kvemo Bolnisi and Kazreti prospects) and in Campanian hosts (Sakdrisi and Beqtakari deposits; Darbazi, Imedi, Bnelikhevi and Samgreti prospects) (Gugushvili, et al. 2014) (Fig.1B).

2 Regional geology and stratigraphy

The Late Cretaceous Sakdrisi gold-copper deposit is one of the major deposits of Bolnisi district. The Bolnisi volcano-tectonic depression is a part of the Artvin-Bolnisi belt, which is characterized by an arc association formed mainly during the Liassic-Campanian interval and represents a distinct tectonic zone along the Tethyan metallogenic belt. This favorable geotectonic location of the Late Cretaceous Bolnisi ore district between the Lesser Caucasus and the Eastern Pontides is reflected by its geological diversity and mineral deposit distribution.

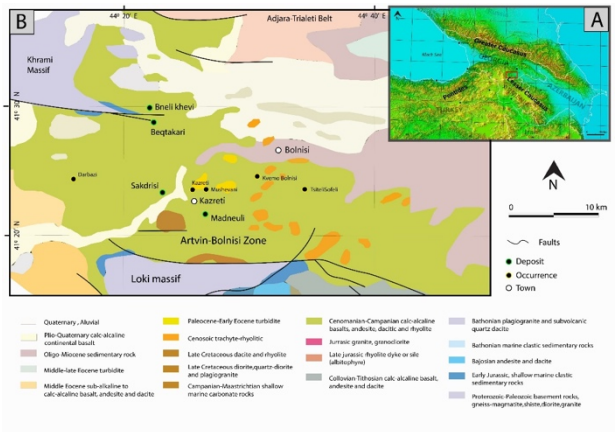

Figure 1. A) Location of the Bolnisi district, B) geological map of the Bolnisi mining district with ore deposits and occurrences.

The Artvin-Bolnisi zone comprises a Hercynian orogenetic basement, which consists of Precambrian and Paleozoic granite, gneiss and plagiogranite, cropping out in the Khrami and Loki massifs, overlain by Carboniferous volcano-sedimentary rocks (Fig.1B). Within the Artvin-Bolnisi zone, the 3000-4000 m thick Late Cretaceous section is dominated by calc-alkaline basalt, andesite, dacite and rhyolite (lava, and pyroclastic rocks) (Fig.1B). Volcanic rocks belong to shallow marine to subaerial settings. Predominant Late Cretaceous volcanic and volcano-sedimentary rocks in this region include rhyodacitic ignimbrite, ash fall and density current deposits with a phreatomagmatic origin (Popkhadze et al 2017; Popkhadze et al 2014). Based on lithological and paleontological data, Late Cretaceous sequences in this region are subdivided into six volcanogenic suites and correspond to Cenomanian and Maastrichtian in age (Apkhazava 1988). The bimodal character of Late Cretaceous volcanism is manifested by the alternation of mafic and felsic suites stratigraphically and geochemistry (Moritz et al

2020). The arc-related, calc-alkaline volcanic rocks include abundant pyroclastic rocks, lava, extrusive domes, and subvolcanic intrusions and dikes, with a predominantly rhyolitic, dacitic and andesitic composition, except one Santonian suite (Tanzia) and one late Campanian suite (Shorsholeti), which are dominantly basaltic and partly alkaline in composition (Gugushvili et al 2014; Popkhadze et al 2014). The Late Cretaceous volcanic rocks were deposited in a shallow-water environment (Adamia Sh et al 2011).

3 The geology of the Sakdrisi deposit

3.1 Host rock characteristics

The Sakdrisi deposit consists of a 2 km long cluster of five mineralized centers aligned along a NE-oriented thrust fault zone (Golay et al 2018). Two complexes have been recognized in the Sakdrisi deposit hosted by the Mashavera Group, including: the Lower Volcano-Sedimentary Complex (LVSC) and the Upper Volcano-Sedimentary Complex (UVSC) (Jelev et al. 2020; Popkhadze et al 2021), separated by a NE oriented thrust fault zone (Golay 2019; Golay et al 2018). The Lower volcano-sedimentary complex (LVSC) is composed of a thick (over 200m) sequence of alternating pumice tuff, massive and layered ash tuff, clastic rocks with different size of pumice rich horizons, locally transition from a pumice-rich part to fine-grained intervals, layered tuff with gypsum and ignimbrite-like tuff (Fig.2).

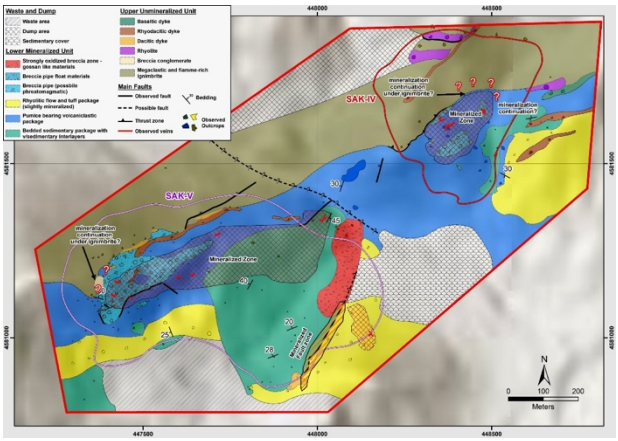

Figure 2. The geological map of the Sakdrisi 4 and 5 open pits.

The upper parts of this complex have been affected by intense silification and associated Au-Cu mineralization. The Upper volcano-sedimentary complex (UVSC) includes ignimbrite. Apart from typical vitroclastic (fiame) ignimbrite, this suite includes also bomb and block intervals, layers of pelitic ash tuff. UVSC is intruded by andesite-basaltic and rhyolite/rhyodacitic dikes (Popkhadze et al 2022; Popkhadze et al 2023). This sequence is non-mineralized, which overlaps the lower mineralized sequence, documented by the thrusted ignimbrite pyroclastic flow.

3.2 3D geological model of the Sakdrisi deposit

A 3D lithological-structural and ore bodies model was constructed in Leapfrog Geo, using historical and new geological maps and the drill hole database recorded in an Excel sheet. In total, 200 drill holes were described and interpreted from the Sakdrisi 5 and 4 ore bodies (part from Sakdrisi 3 also) (Figs.3 and 4).

Based on drill hole description and mapping the following lithostratigraphic units have been identified in the UVSC:

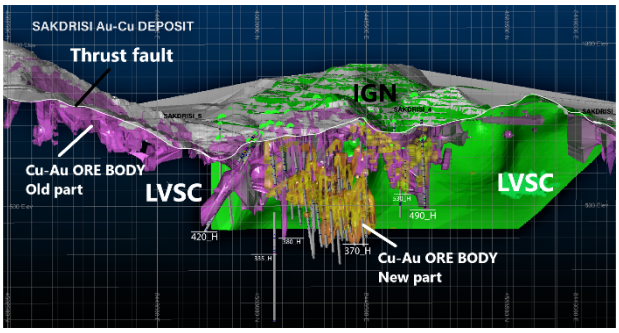

Figure 3. 3D Lithological-structural model of the Sakdrisi 4 and 5 ore bodies, with ore distribution zones.

welded ignimbrite, rhyodacitic and andesite-basaltic dikes and sedimentary formation (SF), which is the thrust fault zone with crushed and clay-altered black sedimentary rocks, in some places the so-called breccia - conglomerate and tuff. The lower LVSC consists of: pumice tuff, massive fine-grained tuff, pumice tuff with transition intervals to fine-grained, thin-bedded tuff/mudstone with gypsum veins and ignimbrite-like tuff. Explosive breccia crosscuts these lower lithological units at different levels and hosts gold-copper ore bodies. The upper mineralized lithological unit (pumice tuff) in some places is strongly oxidized and silicified. As these sequences are crosscut by mafic and felsic dikes. The non-mineralized upper (UVSC) and lower (LVSC) are separated by a thrust fault zone, including the sedimentary formation (SF), which is also non-mineralized.

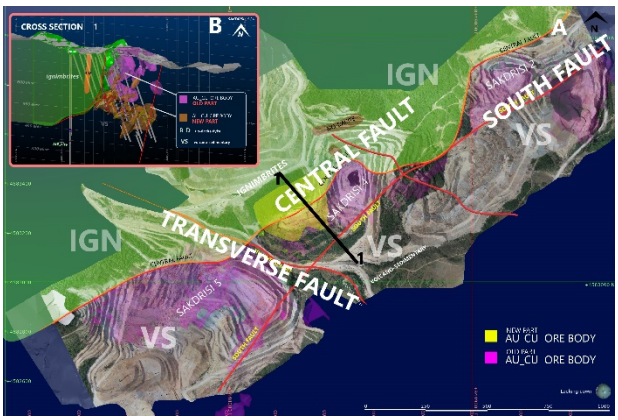

Figure 4. 3D regional model of the Sakdrisi deposit, with modelled faults, lithology and principal open pit locations.

Explosive breccia: explosive breccia outcrops in the Sakdrisi 5 and partly in the Sakdrisi 4 open pits. In Sakdrisi 5, it is possible to see the stratigraphic/sharp contact of the explosive breccia with different lithological units (Fig. 5): crosscutting the pumice tuff and bedded VS complex. The breccia consists variably sized, rounded and sharp rock fragments of pumice tuff, massive fine-grained tuff, black clayey tuff and locally bedded tuff (Fig.6A). The breccia varies between clast-rich and matrix –rich varieties.

Figure 5. The lithological units and fault zones with a gossan-like supergene ore location in Sakdrisi 5.

Some of the rock fragments contain quartz sulphide veins with chalcopyrite also in the matrix, some places cross cutting with quartz/quartz sulphide veins/veinlets and stockworks. In Sakdrisi 5, it is still possible to observe the classical breccia pipe injected in oxidized clastic pumice tuff (Fig.6B).

Figure 6. A. Explosive polymictic breccia with different rock fragments: bedded fine-grained tuff and pumice tuff. B. Polymictic breccia pipe injected in an oxidized pumice tuff.

In Figure 7, we have illustrated the preliminary 3D scheme of distribution of explosive breccia pipe from the Sakdrisi 4 ore body in the lower LVSC mineralized unit and correlation with ore bodies morphology (Fig.7).

Structural modelling (Figs. 4 and 5): The central fault is represented by a thrust fault zone with upper barren ignimbrite, the South fault is very clear at the Sakdrisi 5 open pit, where it is a sharp contact of bedded grey/bluish bedded rocks (gypsum-bearing in some places) with strongly oxidized and silicified pumice tuff and fine-grained tuff units (Fig.5). The northwest-oriented transverse fault is identified between the Sakdrisi 5 and Sakdrisi 4 ore bodies, also Sakdrisi 4 and Sakdrisi 3 and Sakdrisi 3 and Sakdrisi 2 (Fig. 4) (Migineishvili et al 2009).

Figure 7. 3D Lithological-structural model of the Sakdrisi 4 ore body with explosive breccia pipes and ore bodies.

4 Ore bodies: distribution and types

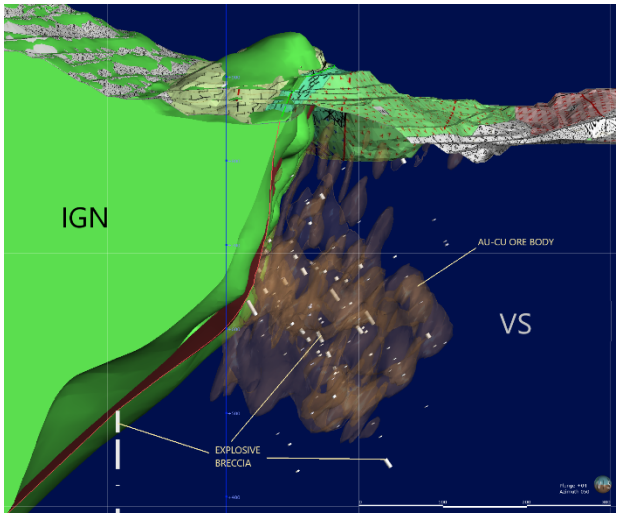

Veins: a vertical zoning of gold grades was observed in quartz/quartz barite and quartz/sulfide veins and low to medium grade in stockworks. Disseminated ore is present in permeable host rocks and in explosive breccia. Supergene mineralization: mostly the upper part of the LVSC (pumice tuff) is affected by surface weathering and supergene overprint is in located areas of the main (mostly consists gold mineralization and locally copper also). Thus, the mineralization is commonly hosted in high permeability zones (pumice tuff), either restricted to subvertical veins or explosive breccia or disseminated in intensively leached rocks. The gossan-like supergene ore with highest gold concentrations and less copper was recognized in Sakdrisi 5 (Fig. 5), where gossan horizon consists of alluvial heterolithic breccia consisting of eroded and transported gossans displaced possibly as far as several hundred meters away from their sources. The distribution of major minerals throughout the gossan profiles like goethite, hematite, quartz and jarosite and the statistical analyses distinguish three separate zones, which was well observed on the profile and was a gradual contact with roughly parallel to current topography. Possibly subsequent local uplift of the gossan-rich rocks by neotectonic movements facilitated the rejuvenation of the oxidation of the ores.

4 Conclusions and recommendations

Two major trends of faults are recognized in the Sakdrisi area: NE and NW directions and dikes also are oriented mostly to the NE direction. The central fault/thrust fault developed when ignimbrite pyroclastic flow was thrusted and overlapped

already the mineralized zone. Thus, the Central fault represents the upper limit of mineralized zone. The south fault zone is represented by a sharp contact with strongly oxidized and silicified with the LVSC unit, which raises the doubt that this fault is later than mineralization, although it is still a subject of study. The transverse faults are very noticeable in this deposit at this stage.

The lower base of mineralization zone in Sakdrisi 4 is observed in some drill holes in layered tuff with gypsum veins and locally ignimbrite-like tuff. Recent data from 400–600 m deep drill cores indicate enriched mineralized zones, which is a new discovery for this deposit. To develop the similar drilling project will be increased the perspectivity of the Sakdrisi deposit.

It is possible to conclude, that in the Sakdrisi deposit there is both a structural and a lithological control: the fault system created the fractures along which mineralized quartz, quartz-barite and quartz-sulfide and sulfide veins have been emplaced. The explosive breccia is mostly mineralized, even non-mineralized explosive breccia pipe in the close system created very fractured/permeable zones for fluid migration. Clastic/pumice-bearing rocks from Sakdrisi deposit is a good permeable rock, which here is strongly oxidized and mostly gold-bearing.

In conclusion, the 3D modelling of the Sakdrisi deposit is critical in this study allowing to visualize and integrate different datasets (from old and new drillings) in a lithological, structural and stratigraphic interpretation connected with the ore bodies distribution. 3D modelling of ore bearing explosive breccia outlines the spatial circulation of hydrothermal fluids in the system.

Acknowledgements

The authors would like to thank the Rich Metal Group for access to open pits and prospects, and for logistical support. The research would not have been possible without constant support provided by SGA, SEG and IAVCEI organizations for attending many international conferences, where the works about the Bolnisi district has been presented.

References

Adamia Sh, Zakariadze G, Chkhotua T, Sadradze N, Tsereteli N, Chabukiani A, Gventsadze A (2011) Geology of the Caucasus: A review. Turkish Journal of Earth Sciences, v.20: 489-544

Apkhazava M (1988) Late Cretaceous volcanism and volcanic structures at Bolnisi volcano-tectonic depression (Doctoral dissertation). Tbilisi, Georgia; Caucasus Institute of Mineral resources; 0-304

Gugushvili v, Bukia A, Goderdzishvili N, Javakhidze D, Zakaraia D, Muladze I, Shavishvili I, Shubitidze J, Tchokhonelidze M (2014) Bolnisi ore district: geological development and structure, genesis of mineralization, economic potential and perspectives. Caucasus Mining Group, Tbilisi. Ed. Natsvlishvili MP 55 p (in Russian)

Golay T, Moritz R, Popkhadze N, Natsvlishvili M (2018) The Sakdrisi Au-Cu deposit, Bolnisi mining district, Georgia: providing a genetic model based on petrographic, geochemical, structural, and alteration studies. The 16th Swiss Geoscience Meeting, Bern, Switzerland, 30 November-1st December, pp. 104-105

Golay T (2019) The Sakdrisi Au-Cu deposit, Bolnisi mining district, Georgia: providing a genetic model based on petrographic, geochemical, structural and alteration studies. MSc thesis, University of Geneva. pp.1-181

Jelev V, Bitsadze N, Ananiashvili G, Aslanishvili G, Shavishvili I, Natsvlishvili M (2021) Litho-structural geological mapping of Sakdrisi and Madneuli deposits. Unpublished report for RMG. Tbilisi, Georgia. pp 0-31

Migineishvili R, Gaxaria D, Natsvlishvili M (2009) Geological map of Sakdrisi deposit. Unpublished enclosure report for RMG (In English)

Moritz R, Melkonyan R, Selby D, Popkhadze N, Gugushvili V, Tayan R, Ramazanov V (2016) Metallogeny of the Lesser Caucasus: From Arc Construction to Postcollision Evolution. Society of Economic Geologists, Special Publication 19, pp.157-192

Moritz R, Popkhadze N, Hassig M, Golay T, Lavoie J, Gugushvili V, Ulianov A, Ovtcharova M, Grosjean M, Chiaradia M, Dumitrica P (2020). At the crossroads of the Lesser Caucasus and the Eastern Pontides: Late to Early Eocene magmatic and geodynamic evolution of the Bolnisi district, Georgia. Lithos-105872, Volumes 378-379

Popkhadze N, Moritz R, Natsvlishvili M, Bitsadze N (2017) First evidence of phreatomagmatic breccia at the Madneuli Polymetallic Deposit, Bolnisi district, Lesser Caucasus, Georgia. In: proceedings of the 14th SGA biennial meeting: Mineral resources to discovery, 20-23 August, Quebec City, Canada; 1:323-326

Popkhadze N, Moritz R, Gugushvili V (2014) Architecture of Upper Cretaceous rhyodacitic hyaloclastite at the polymetallic Madneuli deposit, Lesser Caucasus, Georgia. Cent. Eur. J. Geosci 6(3):308-329

Popkhadze N, Sonmez S, Moritz R, Natsvlishvili M, Bluashvili V, Gagnidze N (2022) The Late Cretaceous Sakdrisi epithermal deposit, Bolnisi district (Lesser Caucasus, Georgia): Geology and ore deposit setting. XXII International Congress of the CBGA, Plovdiv, Bulgaria, 7-11 September.pp.362

Popkhadze N, Moritz R, Sonmez S, Lipartia T, Natsvlishvili M, Gogia B (2023) The Late Cretaceous volcanism in Bolnisi district: lithological, structural and stratigraphic control on ore deposits, Lesser Caucasus, Georgia. IAVCEI2023 Scientific Assembly, 30 June-3 February, Rotorua, New Zealand. P.855

Popkhadze N, Somenz S, Bluashvili V, Natsvlishvili M (2021) The Geological map of Sakdrisi deposit. Unpublished report for RMG. Kazreti, Georgia

Yilmaz A, Adamia Sh, Chabukiani T, Chkhotua T, Erdogan K, Tuzcu S, Karabilykogly M (2000) Structural correlation of the southern Transcaucasus (Georgia)-Eastern Pontides (Turkey)-Tectonics and magmatism in Turkey and the surrounding area. Geological Sosiety of London Spesial Publication, 173:171-182

A Comparative Study of VMS and Epithermal Deposit Settings in the Eastern Pontides, NE Turkey: Insights from Geochronology and Lithogeochemistry

Şafak Utku Sönmez[1], Robert Moritz[1], Serdar Keskin[2], François Turlin[1], Alexey Ulianov[3], Ümit Aydın[2]
[1]Department of Earth Sciences, University of Geneva, Rue des Maraîchers 13, 1205 Geneva, Switzerland
[2]General Directorate of Mineral Research and Exploration of Turkey, Department of Mineral Research and Exploration, Ankara 06520, Turkey
[3]Institute of Earth Sciences, University of Lausanne, 1015 Lausanne, Switzerland

Abstract. The Eastern Pontides, Turkey host a diverse range of mineral deposits, including volcanogenic massive sulfide (VMS) and epithermal deposits. VMS deposits are predominantly hosted by the Late Cretaceous Kızılkaya Formation, whereas epithermal deposits are hosted by the Tirebolu Formation. Favorable host rocks for VMS deposits include felsic volcanic rocks, particularly rhyodacite of tholeiitic to calc-alkaline composition, whereas epithermal deposits are typically hosted by calc-alkaline to shoshonitic rhyolitic-dacitic lava flows. The switch from VMS to epithermal deposit formation coincides with the transition from the older Kızılkaya to the younger Tirebolu Formation (ca. 84-82Ma). The age of Late Cretaceous intrusive complexes hosting porphyry Cu-Mo deposits further coincides with the host rock age of epithermal deposits/occurrences. The switch in the orientation of Late Cretaceous dikes at the Yanıklı prospect documents a major rotation of the regional shortening axis at ~82Ma. The Eastern Pontides of Turkey are a significant metallogenic belt with a high potential for both VMS and epithermal deposits. Our new geochronological constraints provide fundamental insights about the formation and evolution of this metallogenic belt.

1 Introduction

The Eastern Pontides (EPs) orogenic belt is a remarkable segment of the Western Tethyan Metallogenic Belt, which hosts numerous mineral deposits, including porphyry Cu-Mo, precious metal epithermal, and volcanogenic massive sulfide (VMS) deposits. They occur in various regions within the EPs, including the Giresun, Ordu, and Artvin districts, and are associated with Late Cretaceous bimodal submarine magmatism (Aydin et al. 2020; Eyuboglu et al. 2014, 2021; Kandemir et al. 2019; Oğuz-Saka et al. 2023, Özdamar 2016). The boundaries between the different host rock formations are still uncertain within certain districts due to overlapping formation ages and variable geochemical signatures. Additionally, it is unclear which mineralization style is related to each formation, further contributing to the ongoing debate.

The aim of our study is to address the uncertainties related to mineral occurrences hosted by the Late Cretaceous bimodal submarine magmatic rocks in the Eastern Pontides. The current state of research on the mineral deposits of the region is presented in this study, along with a detailed description of the characteristics of the geological formations.

2 Late Cretaceous Magmatism in the Eastern Pontides

The Late Cretaceous volcanic rocks from the EPs are divided into four formations, which were formed during two different magmatic cycles (Aydin et al. 2020; Eyuboglu et al. 2021; Kandemir et al. 2019). Each cycle comprises a mafic and a felsic rock formation (Figure 1; Aydin et al. 2020; Eyuboglu et al. 2014, 2021; Kandemir et al. 2019; Oğuz-Saka et al. 2023). The lowermost formation of the first magmatic cycle is the Çatak Formation, which includes pillow basalt, basaltic-andesitic tuff and breccia, siltstone and marl alternations. $^{40}Ar/^{39}Ar$ dating of 92.1 Ma of the lower basaltic groundmass and planktonic foraminifera from pelagic limestone from the basal part of the Çatak Formation indicate an early/mid-Turonian–Santonian age (Kandemir et al. 2019). The overlaying late Turonian to early Santonian Kızılkaya Formation comprises dacitic and rhyodacitic domes and flows, along with intermediate andesitic stocks and dikes (Aydin et al. 2020; Eyuboglu et al. 2014, 2021; Kandemir et al. 2019). The mid-late Santonian-Campanian Çağlayan Formation of the second magmatic cycle, which consists of pillow basalt, basaltic-andesitic tuff and breccia, siltstone, and marl alternations, intrudes and overlays the Kızılkaya Formation in certain areas. Lastly, the youngest volcanic and volcaniclastic unit of the Cretaceous EPs is the Çayırbağ Formation of the second magmatic cycle, also known as the Tirebolu Formation, which is dominated by felsic volcanism (Aydin et al. 2020; Eyuboglu et al. 2014, 2021; Kandemir et al. 2019).

3 Settings of VMS Systems Hosted by Felsic Magmatic Rocks of the First Magmatic Cycle

The Kızılkaya Formation is composed of dacitic to rhyolitic rocks with varying tholeiitic to calc-alkaline compositions. The felsic rocks of the Kızılkaya Formation are favourable host rocks of VMS deposits in various regions, including Artvin, Rize, Giresun, etc (Figure 2).

In the Artvin District, Murgul, Hod Maden, and Kılıçkaya are major VMS deposits-occurrences hosted by the Kızılkaya Formation.

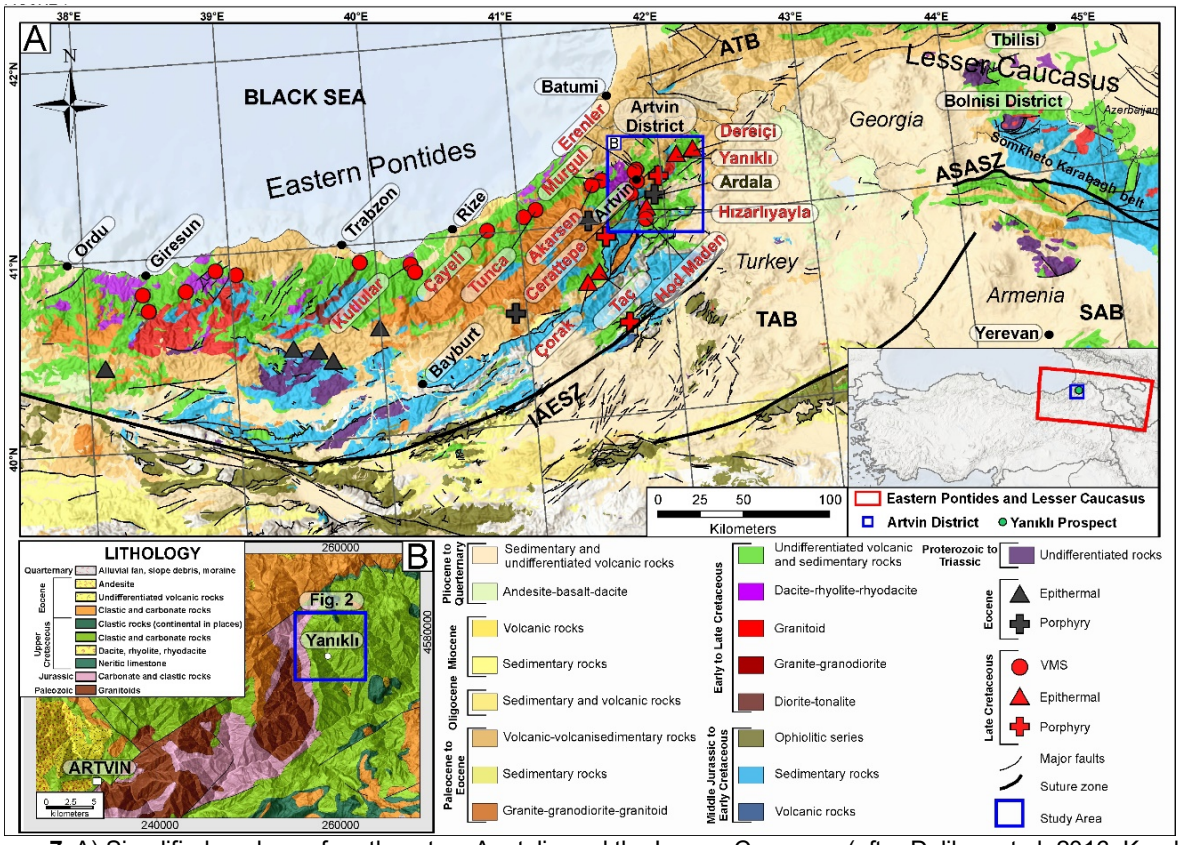

Figure 7. A) Simplified geology of northeastern Anatolia and the Lesser Caucasus (after Delibaş et al. 2016; Kandemir et al. 2019; Moritz et al. 2020). B) Geology of the Artvin District (simplified from the MTA 2002 1:500k geo map, Aydin et al. 2020). Abbreviations of tectonic zones and faults: ASASZ = Amasia-Sevan-Akera suture zone, ATB = Adjara-Trialeti belt, IAES = Izmir-Ankara-Erzincan suture, KB = Kapan block (Eurasian margin), SAB = South Armenian block, TAB Tauride-Anatolide block.

The felsic host rocks have been dated at 88.8 ± 0.9 Ma ($^{40}Ar/^{39}Ar$), and one unmineralized felsic rock has been dated at 86.51 ± 0.35 Ma (U-Pb) (Aydin et al. 2020; Bilir et al. 2022; Kandemir et al. 2019). Moreover, Rabayrol et al. (2023) reported an alteration age of the Taç prospect based on muscovite $^{40}Ar/^{39}Ar$ dating, which yielded an age of 86.3 ± 0.2 Ma.

The Tunca VMS occurrence located in the Rize region is hosted by a dacitic tuff breccia of the Kızılkaya Formation and U-Pb dating yielded an age of 88.1 ± 1.2 Ma (Revan et al. 2017). The Köprübaşı VMS occurrence related to the Kızılkaya Formation in the Giresun region is hosted by rocks dated at 91.1 ± 1.3 Ma and 82.6 ± 1 Ma (Eyuboglu et al. 2014). Furthermore, the host rocks of ore-bearing samples from the same region have yielded U-Pb concordia ages of 83.23 ± 0.21 Ma to 88.23 ± 0.37 Ma (Oğuz-Saka et al. 2023).

The ages of the host rocks of the VMS deposits indicate that they have been formed around 91-83 Ma. It is concluded that the Kızılkaya formation is a favourable host rock environment of the early magmatic cycle for VMS-style mineralization (Figure 2).

4 Late-stage Felsic Magmatic Rocks of the Second Magmatic Cycle As Hosts of Epithermal Polymetallic-Au Deposits and Occurrences

The Tirebolu Formation is the youngest event of felsic magmatism characterized by a calc-alkaline to shoshonitic composition. Within this formation, epithermal vein-type deposits are mainly associated with calc-alkaline rhyodacite volcanic rocks.

The Artvin District is a significant location for late epithermal ore formation, including Yanıklı (this study), Dereiçi (U-Pb; 79.2 ± 1 Ma), Hızarlı (U- Pb; 79.5 ± 1 Ma). The $^{40}Ar/^{39}Ar$ alteration age of the Çorak epithermal system from the Taç prospect is 82.2 ± 2 Ma (Rabayrol et al. 2023). Thus, Taç and Çorak are remarkable examples of epithermal deposits/occurrences that postdate the formation of VMS deposits (Figure 2).

The age interval of the Tirebolu Formation in the Giresun region has been defined by a U-Pb zircon concordia age of 82.19 ± 0.29 Ma and 80.96 ± 0.29 Ma (Oğuz-Saka et al. 2023). This geochemical and geochronological transition suggests a VMS-epithermal switch that coincides with the Kızılkaya and Tirebolu formation transition at ~84-82 Ma.

The age of the host rocks of epithermal occurrences also corresponds to the age of Late Cretaceous intrusive complexes hosting porphyry Cu-Mo deposits in the Eastern Pontides (Figure 2; Delibaş et al. 2016; Kuşcu et al. 2019; Rabyrol et al. 2023).

5 Implications From the Yanıklı Prospect, Artvin District

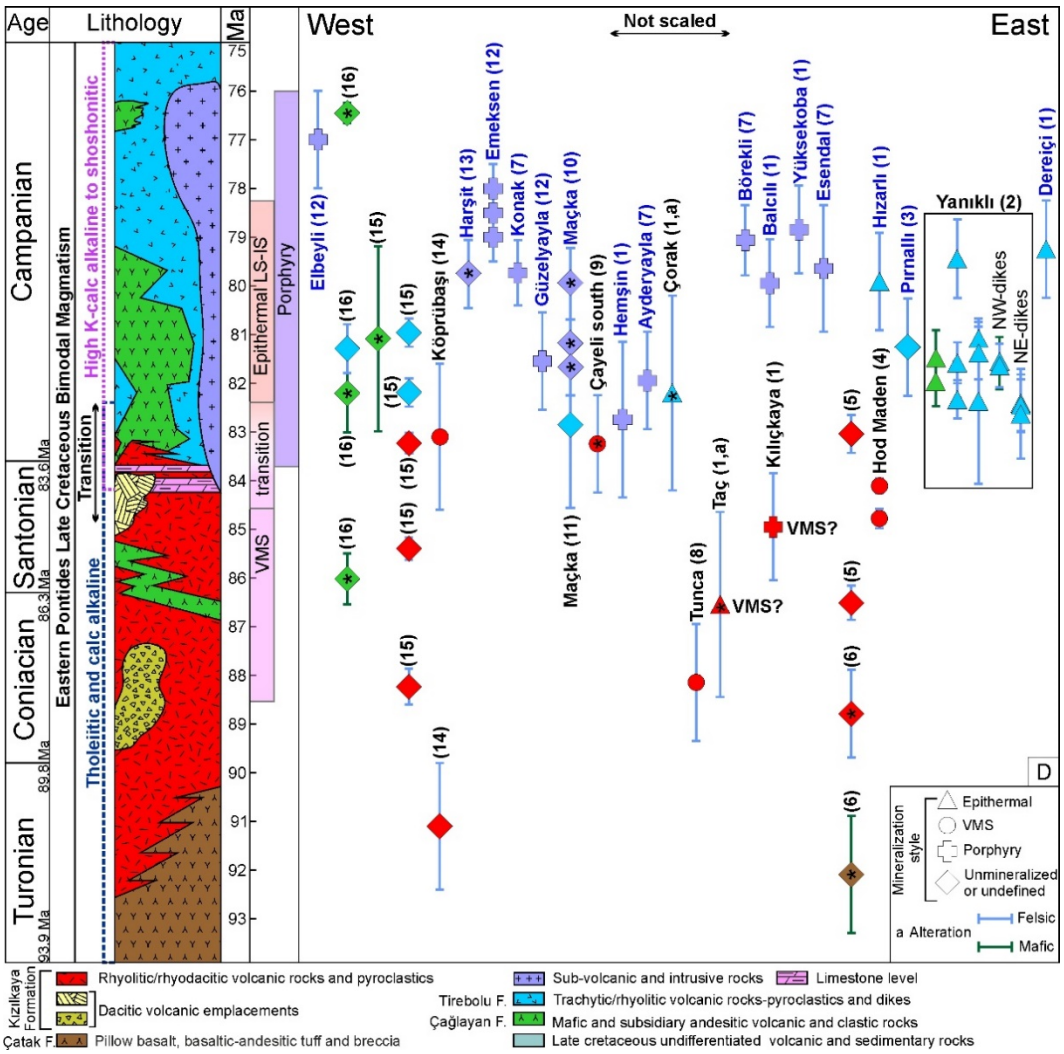

Figure 8. The distribution of well-known mineral occurrences in relation to the Late Cretaceous Eastern Pontides rock formations. All ages are U-Pb dates except where indicated by an asterisk (*), which represents $^{40}Ar/^{39}Ar$ dating. Late Cretaceous volcanic rocks (labelled in black) and plutonic rocks (labelled in blue) from the Eastern Pontides are as follows: (1) Rabayrol et al. (2023); (2) this study; (3) Karsli et al. (2012); (4) Bilir et al. (2022); (5) Aydin et al. (2020); (6) Kandemir et al. (2019); (7) Kuşcu et al. (2019); (8) Revan et al. (2017); (9) Alan et al. (2019); (10) Aydin (2014); (11) Eyuboglu et al. (2021); (12) Delibaş et al. (2016); (13) Karslı et al. (2010); (14) Eyuboglu et al. (2014); (15) Oğuz-Saka et al. (2023); and (16) Özdamar (2016). The host rocks of the VMS deposits/occurrences are constrained by the mid-Coniacian to late-Santonian tholeiitic to calc-alkaline felsic magmatism, whereas epithermal deposits/occurrences are constrained by late-Santionan to Campanian calc-alkaline to high-K calc-alkaline magmatism.

5.1 Lithogeochemistry and geochronology of felsic volcanic rocks at the Yanıklı Epithermal Prospect of the Artvin District

The Yanıklı epithermal prospect is located in the northeastern part of the Artvin District, ~30 km northeast of Artvin. Late Cretaceous felsic volcanic and volcaniclastic rocks host Zn-Pb-Cu-Au ore bodies, and have been affected by weak to pervasive hydrothermal alteration (Sönmez et al. 2022). The felsic rocks in Yanıklı are subdivided into four main units according to their age and composition, namely (i) feldspar porphyry dacite (KDa), (ii) fine-grained flow-banded rhyolite-rhyodacite (KRDa-1), (iii) flow banded-columnar rhyodacite-dacite (KRDa-2), and (iv) flow banded feldspar-rich rhyolite-rhyodacite (KRDa-3). The ages of the KRDa-1 and KRDa-2 units, which host epithermal mineralization, have been determined by U-Pb zircon dating. The KRDa-1 unit yielded a weighted mean age of 82.33 ± 0.39 Ma, whereas the KRDa-2 unit, which is affected by sericitic alteration, as well as weak pyrite ± sphalerite mineralization, yielded a younger weighted mean age of 81.58 ± 0.42 Ma. The adjacent KRDa-3 unit also yielded weighted $^{206}Pb/^{238}U$ mean ages ranging from 81.08 ± 0.34 to 82.37 ± 1.21 Ma. These ages provide important constraints on the age of the host rocks of epithermal ore bodies in the Yanıklı Prospect.

5.2 Dike orientations and local stress fields during the Late Cretaceous

During the Late Cretaceous, two generations of dikes with distinct orientations have been emplaced at the Yanıklı prospect. They include: the NE-trending KDike-1 unit and the NW-trending KDike-2 unit. The NE-oriented felsic dikes of the KDike-1 unit have yielded the oldest $^{206}Pb/^{238}U$ mean

crystallization ages, ranging from 82.41±0.59 Ma to 82.63±0.92 Ma. The younger generation of NW-trending dikes of the KDike-2 unit are predominantly composed of mafic rocks and have a weighted $^{206}Pb/^{238}U$ mean age of 81.64±0.45 Ma. These distinct dike orientations indicate that the main shortening axis (σ1) has rotated over time between the two dike generations. During the first generation of dike emplacement, the shortening orientation was NE-SW, and resulted in a NE-trending dike en-échelon pattern. The modification of the tectonic stress regime took place at ~82 Ma. The second dike generation was controlled by a NW-SE shortening axis and resulted in the emplacement of NW-oriented dikes.

6 Conclusions

The Eastern Pontides region is a major metallogenic belt, mainly characterized by VMS and epithermal systems. VMS deposits are mainly hosted by the Late Cretaceous Kızılkaya Formation, whereas the Tirebolu Formation hosts epithermal deposits. The ideal host rocks for VMS deposits are felsic volcanic rocks, particularly rhyodacite of tholeiitic to calc-alkaline composition, whereas epithermal deposits are typically hosted by calc-alkaline to shoshonitic rhyolitic-dacitic lava flows. The switch between the two distinct metallogenic regimes occurred concurrently with the transition from the older Kızılkaya to the younger Tirebolu Formation at ~84-82 Ma. This coincided with a rotation of the shortening axis from a NE-orientation to a NW-orientation, indicating a major change in the tectonic setting at the Yanıklı prospect.

Acknowledgements

The research was funded by the Swiss National Science Foundation through research grant 200021_188714. Additionally, Ş.U. Sönmez acknowledges the support of the Hugh McKinstry Fund, a student research grant program of the SEG Foundation of Canada. The authors would like to express their sincere gratitude to the General Directorate of Mineral Research and Exploration Turkey (MTA) for granting access to the Yanıklı prospect (project codes of 2019-2020-2021-32-13-06 and 2021-32-13-07), and to the exploration geologists of the MTA Eastern Black Sea District Office (S. Saka, C. Boysan, A. Ağan, and others) for their invaluable assistance and support throughout the project.

References

Alan İ, Balcı V, Keskin H, Altun İ et al (2019) Tectonostratigraphic characteristics of the area between Çayeli (Rize) and İspir (Erzurum). Bull. Miner. Res., 1-29.

Aydin F (2014) Geochronology, geochemistry, and petrogenesis of the Maçka subvolcanic intrusions: implications for the Late Cretaceous magmatic and geodynamic evolution of the eastern part of the Sakarya Zone, northeastern Turkey. Int Geol Rev 1246–1275.

Aydin F, Oğuz-Saka S, Şen C et al (2020) Temporal, geochemical and geodynamic evolution of the Late Cretaceous subduction zone volcanism in the eastern Sakarya Zone, NE Turkey: Implications for mantle-crust interaction in an arc setting. J Asian Earth Sci doi:https://doi.org/10.1016/j.jseaes.2019.104217

Bilir E, Kuşcu İ, Moritz R et al (2022) Hod Maden Deposit, Eastern Pontides, NE Turkey: A Cretaceous Au-rich VMS System - Geochemical and Isotopic Characterization of Hydrothermal Alteration and Mineralization. Sustainable Mineral Resources Supply: Challenges for Future Generations, (p. 5). Geneva.

Delibaş O, Moritz R, Ulianov A et al (2016) Cretaceous subduction-related magmatism and associated porphyry-type Cu–Mo prospects in the Eastern Pontides, Turkey: New constraints from geochronology and geochemistry. Lithos 248-251:119–137.

Eyuboglu Y, Dudás F, Zhu D et al (2021) Late Cretaceous alkaline magmas of the Eastern Pontides Orogenic Belt (NE Turkey): A review with new geological, geochemical and geochronological data. Gondwana Res 97:204–239.

Eyuboglu Y, Santosh M, Yi K et al (2014) The Eastern Black Sea-type volcanogenic massive sulfide deposits: Geochemistry, zircon U–Pb geochronology and an overview of the geodynamics of ore genesis. Ore Geol Rev 59:29-54.

Kandemir Ö, Akbayram K, Çobankaya M et al (2019) From arc evolution to arc-continent collision: Late Cretaceous–middle Eocene geology of the Eastern Pontides, northeastern Turkey. GSA Bulletin 131:1889-1906.

Karsli O, Caran Ş, Dokuz A et al (2012) A-type granitoids from the Eastern Pontides, NE Turkey: Records for generation of hybrid A-type rocks in a subduction-related environment. Tectonophysics 530-531:208-224.

Karsli O, Dokuz A, Uysal İ et al (2010) Relative contributions of crust and mantle to generation of Campanian high-K calc-alkaline I-type granitoids in a subduction setting, with special reference to the Harşit Pluton, Eastern Turkey. Contrib to Mineral Petrol 160:467–487.

Kuscu , Tosdal R, Kuscu G (2019) Episodic porphyry Cu (-Mo-Au) formation and associated magmatic evolution in Turkish Tethyan collage. Ore Geol Rev 107: 119-154.

Moritz R, Popkhadze N, Hässig et al (2020). At the crossroads of the Lesser Caucasus and the Eastern Pontides: Late Cretaceous to early Eocene magmatic and geodynamic evolution of the Bolnisi district, Georgia. Lithos, 378-379.

Oğuz-Saka S, Aydin F, Karsli O et al (2023) Two-stage bimodal volcanism in a Late Cretaceous arc/back-arc setting, NE Turkey: constraints from volcano-stratigraphy, zircon U-Pb and $^{40}Ar/^{39}Ar$ geochronology and whole-rock elemental and Sr-Nd-Pb isotope geochemistry. Lithos 440-441:107018.

Özdamar Ş (2016) Geochemistry and geochronology of late Mesozoic volcanic rocks in the northern part of the Eastern Pontide Orogenic Belt (NE Turkey): Implications for the closure of the Neotethys Ocean. Lithos, 240-256.

Rabayrol F, Wainwright A, Lee R et al (2022) District-Scale VMS to Porphyry-Epithermal Transitions in Subduction to Postcollisional Tectonic Environments: The Artvin Au-Cu District and the Hod Gold Corridor, Eastern Pontides Belt, Turkey. Econ Geol. doi:https://doi.org/10.5382/econgeo.4983

Revan M, Hisatani K, Miyamoto, H et al (2017) Geology, U-Pb geochronology, and stable isotope geochemistry of the Tunca semi-massive sulfide mineralization, Black Sea region, NE Turkey: Implications for ore genesis. Ore Geol Rev 89:369-389.

Sönmez ŞU, Moritz R, Turlin F et al (2022) Age and composition of magmatic rocks, and hydrothermal alteration characteristics of the Yanıklı Prospect, Eastern Pontides, Turkey. Sustainable Mineral Resources Supply: Challenges for Future Generations, (p. 48). Geneva.

Pb-containing aluminium phosphate-sulphate mineralization from the advanced argillic alteration in the Chelopech epithermal high-sulphidation Cu-Au deposit

Sylvina Georgieva[1], Elitsa Stefanova[1], Atanas Hikov[1], Milen Kadiyski[2], Stoyan Georgiev[1], Mariana Trifonova[3]
[1] *Geological Institute, Bulgarian Academy of Sciences, Sofia, Bulgaria*
[2] *Aurubis Bulgaria AD, Pirdop, Bulgaria*
[3] *Dundee Precious Metals Chelopech EAD, Bulgaria*

Abstract. The Chelopech epithermal high-sulphidation Cu-Au deposit is one of the significant and well described deposits in Europe. Its hydrothermal advanced-argillic alteration footprint extensively developed in depth is very suitable for exploring potential geochemical vectoring and indicators. Alunite and aluminum-phosphate-sulphate (APS) minerals are common in the advanced argillic alteration zone of the deposit. Although these minerals are formed along with similar mineral association (quartz, dickite/kaolinite, barite, ore mineralization) they reveal different geochemical properties across the altered rock volume and with distance to the ore bodies and the depth. The studied APS mineralization is established westwards from the ore block 151, level 400, westernmost part of the deposit. It chemical composition refers to woodhouseite-svanbergite- hinsdalite solid solution with Ca- to Sr-rich and Pb-rich varieties without reaching pure end-member. The main peculiarity of the APS from the distal zones compared to the previous published data about APS from the deposit, found in the frame of the ore bodies and in depth (>1300 m) is the remarkable enrichment of Pb content up to 15 wt% PbO. The geochemical signatures of the APS as members of the alunite supergroup could have a potential to be used as directional indicators towards the orebody after careful consideration.

1 Introduction

The aluminium phosphate-sulphate minerals (APS) belong to the alunite supergroup that consists of three mineral groups. The supergroup contains more than 40 mineral species with general formula $DG_3(TO_4)_2(OH,H_2O)_6$, where D is a large cation (Na, K, Ag, NH_4, Pb, Ca, Ba, Sr, REE, U), G is occupied by Al, Fe, Cu or Zn in octahedral coordination, and T is dominated by P, S and As in tetrahedral coordination (Jambor 1999; Dill 2001). These minerals typically occur in advanced argillic style acidic and intermediate pyroclastic, volcanic and subvolcanic rocks related or not to ore mineralization. Such relations have been documented in a large number of epithermal high-sulphidation ore deposits. The geochemical peculiarities of alunite and APS minerals have recently become an object of interest for the exploration in terms to evaluate the distance to the intrusive centre or to distinguish mineralized from barren systems (e.g., Chang et al 2011). APS mineralization (svanbergite-woodhouseite, florencite and crandallite) are broadly established in the advanced argillic alteration of the Chelopech deposit in close proximity to the ore bodies. The mineralization is developed down to a depth of >1300 m (Georgieva et al 2002; Georgieva and Velinova 2014). This report provides new data about Pb-containing APS minerals established in the advanced argillic alteration from the western part of the Chelopech deposit in drill-hole samples, traced westwards and distant from the economically outlined ore bodies.

2 Methodology

Materials used in this study are hydrothermally altered in advanced argillic alteration granodiorite samples from the EXT151-400-19 drill-core, mine level 400, western part of the Chelopech deposit The drill-hole starts from the western peripheral part of the ore-block 151, and shifts outwards of the ore-block to the west. Prior to SEM-EDS chemical study, the mineral composition and relationships in the rocks were examined in thin sections using optical and scanning-electron microscopy.

A VEGA 3 XMU SEM by Tescan at Aurubis Bulgaria AD was used for BSE imaging and determination of major element composition of minerals with EDS. We used a 20 kV accelerating voltage; beam calibration was done using pure copper. The formulae units were calculated based on the assumption that P+S is 2 *apfu* (Jambor 1999).

3 Geological setting

The Chelopech high-sulphidation epithermal Cu-Au deposit is ranked among the most significant European Cu-Au deposits. As part of the Elatsite-Chelopech ore field, it is situated in the northern part of the Panagyurishte ore region within the central parts of the Srednogorie tectonic zone. The Panagyurichte ore region is characterized with the presence of a cluster of porphyry Cu (e.g., Elatsite, Assarel, Medet) and epithermal Cu-Au (e.g., Chelopech, Elshitsa, Radka) deposits.

The ore mineralization of the Chelopech deposit is hosted in an Upper Cretaceous volcanic and volcano-sedimentary complex (Popov et al. 1983), transgressively overlaying gneisses, amphibolites, schists and phyllites of Neoproterozoic to Paleozoic

age (Peytcheva and von Quadt 2004; Carrigan et al. 2006). The Upper Cretaceous volcanic complex consists mainly of intermediate-composition varieties (andesitic, trachydacitic to dacitic) of Turonian age (Stoykov et al. 2004). Recently, Marton et al (2016) proposed a new geological model with a shallow multiphase intrusive complex intersected by vertically extended, intrusion-related breccia bodies with at least one maar-diatreme eruptive centre. The diatreme is related to a granodiorite phase associated with: 1) porphyry Cu-Mo-Au stockwork in the Petrovden area; 2) distal base metal sulphide veins in the Petrovden and Vozdol areas; 3) high-sulphidation Cu-Au mineralization in the Chelopech and Sharlo Dere areas.

Larg parts of the rocks in the vicinity of the Chelopech deposit are overprinted by extensive hydrothermal alteration. The ore mineralization is generally associated with a vast zone of advanced argillic alteration surrounded by halos of quartz-sericitic and propylitic alteration (Georgieva 2017). The economic Cu-Au mineralization is most strongly developed in the volcanic breccia and/or along fractures and represents massive to stockwork bodies, veins and disseminations. Enargite, lusonite, tennantite, chalcopyrite and bornite are the main sulphides and sulphosalts in the ore mineralization along with abundant subordinate and sporadic minerals including tellurides and selenides (Terziev 1968; Petrunov 1995).

4 Results

The studied APS mineralization occurs in the advanced argillic altered granodiorites established westwards from the ore block 151, level 400, westernmost part of the deposit. Besides the intensive alteration, the granodiorites are cut by up to 1 cm wide pyrite veins and late enargite-tennantite nests and veinlets. Along with enargite and tennantite weak mineralization of chalcopyrite, bornite, goldfieldite, tetrahedrite, galena and clausthalite are established. As a gangue mineralization bladed sub- to euhedral barite crystals up to 3 mm occur. Commonly, the APS mineralization is developed as up to 200 μm sub- to euhedral crystals in association with abundant quartz, clay minerals (dickite/kaolinite), barite and disseminated pyrite. Generally, they intergrowth with barite and dickite/kaolinite. Euhedral crystals up to 100 μm can occur as inclusions in ore minerals including enargite and tennantite. The cores of certain APS grains and crystals are replaced by clay minerals (dickite/kaolinite). Clear chemical zoning in the majority of the studied crystals are observed in back-scattered electron (BSE) images (Fig. 1).

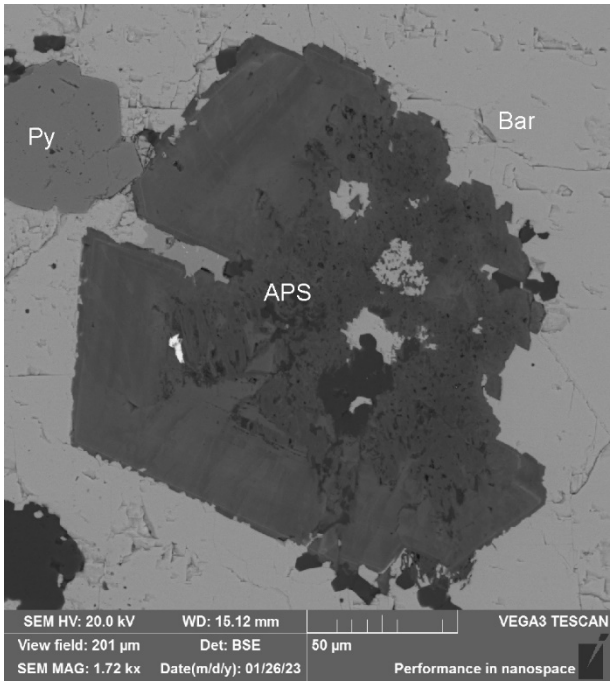

Figure 1. BSE image of zonal APS crystal in barite. Abbreviations: Py – pyrite; Bar - barite

The chemical SEM-EDS analyses reveal that the APS minerals belong mainly to the woodhouseite-svanbergite-hinsdalite solid solution series: $(Ca,Sr,Pb)Al_3(PO_4,SO_4)_2(OH,H_2O)_6$. Their composition ranges from Ca- to Sr-rich and Pb-rich phases without reaching the pure end-members (Fig. 2A). In addition, minor amounts of Ba (Fig. 2B) and LREE are also established. The chemical zoning observed in BSE images is mainly due to variations of Ca, Sr, Pb and Ba contents in *D* crystal structure site. The maximum CaO content is up to 10.3 wt%, SrO - up to 12.3 wt%, PbO – up to 15 wt%. Low contents of K_2O and Na_2O exist in some of the samples. The *G* site is mostly occupied by Al – up to 38.87 wt% Al_2O_3, small amount of Cu - up to 4.57 wt% CuO and Fe - up to 1.87 wt% Fe_2O_3. The phosphorus/sulphur molar ratio from *T* site is close to a 1:1 (Fig. 2C) in the predominant number of analyses. In some analytical points the ratio is more than 3:1. Regarding the Ca-rich varieties compositions close to woodhouseite (with P:S = 1:1) and crandallite (P:S > 3:1) are established.

Our preliminary observations show that the cores of APS crystals have higher Ca and P contents while the peripheries are enriched in Pb. The elevated Ca and P contents in the cores could be explained by apatite dissolution and replacement in acid environment of advanced argillic alteration (Stoffregen 1987; Georgieva and Velinova 2014).

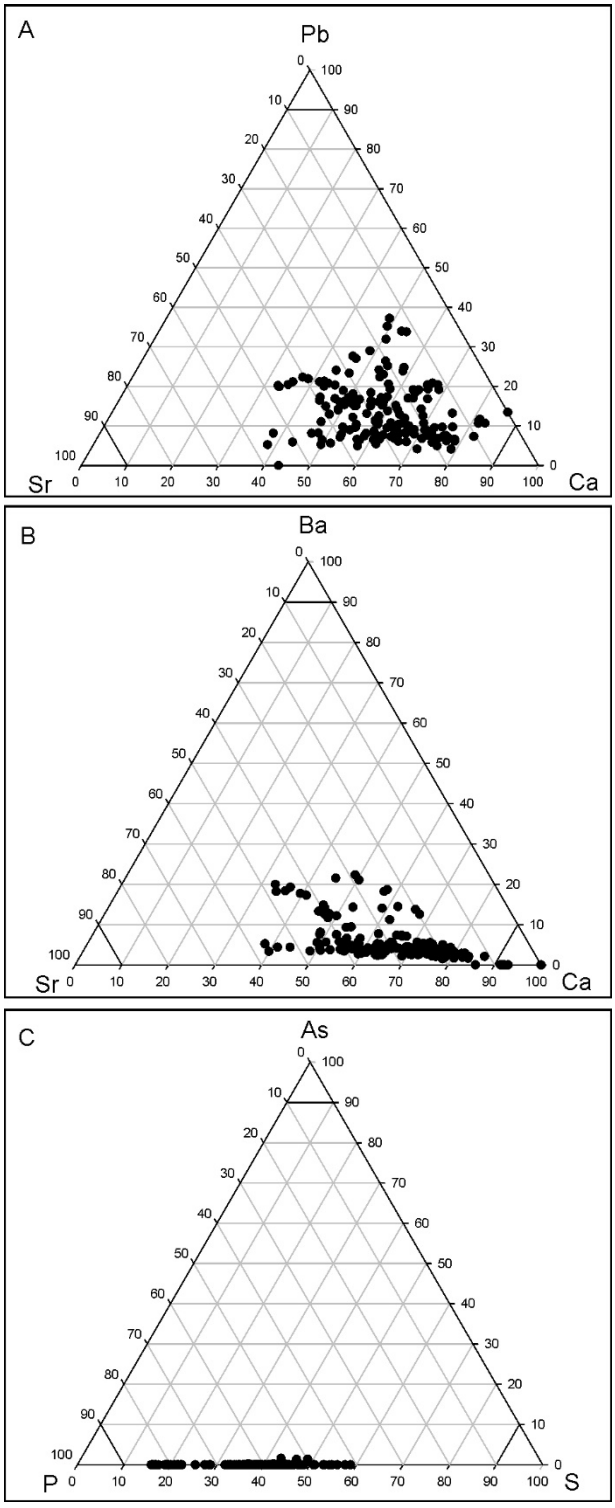

Figure 2. A, B) Cation compositions in the *D* sites of zonal APS; C) Anion composition in the *T* sites of APS

5 Discussion and concluding remarks

The studied APS mineralization is located in the westernmost part of the Chelopech Cu-Au deposit, i.e., in a distal position to the orebody. It has similar occurrence and mineral association compared to the previously studied APS mineralization from the ore blocks at level 405 and from the deep drill-holes 600 and 600a (>1300 m depth). The APS from these localities belong to the svanbergite, woodhouseite, svanbergite-woodhouseite solid solution series from high Ca- to high Sr-varieties with minor amounts of Ba and K. Florencite $(Ce,La,Nd)Al_3(PO_4)_2(OH)_6$ and crandallite $(CaAl_3(PO_4)_2(OH)_5.H_2O)$ as end members are also established (Georgieva et al 2002; Georgieva and Velinova 2014). The main difference between APS minerals from the different localities is their chemistry. The APS mineralization located in a distal position to the orebodies are remarkably enriched in Pb. The chemical composition of the APS reveal Ca, Sr and Pb as main constituents along with less Ba, LREE, K, and Na. This Pb-containing APS mineralization refer to the alunite supergroup with woodhouseite- svanbergite-hinsdalite composition from Ca- to Sr-rich and Pb-rich varieties without reaching pure end-members.

Chang et al (2011) also determined variable Pb-content in alunite from the Mankayan mineral district, Philippines. According to the authors the Pb content in alunite increase with increasing distance from the intrusive center causing the ore mineralization. Our preliminary data are in agreement with the observation of Chang et al (2011) and show Pb-rich APS minerals in a distal parts of the deposit. This suggest that the increased Pb content in the APS could also be considered as a similar directional indicator though further examinations are needed.

Acknowledgements

The study is financially supported by the Bulgarian National Science Fund KP-06-N44/4, 12.2020 project.

References

Carrigan C, Mukasa S, Haydutov I, Kolcheva K. (2006) Neoproterozoic magmatism and Carboniferous high-grade metamorphism in the Sredna Gora Zone, Bulgaria: An extension of the Gondwana-derived Avalonian-Cadomian belt?. Precambrian Res 147(3–4): 404–416. https:// doi.org/10.1016/j.precamres.2006.01.026

Chang Z, Hedenquist JW, White NC, Cooke DR, Roach M, Deyell CL, Garcia J, Gemmell JB, McKnight S, Cuison AL (2011) Exploration Tools for Linked Porphyry and Epithermal Deposits: Example from the Mankayan Intrusion-Centered Cu-Au District, Luzon, Philippines. Econ Geol 106(8): 1365–1398. https://doi.org/10.2113/econgeo.106.8.1365

Dill HG (2001) The geology of aluminium phosphates and sulphates of the alunite group minerals: A review. Earth Sci Rev 53: 35–93.

Georgieva S (2017) Mineral association and their distribution in hydrothermal alteration zones of the Chelopech high-sulphidation deposit, Bulgaria. Geol Balc 46(2): 11–16.

Georgieva S, Velinova N (2014) Florencite-(Ce, La, Nd) and crandallite from the advanced argillic alteration in the Chelopech high-sulphidation epithermal Cu-Au deposit, Bulgaria. Compt Rend Acad Bulg Sci 67(12): 1669–1678.

Georgieva S, Velinova N, Petrunov R, Moritz R, Chambefort I, (2002) Aluminium phosphate-sulphate minerals in the Chelopech Cu-Au deposit: spatial development, chemistry and genetic significance. Geochem Miner Petr 39: 39–53.

Jambor JL (1999) Nomenclature of the alunite supergroup. Canad Mineral 37: 1323–1341.
Marton I, Dintchev Y, Trifonova M, Hadzhieva N, Grigorova M et al (2016) A new geological model for the Chelopech Au-Cu deposit in Bulgaria: exploring a maar-diatreme system within an intrusive environment. In: SEG-MJD 2016 Conf. (electronic abstracts).
Petrunov R (1995) Ore mineral paragenesis and zoning in the deposit of Chelopech. Geochem Mineral Petrol 30: 89–98 (in Bulgarian, with English abstract).
Peytcheva I, von Quadt A (2004) The Palaeozoic protoliths of Central Srednogorie, Bulgaria: records in zircons from basement rocks and Cretaceous magmatites. Proceedings of the Fifth International Symposium on the Eastern Mediterranean Geology, 14–20 April 2004, Thessaloniki, Greece, 392–395.
Popov P, Vladimirov V, Bakardjiev S (1983) Structural model of the polyformational Chelopech copper field (Bulgaria). Geol Rud Mestorojd 25(5): 3–11 (in Russian).
Stoffregen RE, Alpers CN (1987) Woodhouseite and svanbergite in hydrothermal ore deposits: products of apatite destruction during advanced argillic alteration. Canad Mineral 25: 201–211.
Stoykov S, Peytcheva I, von Quadt A, Moritz R, Frank M, Fontignie D (2004) Timing and magma evolution of the Chelopech volcanic complex (Bulgaria). Schweiz Mineral Petrogr Mitt 84: 101–117.
Terziev G (1968) Mineral composition and genesis of the Chelopech ore deposit. Bull Geol Inst, series Geochem Mineral Petrogr 17: 123–187 (in Bulgarian, with English abstract)

Metal Endowment of Magmatic Brines from Active Geothermal Reservoirs

Brian Tattitch[1], Jon Blundy[2], Oscar Laurent[3,4]
[1]*University of Western Australia, Perth, Australia*
[2]*University of Oxford, Oxford, United Kingdom*
[3]*CNRS-Géosciences Environnement Toulouse, France*
[4]*Institute of Geochemistry and Petrology, Department of Earth Sciences, ETH Zurich, Zurich, Switzerland*

Abstract. Exploration for efficient clean geothermal power is targeting ever deeper "supercritical" geothermal reservoirs. Many supercritical reservoirs are accumulations of high-temperature magmatic fluids. Unlike heated meteoric water, these saline fluids and hypersaline brines contain significant endowments of critical elements. To quantify these endowments we examined brine inclusions from 3 active geothermal systems (Kakkonda, Japan; Larderello, Italy; Muara Laboh, Indonesia) and deep samples from 2 active volcanoes (Soufriere Hills Volcano, Montserrat; Ascension Island Volcano, mid-Atlantic). The brines recovered from these systems are extremely salty, (TDS > 50wt% $NaCl_{eq}$). The highest temperature inclusions show maximum trapping temperatures > 500°C. Maximum concentrations of selected elements are: 0.27% Sr and 3 ppm Au (Larderello); 2.7% Mn, 0.9% Zn, 0.7% Cu, 0.3% Pb (Kakkonda); 0.2wt% Cu (Muara Laboh); 0.5% B, 900 ppm Ba, 500 ppm Li and 90 ppm Ag (Montserrat); 0.19% Rb, 350 ppm Mo, 180 ppm W and 4 ppm Au (Ascension). We will show how these brines fit into a broader picture of ancient ore fluids, and modern geothermal systems. Our data also suggest that recovery of these critical elements could provide additional economic value to geothermal production and some systems could become a new versatile economic resource in their own right.

1 Introduction

It has been well established that the solubility of many critical metals relies on the presence of abundant carrier anions, or ligands to stabilize large, dissolved concentrations of metals at high temperature. In magmatic environments saline fluids are responsible for concentrating and transporting a huge range of ore metals from their parental magmas to the site of ore deposition (e.g. Candela and Holland 1984, Kouzmanov and Pokrovski 2012, Tattitch and Blundy 2017). There is strong evidence that these types of saline magmatic fluids were not unique to systems leading to ore deposition, but rather that many shallow evolved magmatic systems (e.g. granitic intrusions and arc volcanoes) commonly degas fluids rich in metals (e.g. Audetat et al. 2008, Edmonds et al. 2018).

However, the hypersaline metalliferous brines observed at depth in granites and ore deposits are not the same as the volcanic emissions observed at the surface today. Volcanic fumaroles do retain an imprint of the metal-rich nature of their generation, but only transport a tiny fraction of the metal endowment initial imparted when they were degassed from deep magma reservoirs. This is because when saline fluids ascend away from the magmatic hearth, they cannot retain their entire metal-chloride load. As they ascend at high-temperature the decompression inescapably leads to the formation of metal-rich hypersaline brine as the metal-Cl solubility in the ascending vapor decreases. The textural association of these two fluids in magmatic systems (e.g. Fournier 1999) and more recent numerical modelling of magmatic degassing (Afanasyev et al. 2018) both show that the hypersaline brine formed during decompression is commonly left behind, accumulating at depth, while the low-density metal-poor vapor is released; it is this metal-poor vapor that feeds volcanic fumaroles in active volcanoes.

While there is abundant evidence from volcanic monitoring that magmatic vapors contain magmatic derived metals, this only provides a window into the modern geothermal brine reservoirs left behind at depth. To understand the endowment of modern brine reservoirs we need to examine them directly. Our early investigation of modern brine reservoirs (Blundy et al. 2021) revealed that these brines are significantly enriched in base metals (Cu, Zn, Pb) similar to brines associated with porphyry ore deposits. These data show that the base metal concentration in the cooling brines is likely limited by sulfide solubility, fractionating Cu from the more soluble Zn and Pb. Linking the brine trace data to models for brine lens generation shows that protracted periods of degassing and brine accumulation will lead to either a substantial soluble Cu reservoir, or substantial Cu-sulfide deposition dependant on the availability of reduced sulfur (Blundy et al. 2021). Nonetheless, drilling deep hot brine wells, maintaining well integrity and preventing unwanted scaling prior to metal recovery pose significant challenges for exploiting these brines for metals or energy. To overcome these challenges and evaluate the economic potential of these brines we need a more complete understanding of their composition and distribution.

Here we will present a greatly expanded modern brine dataset with all major salts and 14 key trace metals and trace elements. Our expanded dataset shows that hypersaline modern brines from around the world are commonly more enriched in critical metals than geothermal fluids or other brines utilized for metal production (e.g. Harto 2013) and more have an even larger and more versatile potential metal endowment than reported previously (Blundy et al. 2021).

2 Methods

Here we present evidence of the presence of metal-rich hypersaline magmatic brines in 3 active geothermal reservoirs (Kakkonda, Japan, Larderello, Italy, Muara Laboh, Indonesia) and 2 active volcanoes (Soufriere Hills Volcano, Montserrat and Ascension Island Volcano, mid-Atlantic) (Figure 1). These sites were chosen because at each site there was already an indication of conductive saline fluids at depth (Rizzo et al. 2022, Uchida et al. 2000, Dyaksa et al. 2016, Ryan et al. 2013), or shallow magma in the case of Ascension Island (Chamberlain et al. 2016)

Figure 1: Map of Sample Locations for Active Hydrothermal Systems Containing Deep Hypersaline Brines

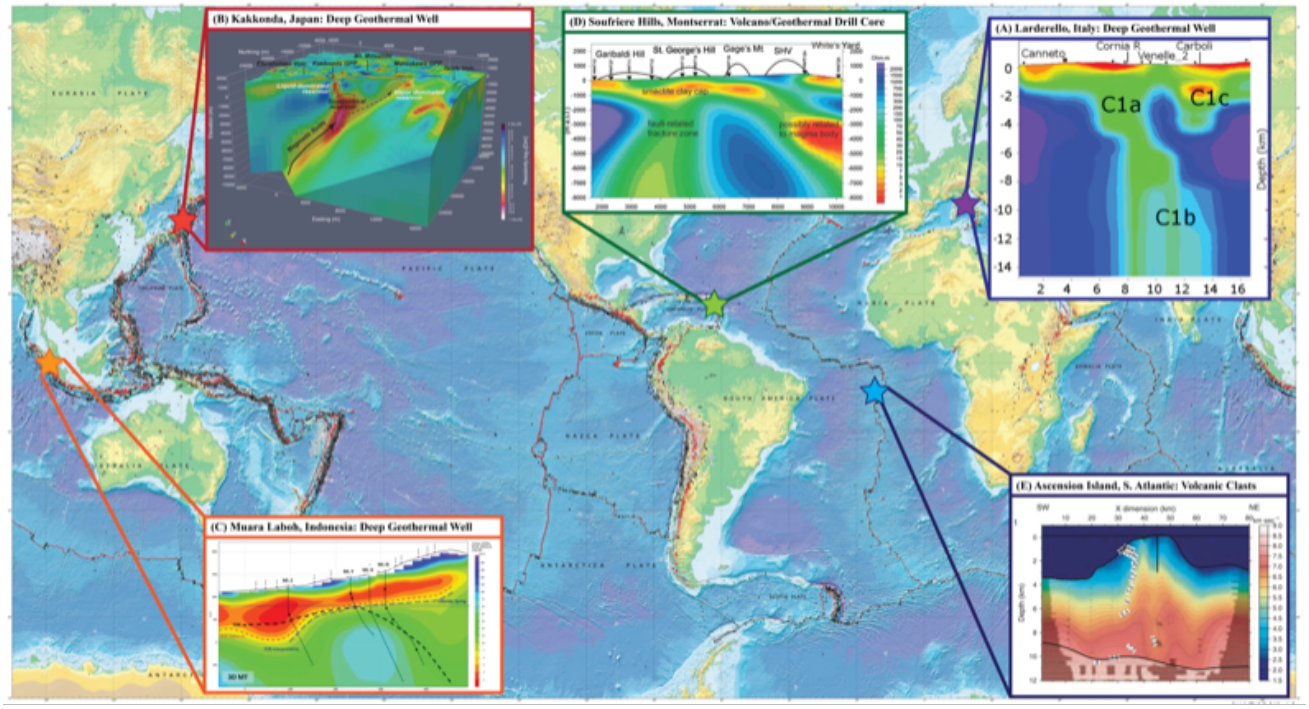

Figure 1. World map (Base map USGS I-2800) showing the sample locations of the 5 sites examined for evidence of metalliferous hypersaline brine in deep geothermal reservoirs. Electrical conductivity surveys, highlighting conductive fluids at depth are shown for sites (A) Larderello, (B) Kakkonda, (C) Muara Laboh, and (D) Montserrat, along with a seismic survey of site (E) Ascension Island, showing magma at depth.

2.1 Fluid inclusion Analyses

We obtained deep drill core samples from the 3 intrusive magmatic geothermal systems (Kakkonda- well WD-1a, Larderello- wells Travale-1s and Radicondoli-26, Muara Laboh- well H4) along with drill core samples from the exploratory well from Soufriere Hills Volcano (SVH) on Montserrat. From the geothermal sites we recovered several generations of quartz veins to search for hypersaline brine fluid inclusions. No quartz veins were present in the drill core from Montserrat. As a result, we recovered several "micro-miarolitic" cavities from the Montserrat drill core filled with hydrothermal quartz.

No drill core material is available from Ascension Island. However, volcanic clasts recovered from the island occasionally contain fragments of granitic material from the roots of the volcano. We extracted grains of magmatic quartz and sanidine from these granitic clasts to search for brine inclusions. Figure 2 shows photo-micrographs of typical brine fluid inclusions recovered from each of these 5 sites.

Each inclusion assemblage was examined using a Linkam XY1400 stage to determine the dissolution temperature for the halite daughter minerals (T_m^{Halite}), as well as the contraction vapor bubble (T_m^{L-V}). Upon dissolution of both phases the inclusions were considered homogenized back to their original single brine liquid composition (T_h).

2.2 LA-ICPMS Analyses

Inclusion assemblages with a significant number of brine inclusions of sufficient size (>15 μm) were selected for ICPMS analysis using a quadrupole mass spectrometer and a custom 193 nm laser system at ETH Zurich. We examined both major (Na, K, Ca, Fe, Mn) and trace element (Li, Cu, Zn, As, Mo, Ag, Sb, W, Au, Pb, B, Rb, Sr, Ba) abundances in the inclusions standardized to a total salinity determined by microthermometry. Spot size in increased stepwise until ablating the entire inclusion. Transient signals from the ICPMS were integrated in SILLS (Guillong et al. 2008) to quantify the concentration of all the elements of interest for each inclusion. Brine compositions will then be reported as averages for each of the samples once inclusion signals are screened for any irregularities (missing salt signals, major elements below LOD).

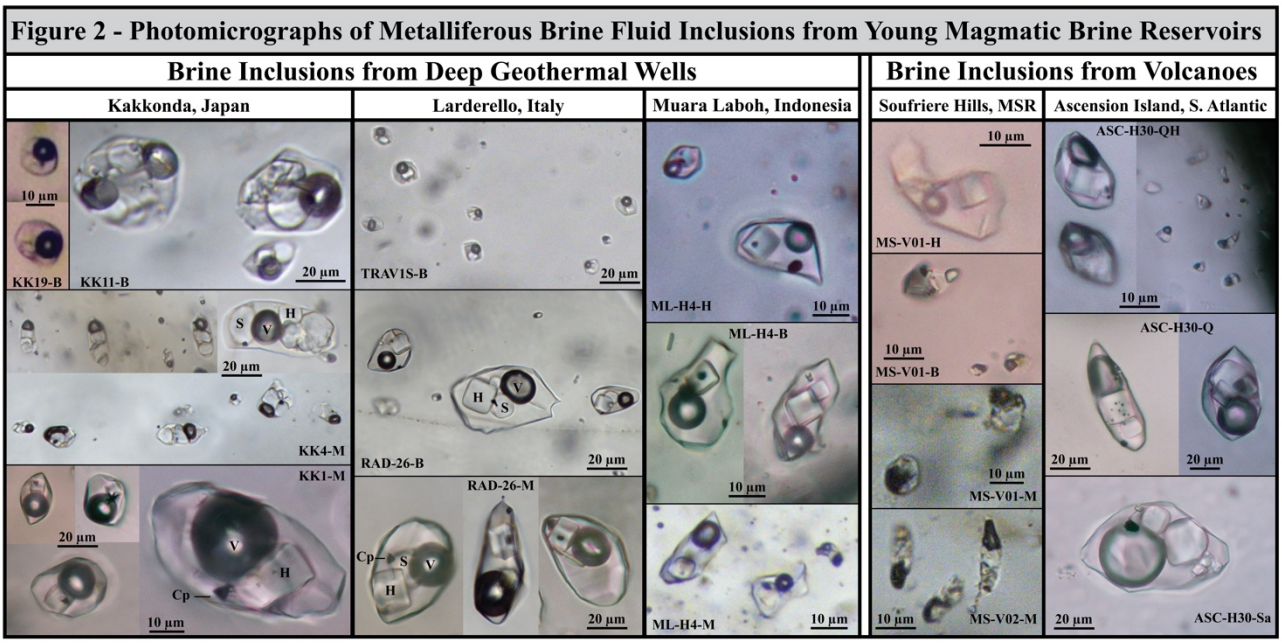

Figure 2. Photo-micrographs of brine fluid inclusions from each of the 5 geothermal/volcanic sites examined. Inclusions all show at least one halite daughter mineral along with a contraction vapor bubble formed on cooling to room temperature. Many of the inclusions also contain opaque daughter minerals formed from mixtures of oxide and sulfide, again formed upon cooling the metal-rich brine inclusions. Homogenization of these inclusions back to a single liquid phase was used to determine the salinity and trapping temperature of the inclusions.

3 Results

Histograms showing the ranges of T_m^{Halite} and $T_m^{L\text{-}V}$ for each of the samples examined from each of the 5 sites are shown in Figure 3. Microthermometry data shows that the brines in these systems are truly hypersaline and have a salinity in excess of >50wt% $NaCl_{eq}$ for nearly all samples. The highest temperature brines also have trapping temperatures (preserved as T_h) in excess of 500ºC. These high temperatures are consistent with the magmatic origin of the saline fluids that formed these brine reservoirs at depth.

We will present complete LA-ICPMS analyses of the entire brine sample suite at the SGA meeting. The highest concentrations for some selected elements include: 0.27% Sr and 3 ppm Au (Larderello); 2.7% Mn, 0.9% Zn, 0.7% Cu, 0.3% Pb (Kakkonda); 0.2wt% Cu (Muara Laboh); 0.5% B, 900 ppm Ba, 500 ppm Li and 90 ppm Ag (Montserrat); 0.19% Rb, 350 ppm Mo, 180 ppm W and 4 ppm Au (Ascension). This expanded dataset confirmed the previous observation that the modern magmatic brine reservoirs examined are well endowed with base metals (Blundy et al. 2021) similar to brines recovered from ore veins in arc magmatic-hydrothermal deposits (Kouzmanov and Pokrovski 2012). However, our data shows that these brines are endowed with much more than base metals.

The complete sample suite will also be compared to a database of analyses from ancient brine ore fluids and granite-hosted brine inclusions as well as deep geothermal brines and dilute geothermal waters. We will discuss how our data highlights that modern brines are very similar to the ore fluids that formed ore deposits in the past. Characterizing these brines can provide valuable information about the nature of magmatic brines that can lead to ore formation without the challenges of resetting inclusions and overprinting that are common in ancient ore systems. They can provide information about high-temperature alteration, ore mineral solubility, and the extent of brine reservoirs above intrusions. All of these aspects of modern brine lenses can provide new insights into the nature of magmatic hydrothermal ore deposition.

Yet, understanding these high-temperature brines can also help with developing new models for supercritical geothermal wells, or developing new materials to allow for protracted exposure of wells to corrosive supercritical fluids near these brines, or perhaps exposure to the brines themselves. Yet, our data show that these brines are also much more endowed in critical metals and other valuable elements than any of the geothermal waters or brines currently exploited for metal recovery.

Finally, the large array of valuable elements dissolved in the brines represent a significant potential economic resource if they could be recovered. As such, deep magmatic brines could provide an entirely new way to secure some of these critical elements and magmatic brine reservoirs could become an economic resource in their own right. Each of these facets of the scientific and economic potential of brine lenses will also be discussed.

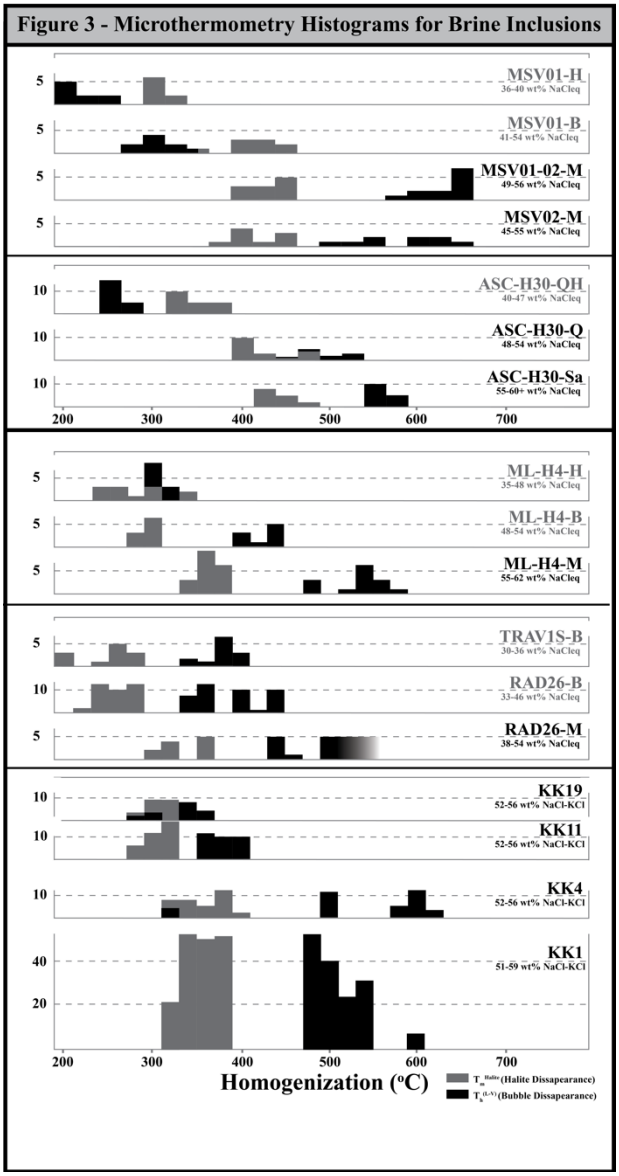

Figure 3. Histograms showing the ranges for T_m^{Halite} and $T_m^{L\text{-}V}$ for each of the brine sample sets examined in this study. Halite dissolution temperatures were used to determine the salinity of the brine inclusions. Most inclusions homogenized by bubble disappearance after halite dissolution and $T_m^{L\text{-}V}$ was then used to determine the trapping conditions for the brines.

Acknowledgements

We would like to acknowledge BHP for supporting this research project and ETH Zurich and Cyril Chelle-Michou for assistance with the LA-ICPMS analyses. We would also like to thank AIST and the Japanese Geologic Survey for providing access to the Kakkonda drill cores; Paolo Fulignati for drill core samples from Larderello; Jim Stimac for samples from Muara Laboh; The Montserrat Volcano Observatory, BGS and Adam Stinton for samples from the SHV; and Chris Harris for samples from Ascension Island.

References

Afanasyev A., Blundy J., Melnik O. and Sparks S. (2018) Formation of magmatic brine lenses via focussed fluid-flow beneath volcanoes. *Earth Planet. Sci. Lett.* **486**, 119–128.

Audétat A., Pettke T., Heinrich C. A. and Bodnar R. J. (2008) Special Paper: The Composition of Magmatic-Hydrothermal Fluids in Barren and Mineralized Intrusions. *Econ. Geol.* **103**, 877–908.

Blundy J., Afanasyev A., Tattitch B., Sparks S., Melnik O., Utkin I., and Rust A. (2021) The economic potential of metalliferous sub-volcanic brines. *R. Soc. open sci*. 8

Candela P. A. and Holland H. D. (1984) The partitioning of copper and molybdenum between silicate melts and aqueous fluids. *Geochim. Cosmochim. Ac.* **48**, 373–380.

Chamberlain K.J., Barclay J., Preece K., Brown R.J., Davidson J.P., EIMF (2016) Origin and evolution of silicic magmas at ocean islands: Perspectives from a zoned fall deposit on Ascension Island, South Atlantic. J*ournal of Volcanology And Geothermal Research,* V. 327, pp 349-360

Harto, Christopher. *Argonne Geothermal Geochemical Database v2.0*. United States: N. p., 2013. Web. doi:10.15121/1149726.

Dyaksa D.A., Ramadhan I., Ganefianto N. (2016) Magnetotelluric Reliability for Exploration Drilling Stage: Study Cases in Muara Laboh and Rantau Dedap Geothermal Project, Sumatera, Indonesia. *Proceedings, 41st Workshop on Geothermal Reservoir Engineering.* Feb. 22-24

Edmonds M, Mather TA, Liu EJ. (2018) A distinct metal fingerprint in arc volcanic emissions. Nat. Geosci. 11, 790.

Fournier R. O. (1999) Hydrothermal processes related to movement of fluid from plastic into brittle rock in the magmatic-epithermal environment. *Econ. Geol.* **94**, 1193–1211.

Kouzmanov K. and Pokrovski G. S. (2012) Hydrothermal controls on metal distribution in porphyry Cu (-Mo-Au) systems. *Soc. Econ. Geol. Spec. Publ.* **16**, 573–618.

Guillong M., Meier D.L., Allan M.M., Heinrich C.A., and Yerdley B.W.D. (2008) Appendix A6: SILLS: A Matlab-based program for the reduction of laser ablation ICP-MS data of homogeneous materials and inclusions. *MAC Short Course 40: Laser-Ablation-ICP-MS in Earth Sciences: Current practices and outstanding issues.*

Rizzo E., Giampaolo V., Capozzoli L., De Martino G., Romano G., Santilano A., Manzella A. (2022) 3D deep geoelectrical exploration in the Larderello geothermal sites (Italy), *Physics of the Earth and Planetary Interiors*, V. 329–330

Ryan G.A., Peacock J.R., Shalev E., and Rugis J. (2013), Montserrat geothermal system: A 3D conceptual model, *Geophys. Res. Lett.*, 40, 2038–2043

Tattitch B. C. and Blundy J. D. (2017) Cu-Mo partitioning between felsic melts and saline-aqueous fluids as a function of XNaCleq, $fO2$, and $fS2$. *Am. Mineral.* **102**, 1987–2006.

Uchida, T., Ogawa, Y., Takakura, S. and Mitsuhata, Y. (2000). Geoelectrical investigation of the Kakkonda geothermal field, northern Japan. In *proceedings world geothemal congress, Tohoku-Kyushu, Japan* pp. 1893-1898.

Numerical constraints on the hydrothermal fluid evolution forming the Pirquitas Sn-Ag-Pb-Zn deposit in NW Argentina

Malte Stoltnow[1,2], Philipp Weis[1,2], Maximilian Korges[1]
[1]Institute of Earth and Environmental Science, University of Potsdam, Germany
[2]GFZ German Research Centre for Geosciences, Potsdam, Germany

Abstract. The epithermal Pirquitas Sn-Ag-Pb-Zn mine in NW Argentina is hosted in a domain of metamorphosed sediments without geological evidence for volcanic activity within a distance of about 10 km from the deposit. However, recent geochemical studies of ore-stage fluid inclusions indicate a significant contribution of magmatic volatiles. We tested different formation models by applying an existing numerical process model for porphyry-epithermal systems with a magmatic intrusion located either at a distance of about 10 km underneath the nearest active volcano or hidden underneath the deposit. The results show that the migration of the ore fluid over a 10-km distance results in metal precipitation by cooling before the deposit site is reached. In contrast, simulations with a hidden magmatic intrusion beneath the Pirquitas deposit are in line with field observations, which include mineralized hydrothermal breccias in the deposit area.

1 Introduction

Magmatic-hydrothermal systems form a variety of ore deposits at different proximities to upper-crustal hydrous magma chambers, ranging from greisenization in the roof zone of the intrusion, porphyry mineralization at intermediate depths to epithermal vein deposits near the surface (e.g. Hedenquist and Lowenstern 1994; Sillitoe 2010). Base metal zoning can extend horizontally by distances of up to 8 km, typically containing a proximal Cu-rich core region surrounded by Pb-Zn-Ag mineralization at more distal settings (Lang and Eastoe 1988; Sillitoe 2010). The physical transport processes and chemical precipitation mechanisms vary between deposit types and are often still debated. For this study, we investigated the fluid evolution from proximal to distal settings at the epithermal Pirquitas Sn-Ag-Pb-Zn Mine in NW Argentina, where the origin of the mineralizing fluids is unclear.

The Pirquitas Mine is suggested to be the southernmost of the polymetallic epithermal deposits of the Central Andean Tin Belt (CATB; Fig. 1) (e.g., Paar et al. 2000; Passamani et al. 2020) and its formation is a topic of debate. While the Peruvian and Bolivian deposits of the CATB have a clear association with Miocene magmatism (e.g., Grant et al. 1979), Pirquitas lacks a direct connection to magmatic activity. However, there is evidence from noble gas isotopes for magmatic fluid contribution to the ore fluid, which formed the Pirquitas mineralization (Desanois et al. 2019), and the presence of the Cortaderas breccia, which is suggested to be underlain by an inferred intrusion (Slater et al. 2021).

Figure 1. Map of the southern sector of the Central Andean Tin Belt with the location of the Pirquitas deposit in the southernmost part. Miocene porphyry and subvolcanic intrusions, caldera structures, major WNW-trending lineaments, and fault zones as well as the dominant host rock lithologies are shown (modified from Passamani et al. 2020).

Passamani et al. (2020) propose that a complex magmatic-hydrothermal fluid system could be fed from the nearby Granada volcano and the Coranzuli caldera, which are connected by the Lipez lineament over a distance of ~30 km (Fig. 1). This model suggests that the formation of the Pirquitas system may include ore fluids expelled from a magma reservoir underlying the Granada volcano, which would have travelled a distance of at least 8 km (Fig. 2a).

As an alternative explanation, the model infers a hidden intrusion located underneath the Pirquitas Mine (Fig. 2a). Such an intrusion would promote fluid temperatures of >500°C as suggested for the Bolivian deposits (e.g., Sugaki et al. 1988), which have, however, not been observed in Pirquitas yet,

where the maximum temperature estimate from fluid inclusion analyses is <400°C (Desanois et al. 2019).

Analyses of fluid inclusions hosted in hydrothermal vein quartz and ore minerals from the Pirquitas Mine indicate that the hydrothermal system was characterized by mixing of magmatic fluids and meteoric water (Desanois et al. 2019). This model also proposes that there might be a hidden high-grade Ag (± base metals) lens at depth, which may have served as a source region for later remobilization eventually forming the mineralization at Pirquitas. This interpretation is supported by noble gas analyses (Desanois et al. 2019) and the existence of hydrothermal breccias with mineralized clasts at locations near the open pit mine, which indicates that the hydrothermal system extends to greater depth and suggests that the fluid source may rather be located underneath the deposit.

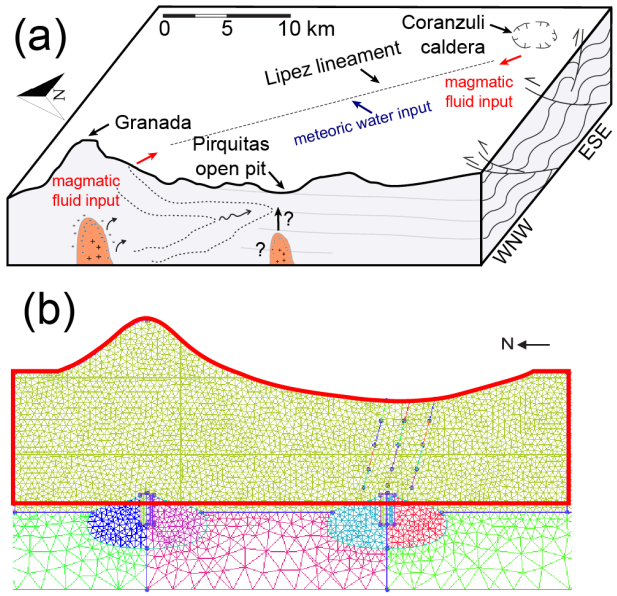

Figure 2. (a) Conceptual model showing the Lipez lineament connecting the Granada stratovolcano and the Coranzuli caldera, forming a complex magmatic-hydrothermal system with potential ore fluids either being related to the Granada volcano or to a hidden proximal intrusion at depth below the Pirquitas open-pit mine (modified from Passamani et al. 2020). (b) Excerpt of the modelling mesh approximating the geological setting including the two hypothesized magma reservoirs at about 5 km depth.

2 Methods

We use numerical simulations to test the different conceptual formation models. Based on the parametrization of Weis et al. (2012), we performed simulations testing the hydrology of mineral systems, where mineralization formed (i) at a distance of about 10 km and (ii) directly above a magmatic intrusion (Fig. 2b). Our approaches include a modelling setup with a total extension of 40 x 9 km. Both the stratovolcano, which rises 2 km above, and an assumed valley, which has incised to a maximum of 1 km below the ambient level, are exaggerating field observations to achieve broader fluid transport by topography-driven groundwater flow. The geometry includes two magma reservoirs, which can be switched on and off in the model configurations for either distal (simulation 1, Fig. 3a) or proximal (simulation 2, Fig. 3b) settings.

The numerical model simulates the release of magmatic fluids from a cooling and crystallizing magma reservoir and its interaction with a dynamic permeability model for hydraulic fracturing that mimics the formation of stockwork veining, and the convection of meteoric fluids. Previous simulations have shown how the interplay of these processes self-organizes into a hydrological divide between a magmatic fluid plume at high temperatures and high pressures and a hydrothermal system with mixed magmatic-meteoric fluids at lower temperatures and pressures (for a detailed description see Weis et al. 2012).

3 Results and Interpretation

With the numerical modelling approach, we can test different formation models for the Pirquitas Deposit, which are based on geochemical (Desanois et al. 2019; Slater et al. 2021), geophysical (Soler et al. 2007) and structural geological (Passamani et al. 2020) studies. Figures 3a and b display the evolution of the hydrology after a simulation time of 15 kyrs, which represents the broadest migration of the temperature fronts.

3.1 Distal Setting

Simulation 1 includes a magma reservoir underlying a stratovolcano. The vertical extension of the stratovolcano promotes the flow of meteoric water towards greater depth suppressing the ascent of magmatic fluid, the accompanied temperature front, and the formation of domains with bulk salinities of >40 wt% NaCl eq. (Fig. 3a). Although fluids containing bulk salinities up to 20 wt% NaCl eq. can travel distances of up to 10 km and thus reach the site of the Pirquitas mineralization, fluid temperatures in this area are limited to <100°C.

Based on simulation results from Stoltnow et al. (2023), which used base metal solubilities reported by Kouzmanov and Pokrovski (2012), this thermal evolution implies that the area in which base metals may accumulate to economic values is restricted to the domain directly overlying the injection point. In this domain, the pore fluid factor is below 0.7 (beginning of the hydrostatic pressure regime) and extends to the 200°C isotherm (Fig. 3a). Consequently, the simulation representing a distal source for the fluids and metals may rather produce an economic mineralization underneath the Granada volcano at a distance of some 10 km, but unlikely produced the primary mineralization at Pirquitas.

3.2 Proximal Setting

In contrast, simulation 2 tests the proximal setup with an inferred magma reservoir right beneath the open-pit mine of the Pirquitas Deposit (Fig. 3b). The vertical depression located above the magma chamber causes a strong inflow of meteoric fluids, which focuses ascending magmatic fluids and the accompanying temperature front. Although the domain right beyond the hydrological divide is characterized by bulk salinities >80 wt% NaCl eq. due the local and temporal saturation of the fluids in solid halite, the overall migration of saline fluids (>0 wt% NaCl eq.) is restricted to the focused region between the hydrological divide and the Pirquitas open pit (Fig. 3b).

Similarly, the area of potential economic metal enrichment is more focused (~2 km horizontal extension) compared to the distal setting (~4 km horizontal extension) and reaches shallower depths of ~2 km. Furthermore, higher bulk salinities along the outer part of the hydrological divide could support an overall higher metal enrichment potential (Stoltnow et al., 2023) and higher ore grades. The modelled depth level, temperature, salinity, and mixed origin (magmatic and meteoric) of hydrothermal ore formation are in agreement with recent findings (Desanois et al. 2019; Slater et al. 2021). In addition, the modelled transition from lithostatic to hydrostatic fluid pressures at the hydrological divide would be in line with the presence of a hydrothermal breccia below the Pirquitas Mine.

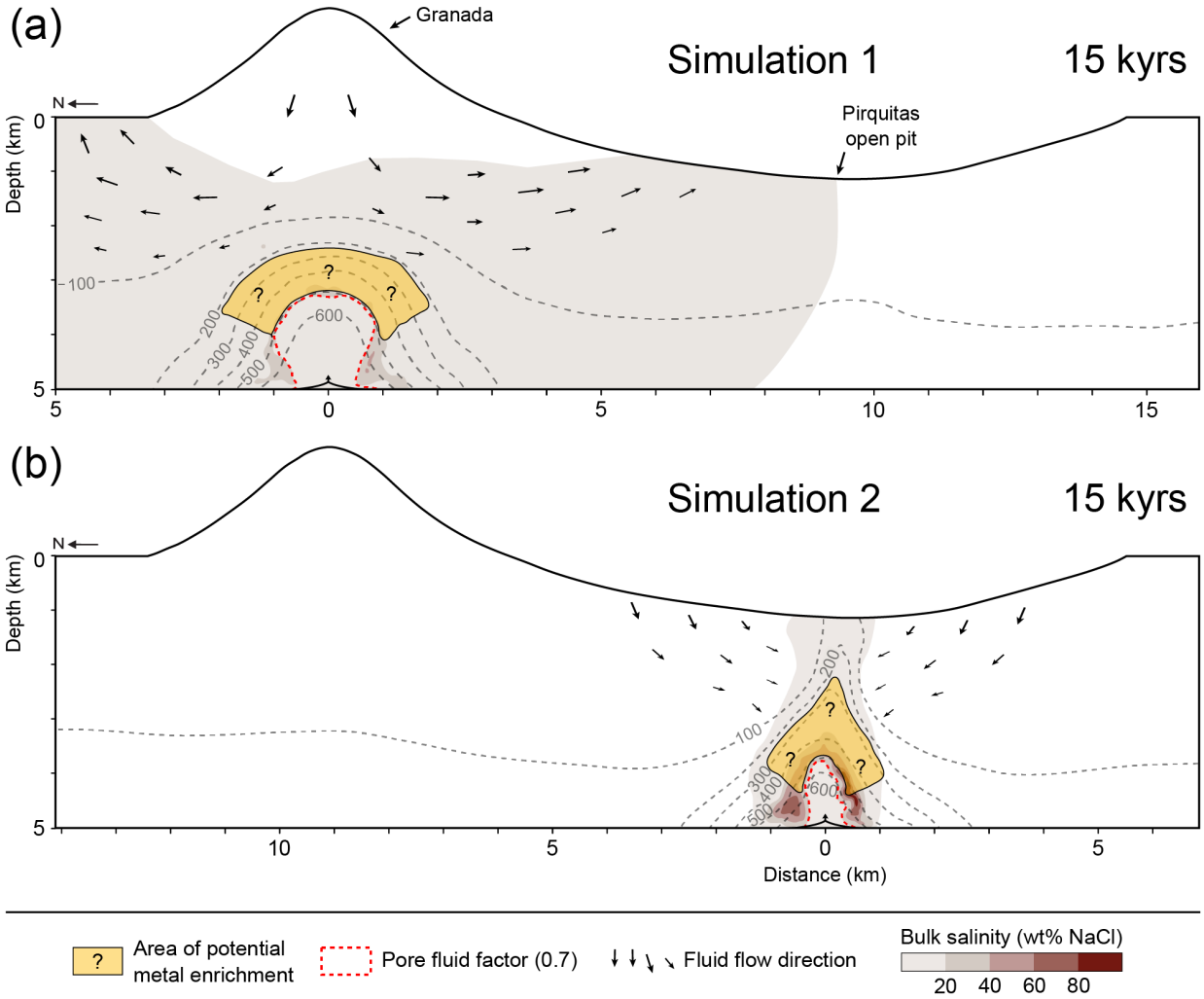

Figure 3. Bulk fluid salinity (colours) and isotherms (dashed lines) of the modelled Pirquitas hydrothermal system after 15 kyrs with a magma reservoir beneath the Granada stratovolcano (a) and beneath the Pirquitas deposit (b). The extent of the areas with potential and economic metal enrichment is based on modelling results in Stoltnow et al. (2023). The pore fluid factor (fluid pressure divided by lithostatic pressure) of 0.7 indicates the transition from near-hydrostatic to near-lithostatic fluid pressures. Arrows at a depth of 5 km refer to the fluid injection location at the cupola region of the magma reservoir.

4 Discussion and Conclusions

Our modeling results show that fluids necessary to form Pirquitas-like mineralization may not be transported farther than 2-3 km in both horizontal and vertical directions from the porphyry region of the magma reservoir (Fig. 3b). Later remobilization can lead to further transport and reprecipitation of

base metals at further distances (Stoltnow et al. 2023), but is unlikely to be permissive with the hypothesis of the Pirquitas mineralization being fed by a magma reservoir underneath the Granada stratovolcano (e.g. Passamani et al. 2020).

Instead, the simulations rather highlight the necessity of an intrusion underneath or in closer proximity to a Pirquitas-like mineralization, which has also been proposed previously (Desanois et al. 2019; Passamani et al. 2020; Slater et al. 2021). These findings are supported by the occurrence of hydrothermal breccias at both the Pirquitas Deposit and the Cortaderas Deposit some 500 m north of the Pirquitas open pit, which is proposed to be underlain by a hidden intrusion (Slater et al. 2021).

The simulations rely on a number of simplifications. In this reconnaissance study, we reduced the geological complexity to investigate first-order controls on the ore-forming hydrothermal system. To obtain a lateral transport by 10 km from the cupola region of the magma reservoir, the model required a significant topographic gradient from the volcano summit to the deposit location as a driving force for the convection of meteoric fluids. However, the same process also leads to strong cooling of the metal-bearing magmatic fluids. Further simulations could include more geological heterogeneity in the permeability structure, e.g., by including fault zones or low-permeability lithocaps, which may support lateral fluid migration with less cooling.

In general, the simulations show that the quantification of first-order controls on the physical hydrology at the porphyry-epithermal transition can be instrumental to understand the ore-forming system beyond the deposit scale.

Acknowledgements

This project is part of the international research training group StRATEGy at the University of Potsdam (Germany) and was funded jointly by the German Research Foundation (DFG) and the State of Brandenburg, Germany.

References

Desanois L, Lüders V, Niedermann S, Trumbull RB (2019) Formation of epithermal Sn-Ag-(Zn) vein-type mineralization at the Pirquitas deposit, NW Argentina: Fluid inclusion and noble gas isotopic constraints. Chem Geol 508:78–91. https://doi.org/https://doi.org/10.1016/j.chemgeo.2018.04.024

Grant JN, Halls C, Avila Salinas W, Snelling NJ (1979) K-Ar ages of igneous rocks and mineralization in part of the Bolivian tin belt. Econ Geol 74:838–851. https://doi.org/10.2113/gsecongeo.74.4.838

Hedenquist JW, Lowenstern JB (1994) The role of magmas in the formation of hydrothermal ore deposits. Nature 370: 519-527

Kouzmanov K, Pokrovski G (2012) Hydrothermal Controls on Metal Distribution in Porphyry Cu (-Mo-Au) Systems. SEG Special Publication 16:573–618

Lang JR, Eastoe CJ (1988) Relationships between a porphyry Cu-Mo deposit, base and precious metal veins and Laramide intrusions, Mineral Park, Arizona. Econ Geol 83:551–567. https://doi.org/10.2113/gsecongeo.83.3.551

Paar WH, Miletich R, Topa D, et al (2000) Suredaite, PbSnS3, a new mineral species, from the Pirquitas Ag-Sn deposit, NW-Argentina: mineralogy and crystal structure. Am Miner 85:1066–1075. https://doi.org/doi:10.2138/am-2000-0723

Passamani FM, Bongiolo EM, Nepomuceno de Oliveira F, Neumann R (2020) Geology and structural controls of the Ag–Sn–Zn Pirquitas deposit, northwestern Argentina. J South Am Earth Sci 100:102537. https://doi.org/https://doi.org/10.1016/j.jsames.2020.102537

Sillitoe RH (2010) Porphyry copper systems. Econ Geol. 105: 3-41 https://doi.org/10.2113/gsecongeo.105.1.3

Slater ET, Kontak DJ, Mcdonald AM, Fayek M (2021) Origin of a multi-stage epithermal Ag-Zn-Pb-Sn deposit: the Miocene Cortaderas breccia body, Pirquitas mine, NW Argentina. Miner Depos 56:381–406. https://doi.org/10.1007/s00126-020-00976-8

Soler MM, Caffe PJ, Coira BL, et al (2007) Geology of the Vilama caldera: A new interpretation of a large-scale explosive event in the Central Andean plateau during the Upper Miocene. J Volcanol Geotherm Res 164:27–53. https://doi.org/https://doi.org/10.1016/j.jvolgeores.2007.04.002

Stoltnow M, Weis P, Korges M (2023) Hydrological controls on base metal precipitation and zoning at the porphyry-epithermal transition constrained by numerical modeling. Sci Rep https://doi.org/10.1038/s41598-023-30572-5

Sugaki A, Kojima S, Shimada N (1988) Fluid inclusion studies of the polymetallic hydrothermal ore deposits in bolivia. Miner Depos 23:9–15. https://doi.org/10.1007/BF00204221

Weis P, Driesner T, Heinrich CA (2012) Porphyry-Copper Ore Shells Form at Stable Pressure-Temperature Fronts Within Dynamic Fluid Plumes. Science 338:1613–1616. https://doi.org/10.1126/science.1225009

Ore Mineral Textures of the Midas Low-Sulfidation Epithermal Deposit: Implications for Ore-Forming Processes

Lauren R. Zeeck[1], Thomas Monecke[1], T. James Reynolds[1,2], Katharina Pfaff[1], Nigel M. Kelly[3]
[1]Department of Geology and Geological Engineering, Colorado School of Mines, Golden, CO, USA
[2]FLUID INC., 1401 Wewatta St. #PH3, Denver, Colorado 80202, USA
[3]Bruker Nano Analytics, 415 N Quay Street, Kennewick, WA 99336, USA

Abstract. Ore and gangue mineral textures of high-grade quartz vein material from the middle Miocene Midas Au-Ag deposit near Elko, Nevada, were studied to identify the processes that resulted in precious metal enrichment at this low-sulphidation epithermal deposit. Ore minerals in high-grade samples occur as dendritic aggregates within distinct ginguro bands. The delicate ore mineral dendrites are hosted by mosaic quartz that appears to have formed through recrystallisation of a microspherical silica precursor. Based on the comparison to modern geothermal systems, this microspherical silica precursor is interpreted to have been gel-like opal-A_G originally. The occurrence of ore mineral dendrites and microspherical opal-A_G suggests that mineral precipitation at Midas occurred at far-from-equilibrium conditions. The findings of this study are consistent with previous models linking high-grade precious metal enrichment in low-sulfidation epithermal deposits to episodic flash vaporisation of the hydrothermal liquids within hundreds of meters from the paleosurface.

1 Introduction

The Miocene Midas low-sulfidation epithermal deposit located along the Northern Nevada Rift (NNR) in the Battle Mountain-Eureka trend in northeast Nevada comprises a complex of high-grade Au-Ag veins. Previously known as the Ken Snyder mine, underground mining at Midas yielded over 2.2 million ounces of gold and 27.6 million ounces of silver from 1998 to 2017, making it the largest known producer in this region (Leavitt et al. 2004; Thompson 2017).

Previous studies on the ore mineralogy of the Midas deposit focus on the multiple stages of mineral deposition which formed the main veins, namely the Colorado Grande and Gold Crown veins. Ore minerals include naumannite, aguilarite, and electrum with minor amounts of native silver and fischesserite, plus rare lead-, copper-, and iron-selenide minerals (Goldstrand and Schmidt 2000).

The present contribution reports on findings from the study of fourteen high-grade vein samples from the Colorado Grande, Gold Crown, Snow White, Discovery, and Sleeping Beauty veins. The results of this petrographic study demonstrate that ore minerals at Midas were deposited under chemical disequilibrium conditions established during flash vaporisation of the hydrothermal liquids and that these conditions propagated down to at least ~500 m depth below surface.

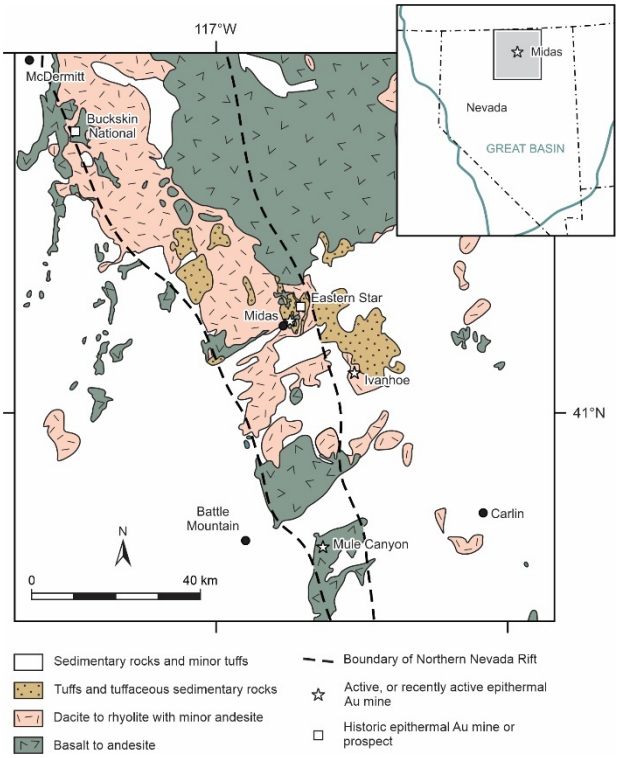

Figure 1. Regional geology and location of the Northern Nevada Rift. The map also highlights the locations of major low-sulfidation epithermal precious metal occurrences (modified from Leavitt et al. 2004).

2 Regional geology

The Midas deposit is located in the Midas mining district and occurs along the eastern margin of the NNR (Fig. 1). The NNR is a north-northwest trending lineament defined by a positive aeromagnetic anomaly that extends ~500 km from south-eastern Nevada to the Nevada-Oregon border (John et al. 2000). Formation of the NNR is related to regional extension and subsequent emplacement of mafic magmas related to the Yellowstone hot spot (John et al. 2000).

The Midas deposit is coeval with Miocene bimodal volcanism that occurred along the NNR from 16.5 to 14.7 Ma (Zoback et al. 1994; John et al. 2000; Leavitt et al. 2004). The Midas volcanic assemblage includes felsic ash-flow tuffs, flows, domes, and volcaniclastic sedimentary deposits, as well as mafic sills and dikes (Goldstrand and Schmidt 2000; Leavitt et al. 2004).

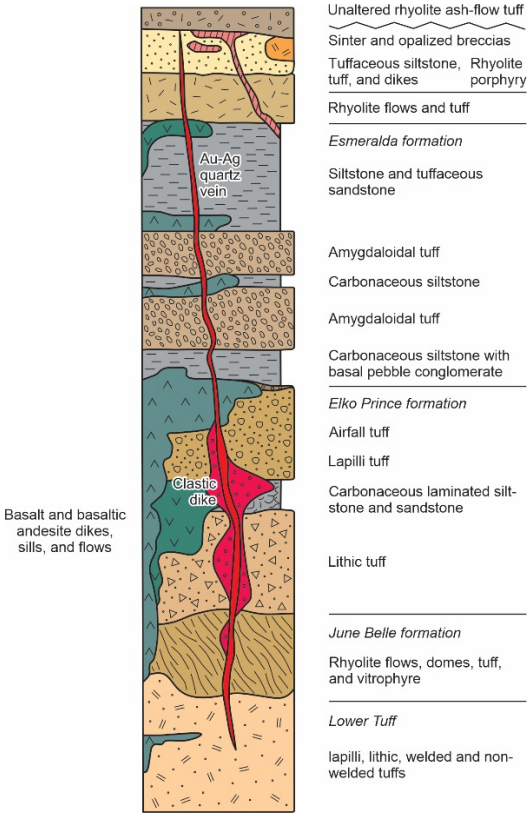

Figure 2. Generalized stratigraphic section of the Midas deposit. Ore is primarily confined to steeply dipping quartz veins (shown in red), which crosscut all units below the unaltered rhyolite ash-flow unit (modified from Goldstrand and Schmidt 2000; Leavitt et al. 2004).

Host rocks to the Midas deposit consist of four primary stratigraphic units, the Lower Tuff, June Belle, Elko Prince, and Esmeralda formations, that extend to a depth of ~1.5 km below the present-day surface (Leavitt et al. 2004). Mineralized quartz veins are steeply dipping and crosscut all principal stratigraphic units (Fig. 2). These are topped by an unaltered rhyolite ash-flow tuff.

3 Materials and methods

Representative vein samples were collected from twelve drill holes (C96-0008, C96-0011, MKC-0232, MKC-0244, MKC-0266, MKC-0267, MSC-0158, MSC-0165, MSC-0171, and RG-0038, RG-0096, and RG-0100) at Hecla's core storage near Elko, Nevada. Initially, the distribution of major and trace elements in cut hand specimens and billets was mapped using a bench-top Bruker M4 Tornado µXRF. The spot size of acquisition was ~25 µm. Element mapping was conducted at a line scan spacing of 50 µm, and a data acquisition dwell time of 50 ms per pixel. Following data acquisition, X-ray peaks were checked manually.

Following µXRF analysis, single-sided polished 80-µm-thick sections were prepared. These were studied in transmitted and reflected light using an Olympus BX51 microscope to document ore and gangue mineral textures.

Following optical petrography, ore mineralogy was determined using automated scanning electron microscopy at the Colorado School of Mines. Samples were loaded into the TESCAN-VEGA-3 Model LMU VP-SEM platform, which is controlled by the TIMA3 software package. Four energy dispersive X-ray (EDX) spectrometers acquired spectra with a beam stepping interval of 25 µm, an accelerating voltage of 20 keV, and a beam intensity of 17. Results output by the TIMA software allows a compositional map to be generated and composition assignments to be grouped appropriately. In addition to automated scanning electron microscopy, a TESCAN MIRA3 LMH Schottky field emission-scanning electron microscope equipped with a single-crystal YAG backscatter electron detector was used to study the ore mineralogy. Imaging was performed at a working distance of 10 mm and an accelerating voltage of 15 kV. Semiquantitative chemical analyses of minerals were performed by energy-dispersive X-ray spectroscopy using an attached Bruker XFlash 6|30 silicon drift detector.

4 Ore mineral petrography

Veins samples from the Midas low-sulphidation epithermal deposit are typically massive, crustiform, or brecciated. Bonanza-grade samples contain colloform bands of quartz of varying colour, texture, grain size, and thickness. Typically, quartz is white to translucent. Many vein samples contain adularia that is milky-white in colour and commonly is intergrown with quartz. Quartz pseudomorphs of calcite are common.

In the bonanza-grade vein samples from Midas, ore minerals primarily occur in specific colloform bands within the crustiform veins or are distributed irregularly between the clasts and matrix of brecciated samples. Ore minerals typically occur as dendritic aggregates (Fig. 3a). Element maps created by µXRF show that elevated Ag concentrations typically correlate with Se-enrichment. Bands of high-grade Ag sometimes contain high Au concentrations. However, there is no direct correlation between Ag and Au at the microscale (Figs. 3b, c).

Au and Ag are present primarily as naumannite, aguilarite, and electrum in the samples investigated. Sulfoselenides are light grey, weakly anisotropic, and have a low reflectance with a metallic or adamantine lustre. The Ag sulfoselenides can be intergrown with minor electrum. Electrum aggregates range from 15 to 40 µm in size. They are golden to whitish in reflected light.

The ore mineral dendrites are hosted by microcrystalline quartz (Fig. 3d). The microcrystalline quartz appears to have formed through recrystallisation of a silica precursor. In least-recrystallized areas, the quartz shows a mosaic texture in crossed-polarized light whereby individual quartz grains have irregular and inter-

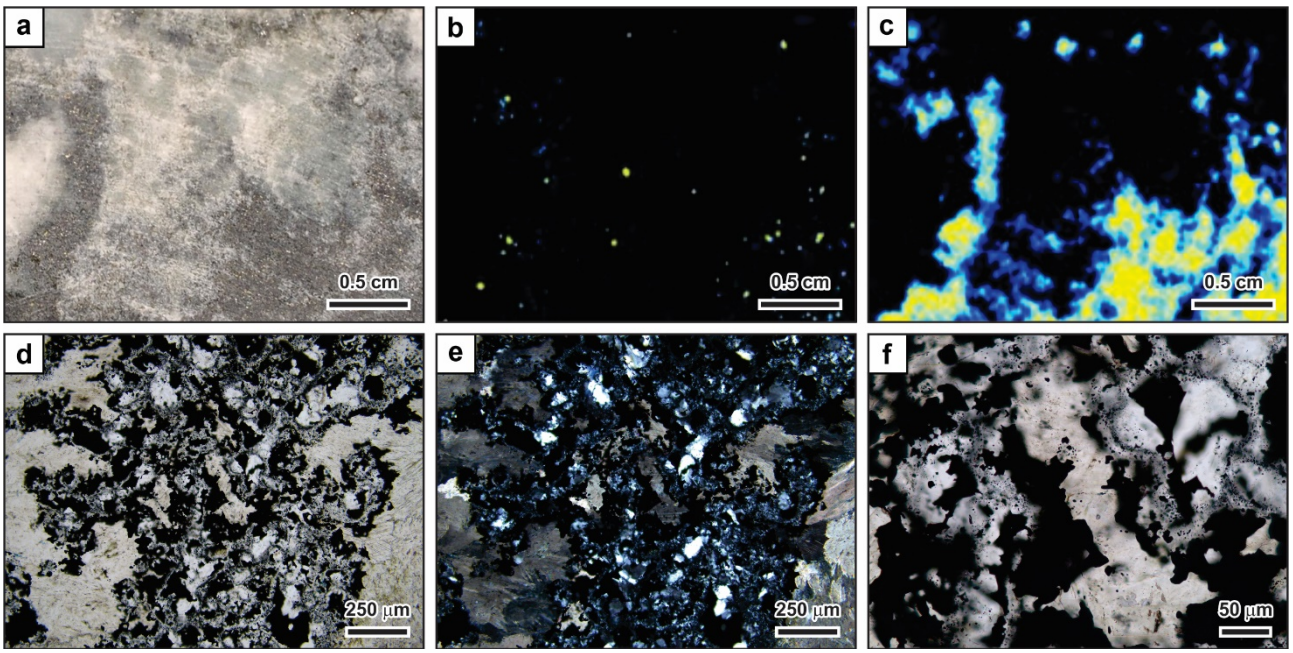

Figure 3. Microtextures and trace element maps of a representative quartz vein sample from drill hole MKC-0232 at the Midas deposit, Nevada. **a** RGB sample image of the scanned billet MKC-0232G (drill hole depth of 349 m). **b** µXRF element map of Au count rates. Individual gold grains are scattered. **c** µXRF element map of Ag count rates. Ag is present in higher quantities than Au and forms aggregates that are dendritic in nature. **d** Photomicrograph of ore mineral dendrite. Plane-polarized light. **e** Same field of view showing the mosaic texture of the quartz hosting the ore mineral dendrite. Crossed-polarized light. **f** High-magnification image of ore mineral grains in contact with the mosaic quartz. The recrystallisation of the silica matrix locally resulted in the formation of small euhedral quartz crystals.

penetrating grain boundaries and differ in orientation (Fig. 3e). Where intensely recrystallized, the quartz grains have polygonal shapes. At the microscale, the ore minerals are in contact with the recrystallized microcrystalline quartz. In some cases, the quartz forming the matrix is overgrown by small euhedral quartz crystals (Fig. 3f). Ore minerals also occur as encapsulated inclusions in the quartz (Fig. 3f).

5 Discussion and conclusions

The textural observations at Midas are similar to those in other low-sulphidation epithermal deposits. Previous research suggests that the mosaic quartz that is now present in the vein samples at Midas formed through recrystallisation of a noncrystalline silica precursor. This precursor phase was originally microspherical in nature, similar to opal-A_G, which forms a common scale in geothermal systems (Moncada et al. 2012; Taksavasu et al. 2018; Tharalson et al. 2019; Zeeck et al. 2021; Monecke et al. 2023).

It has been proposed that ore mineral dendrites form in open spaces through colloidal metal transport (Saunders 1990). However, recent studies by Monecke et al. (2023) on the McLaughlin low-sulphidation epithermal deposit in California have shown that ore mineral dendrite formation took place within bands of noncrystalline silica gel. The gel provided a protective layer within which the ore mineral dendrites may grow through diffusion and advection processes (Monecke et al. 2023). The dendrites at Midas likely formed in the same manner. The delicate ore mineral dendrites are encapsulated by the mosaic quartz that formed through recrystallisation of the microspherical silica precursor. The colloform silica bands appear to have formed first.

Previous workers have shown that deposition of the noncrystalline silica forming the matrix to the ore mineral dendrites required the hydrothermal liquids to periodically reach extreme supersaturation. Such high degrees of silica supersaturation were most likely achieved through vapor loss associated with catastrophic pressure drops accompanying hydrothermal eruptions on the surface. Following flash vaporisation of hydrothermal liquids, ore mineral dendrites grew within the newly deposited silica gel from the metal-laden hydrothermal liquids. Repetition of this process through time would explain that the colloform veins in low-sulphidation epithermal deposits contain multiple, discrete ginguro bands (Moncada et al. 2012; Taksavasu et al. 2018; Tharalson et al. 2019; Zeeck et al. 2021; Monecke et al. 2023).

The samples from the Midas low-sulphidation epithermal deposit provide important context for understanding the formation of high-grade veins in the epithermal environment. Samples investigated containing ore mineral dendrites in ginguro bands were sampled at depths of up to ~500 m below the surface. This implies that flash vaporisation of the hydrothermal liquids along the controlling structures must have occurred to significant depths below the paleosurface. As such, bonanza-grade ore zones in low-sulphidation deposits formed through flash vaporisation may reach to greater depths than predicted by the generally accepted model of epithermal ore formation (Buchanan 1981).

Acknowledgments

John Marma and Hecla Mining Company are thanked for their help in procuring samples. High Mesa Petrographics conducted the thin section preparation. We thank Quinton Hennigh for his insights into the geology of epithermal deposits.

References

Buchanan LJ (1981) Precious metal deposits associated with volcanic environments in the southwest Ariz Geol Soc Dig 14:237–262

Goldstrand PM, Schmidt KW, (2000) Geology, mineralization, and ore controls at the Ken Snyder gold-silver mine, Elko County, Nevada. In: Cluer JK, Price JG, Struhsacker EM, Hardyman RF, Morris CL (eds) Geology and Ore Deposits 2000: The Great Basin and Beyond. Geol Soc Nev Symp Proc, pp 265–287

John DA, Wallace AR, Ponce DA, Fleck RB, Conrad JE (2000) New perspectives on the geology and origin of the northern Nevada rift. In: Cluer JK, Price JG, Struhsacker EM, Hardyman RF, Morris CL (eds) Geology and Ore Deposits 2000: The Great Basin and Beyond. Geol Soc Nev Symp Proc, pp 127–154

Leavitt ED, Spell TL, Goldstrand PM, Arehart GB (2004) Geochronology of the Midas low-sulfidation epithermal gold-silver deposit, Elko county, Nevada. Econ Geol 99:1665–1686

Moncada D, Mutchler S, Nieto A, Reynolds TJ, Rimstidt JD, Bodnar RJ (2012) Mineral textures and fluid inclusion petrography of the epithermal Ag–Au deposits at Guanajuato, Mexico: Application to exploration. J Geochem Explor 114:20–35

Monecke T, Reynolds TJ, Taksavasu T, Tharalson ER, Zeeck LR, Guzman M, Gissler G, Sherlock R (2023) Natural growth of gold dendrites within silica gels. Geology 51:189–192

Saunders JA (1990) Colloidal transport of gold and silica in epithermal precious-metal systems: Evidence from the Sleeper deposit, Nevada. Geology 18:757–760

Taksavasu T, Monecke T, Reynolds TJ (2018) Textural characteristics of noncrystalline silica in sinters and quartz veins: Implications for the formation of bonanza veins in low-sulfidation epithermal deposits. Minerals 8:331

Tharalson ER, Monecke T, Reynolds TJ, Zeeck L, Pfaff K, Kelly NM (2019) The distribution of precious metals in high-grade banded quartz veins from low-sulfidation epithermal deposits: Constraints from μXRF mapping. Minerals 9:740

Thompson W (2017) Update of geology within the Midas Au/Ag mining district, Elko County, Nevada. Geol Soc Nev Newsl 33:3

Zeeck LR, Monecke T, Reynolds JT, Tharalson ER, Pfaff K, Kelly NM, Hennigh QT (2021) Textural characteristics of barren and mineralized colloform quartz bands at the low-sulfidation epithermal deposits of the Omu Camp in Hokkaido, Japan: Implications for processes resulting in bonanza-grade precious metal enrichment. Econ Geol 116:407–425

Zoback ML, McKee EH, Blakely RJ, Thompson GA (1994) The northern Nevada rift: Regional tectono-magmatic relations and middle Miocene stress direction. Geol Soc Am Bull 106:371–382

